



中国科学院大学  
University of Chinese Academy of Sciences

# 博士学位论文

## 使用 LAMOST 光谱数据库搜索第一颗星的化学指纹

作者姓名: Mohammad Khaled Hashem Mardini

指导教师: 赵刚 研究员 中国科学院国家天文台

李海宁 研究员 中国科学院国家天文台

学位类别: 理学博士

学科专业: 天体物理

培养单位: 中国科学院国家天文台

2019 年 8 月 22 日



**Search for the Chemical Fingerprints of the First Stars using the**  
**LAMOST Spectroscopic Database**

A dissertation submitted to the  
University of Chinese Academy of Sciences  
in partial fulfillment of the requirement  
for the degree of  
Doctor of Natural Science  
in Astrophysics  
By  
Mohammad Khaled Hashem Mardini  
Supervisor: Professor Zhao Gang  
Dr. Haining Li

National Astronomical Observatories of China  
Chinese Academy of Sciences

2019 年 8 月 22 日



## **中国科学院大学**

### **学位论文原创性声明**

本人郑重声明：所呈交的学位论文是本人在导师的指导下独立进行研究工作所取得的成果。尽我所知，除文中已经注明引用的内容外，本论文不包含任何其他个人或集体已经发表或撰写过的研究成果。对论文所涉及的研究工作做出贡献的其他个人和集体，均已在文中以明确方式标明或致谢。本人完全意识到本声明的法律结果由本人承担。

作者签名：

日 期：

## **中国科学院大学**

### **学位论文授权使用声明**

本人完全了解并同意遵守中国科学院大学有关保存和使用学位论文的规定，即中国科学院大学有权保留送交学位论文的副本，允许该论文被查阅，可以按照学术研究公开原则和保护知识产权的原则公布该论文的全部或部分内容，可以采用影印、缩印或其他复制手段保存、汇编本学位论文。

涉密及延迟公开的学位论文在解密或延期后适用本声明。

作者签名：

导师签名：

日 期：

日 期：



## 摘要

众所周知，第一代恒星是在高红移的低质量晕圈中形成的。这些恒星物体的典型质量 ( $M_\star \sim 100 M_\odot$ ) 与现今的恒星相比更高；由于没有足够的冷却剂。然而，这些短命的恒星在它们爆炸并用重金属（例如碳和氧）污染周围的原始气体时，已经戏剧性地改变了这幅画面。提供有效气体冷却的途径，从而允许形成低质量和中质量恒星。因此，推测 Pop III 恒星的后代显示出独特的丰度模式（相当低的铁和高度增强的碳）。

在这项研究中，我们提出 12 种金属贫乏恒星的化学成分和运动参数，在银河系光环系统的金属度范围为  $-3.3 < [\text{Fe} / \text{H}] < -2.4$ 。这个恒星样本最初被确定为 LAMOST DR3 低分辨率 ( $R \sim 2,000$ ) 中的金属贫乏候选者。Lick / APF 获得高分辨率 ( $R \equiv \lambda / \Delta\lambda \sim 110,000$ ) 光谱观察。我们确定了恒星参数 ( $T_{\text{eff}}$ ,  $\log g$ ,  $[\text{Fe}/\text{H}]$  和  $\xi$ ) 以及最多 25 个元素的个体丰度：包括碳和氮，光 (Na-Ca)，铁-峰 (Sc-Zn) 和多达 11 个中子俘获元素（包括 Ba 和 Eu），以定量评估我们的 tagret 星。我们的样本恒星的化学丰度模式显示我们的样本包含五个碳正常恒星和七个碳增强金属贫乏 (CEMP) 恒星：(i) CEMP-r/s 恒星 J2114-0616  $[\text{C}/\text{Fe}] = 1.37$ ,  $[\text{N}/\text{Fe}] = 1.88$ ,  $[\text{Ba}/\text{Fe}] = 1.00$ ,  $[\text{Eu}/\text{Fe}] = 0.84$ , (ii) CEMP-r 星 J1054 + 0528,  $[\text{C}/\text{Fe}] = 0.82$ ,  $[\text{Eu}/\text{Fe}] = 0.44$  和  $[\text{Ba}/\text{Fe}] = -0.52$  (iii) CEMP-no ( $[\text{C}/\text{Fe}] \geq +0.7$  和  $[\text{Ba}/\text{Fe}] < 0.0$ ) 明星 J1529+0804, J1630+0953, J1645+4357, J2216+0246 和 J2216+2232。此外，观察到的光和重元素的化学丰度表明我们的目标恒星可能是由混合良好的恒星云产生的。

此外，我们使用两个 CEMP-no 星 (J1630+0953 和 J2216+0246) 的光元素丰度与零金属度超新星模型进行蒙特卡罗模拟比较，产生  $10^4$  生成集，以推断质量 CEMP 恒星的恒星祖先的分布。对于 J1630+0953 的情况，绝大多数这些集合 (*sim* 94) 与预测的祖先产量相匹配，恒星质量范围为  $21\text{-}25M_\odot$  和爆炸能量  $0.3 \times 10^{51} \text{ erg}$ 。其余的这些生成组 (600 组) 显示，恒星质量为  $50 M_\odot$  和爆炸能量为  $10.0 \times 10^{51} \text{ erg}$  的祖先可能是造成污染的原因。J1630 + 0953 诞生云。J2216 + 0246 的采样集周围的  $\sim 85$  表明在 J2216+0246 大气中携带的观测元素模式对应

于恒星质量范围为  $13\text{-}16 M_{\odot}$  和爆炸能量  $1.5\text{-}1.8 \times 10^{51} \text{ erg}$ 。然而，在大约  $\sim 15$  的 J2216+0246 生成的套装匹配更重的恒星质量范围 ( $10.6\text{-}29.5 M_{\odot}$ ) 和更强的爆炸能量 ( $0.6\text{-}5 \times 10^{51} \text{ erg}$ )。一般而言，这种蒙特卡罗模拟练习表明，这些巨大恒星祖先的化学产量污染了 J1630+0953 和 J2216+0246 的出生云，然后提供冷却途径以允许形成这些 CEMP-no 恒星。此外，这些可能的祖先（恒星质量范围为  $13\text{-}25 M_{\odot}$  和爆炸能量为  $0.3\text{-}1.8 \times 10^{51} \text{ erg}$ ）可以解决第一代恒星的初始质量函数。与此同时，他们提出了另一个问题，即无论是否更大规模的 SN，它可能会更加精力充沛，消灭主机晕云并且不允许形成 EMP 星。

为了完整起见，我们根据最近发表的 Gaia DR2 观测结果对我们的样本恒星进行了运动学和动力学分析。这个练习的结果（运动参数，恒星轨道和结合能）表明我们的样本只包含一个外部晕星 (J2114 – 0616)，而我们的其他样本恒星可能是内晕星，但是有一个增生起源。此外，我们的样本恒星的巨大主体距离银河系中心的距离接近  $\sim 2.9 \text{ kpc}$ 。

一般来说，这项研究试图将我们的样本恒星的衍生丰度模式与源自盖亚 DR2 观测的运动学相关联，从而对起源和 CEMP 恒星的化学演化，以及对银河系中最低金属度恒星的群体 III 祖先的性质的严格限制。

**关键词：** 银河系：光环---恒星：基本参数---恒星：丰度—恒星：运动学和动力学---恒星：人口 II ---恒星：化学特殊

## Abstract

It is widely recognized that the very first-generation of stars (Population III or Pop III) have formed in low-mass halos at high-redshifts. The typical mass of these stellar objects ( $10 - 1000 M_{\odot}$ ) indicates the absence of sufficient cooling agents. However, these short-lived stars had dramatically changed this picture by the time they exploded and polluted the surrounding pristine gas with heavy metal (e.g., carbon); providing pathways for efficient gas cooling, and thus allowing the low- and intermediate-mass stars to form. As a result, the progeny of Pop III stars are presumed to show unique abundance patterns (low iron abundances with high carbon enhancement).

In this study, we present chemical compositions and kinematic parameters of 12 stars in the metallicity range of  $-3.3 < [\text{Fe}/\text{H}] < -2.4$  in the Milky Way halo system. This sample of stars was first identified as metal-poor candidates in the LAMOST DR3 low-resolution ( $R \sim 2,000$ ). High-resolution ( $R \equiv \lambda/\Delta\lambda \sim 110,000$ ) spectroscopic observations were obtained by the Lick/APF. We determined stellar parameters ( $T_{\text{eff}}$ ,  $\log g$ ,  $[\text{Fe}/\text{H}]$ , and  $\xi$ ) and individual abundances for up to 25 elements: include carbon and nitrogen, light (Na-Ca), iron-peak (Sc-Zn), and up to 11 neutron-capture elements (including Ba and Eu), to quantitatively evaluate our target stars. The chemical abundance patterns of our sample stars reveal that our sample contain five carbon normal stars and seven carbon-enhanced metal-poor (CEMP) stars: (i) The CEMP-r/s star J2114–0616 with  $[\text{C}/\text{Fe}] = 1.37$ ,  $[\text{N}/\text{Fe}] = 1.88$ ,  $[\text{Ba}/\text{Fe}] = 1.00$ , and  $[\text{Eu}/\text{Fe}] = 0.84$ , (ii) The CEMP-r star J1054+0528 with  $[\text{C}/\text{Fe}] = 0.82$ ,  $[\text{Eu}/\text{Fe}] = 0.44$  and  $[\text{Ba}/\text{Fe}] = -0.52$  (iii) The CEMP-no ( $[\text{C}/\text{Fe}] \geq +0.7$  and  $[\text{Ba}/\text{Fe}] < 0.0$ ) stars J1529+0804, J1630+0953, J1645+4357, J2216+0246, and J2216+2232. Besides, the observed chemical abundances of the light and the heavy elements indicate that our target stars might likely be born from a well-mixed stellar cloud.

In addition, we performed Monte Carlo simulations comparison of  $10^4$  sets, using the light-element abundances of two CEMP-no stars (J1630+0953 and J2216+0246) with zero-metallicity supernova models to infer the mass distribution of the stellar

progenitors of CEMP stars. For the case of J1630+0953, the majority of these sets ( $\sim 94\%$ ) matches the predicted yields of a progenitor with a stellar-mass range of 21-25  $M_{\odot}$  and explosion energy of  $0.3 \times 10^{51}$  erg. The rest of these generated sets (600 sets) shows that a progenitor with a stellar mass of  $50 M_{\odot}$  and explosion energy of  $10.0 \times 10^{51}$  erg is likely responsible for the contamination of the J1630+0953 birth cloud. Around 85% of the sampled sets of J2216+0246 suggest that the observed elemental pattern carried in J2216+0246 atmosphere correspond to a progenitor with a stellar-mass range of 13-16  $M_{\odot}$  and explosion energy of  $1.5-1.8 \times 10^{51}$  erg. However, in about 15% of J2216+0246 generated sets matches heavier stellar-mass range ( $10.6-29.5 M_{\odot}$ ) and stronger explosion energies ( $0.6-5 \times 10^{51}$  erg). In general terms, this Monte Carlo simulations exercise indicates that chemical yields of these massive stellar progenitors polluted the birth cloud of J1630+0953 and J2216+0246, which then provided cooling pathways to allow the formation of these CEMP-no stars. Moreover, these possible progenitors (stellar-mass range of 13-25  $M_{\odot}$  and explosion energies of  $0.3-1.8 \times 10^{51}$  erg) may address the initial mass function of the very first stellar generation. At the same time, they raise another question whether or not more massive SN, which in term might be more energetic, wipeout the host halo cloud and not permit the formation of EMP stars.

For completeness, we conducted a kinematic and dynamical analysis for our sample stars based on the recently published observations of Gaia DR2. The results of this exercise (kinematic parameters, stellar orbits, and binding energy) indicate that our sample contains only one outer halo star (J2114-0616), while the rest of our sample stars are likely inner halo stars, but with an accreted origin. Also, the vast majority of our sample stars, pass close to the Galactic center ( $\sim 2.9$  kpc).

In general, this study attempts to attach two cosmological solutions (the derived abundance patterns of our sample stars and the kinematics derived from Gaia DR2 observations) to place crucial limitations on the origin and chemical evolution of CEMP stars, together with critical constraints on the nature of the Population III progenitors of the lowest metallicity stars in our Galaxy.

**Keywords:** Galaxy: halo— stars:fundamental parameters— stars: abundances---stars: kinematics and dynamics — stars: Population II— stars: chemically peculiar



## 目 录

摘要 .....	1
Abstract .....	III
<b>第1章 Introduction .....</b>	<b>1</b>
1.1 Stars Formation .....	3
1.2 Stellar Evolutions .....	5
1.2.1 H-Burning Phase .....	6
1.2.2 The Helium Burning Phase .....	10
1.2.3 The Advance Evolutionary Phase .....	11
1.3 Stellar Populations .....	13
1.3.1 The first stars .....	14
1.3.2 Metal-poor stars .....	15
1.3.3 The diversity of the observed chemical abundances of metal-poor stars	18
1.4 The structure of the Milky Way system .....	21
<b>第2章 Target Selection and Observations .....</b>	<b>27</b>
2.1 Target Selection From LAMOST survey .....	27
2.2 High-resolution Observations with Lick/APF .....	28
<b>第3章 Data Reductions .....</b>	<b>31</b>
3.1 Data reductions with IRAF .....	31
<b>第4章 Stellar Parameters .....</b>	<b>35</b>
4.1 Effective temperature .....	35
4.2 Surface gravity and microturbulence .....	35
4.3 Abundance Analysis .....	37
4.4 LTE and NLTE calculations .....	37
<b>第5章 DISCOVERY OF FIVE CARBON-ENHANCED METAL-POOR STARS FROM LAMOST .....</b>	<b>39</b>
5.1 Results and discussion .....	39
5.1.1 Chemical abundance comparison with literature data .....	39
5.1.2 Nucleosynthetic signatures of s- and r-process .....	43
5.1.3 Kinematics and dynamics .....	46

<b>第 6 章 Chemodynamical Analysis of Six Low-Metallicity Stars in the Galactic Halo</b>	51
6.1 Results and Discussion	51
6.1.1 Chemical Abundance Comparison with Literature Data	51
6.1.2 J1630+0953 and J2216+0246 Possible Progenitors	57
6.1.3 Kinematics and Dynamics	59
<b>第 7 章 Conclusions</b>	65
<b>附录 A Appendix A</b>	67
<b>附录 B Appendix B</b>	79

## 图形列表

1.1 Timeline of the universe. A representation of the evolution of the universe over 13.77 billion years. The far left depicts the earliest moment we can now probe, the far right represents the present time. Image Credits: NASA/WMAP Science Team .....	2
1.2 A schematic view of the hydrostatic equilibrium. The outward force has to balance the inward force. Only then does a star remain in equilibrium and neither collapses nor flies apart. Credits: Peter Palm .....	4
1.3 A schematic view of the Sun's structure as an illustrative example of stellar structure. Credits: NASA/Goddard .....	5
1.4 Schematic view of the proton-proton chain, fusion of four hydrogen nuclei into one helium nucleus. This fusion happened in three steps, energy is released in every step. Credits: Peter Palm .....	7
1.5 Schematic view of the CNO cycle. Helium is produced in six steps, energy is released in every step. Credits: Peter Palm .....	9
1.6 The nuclear energy generation in units of $\text{erg } g^{-1} s^{-1}$ as a function of the temperature for the p-p chain and the CNO cycle. The open circle marks the location of the sun in this diagram. Credits: LEBLANC/An introduction to stellar astrophysics .....	10
1.7 Schematic view of a massive star with over $8 M_{\odot}$ . At the end of its cosmic life, such star will have an iron-nickel core surrounded by layers of the recently produced elements. No more energy can be produced by iron fusion in its core. Credits: Peter Palm .....	12
1.8 Schematic view of the cosmic cycle of matter, stars will be formed from interstellar gas. The interstellar medium will be enriched by the elements synthesized in these stars, by either stellar winds or supernova explosions. Therefore, each successive generation of stars will be more metal-rich Credits: Peter Palm .....	16
1.9 Schematic view of the Milky Way with its different components indicated. Credits: Peter Palm .....	24
3.1 Chart-flow for the echelle reduction procedure.....	31
3.2 An illustrative example of our data reduction procedures for the major steps.	34

4.1 Our sample shown in an H-R-Diagram, based on the $T_{\text{eff}}$ and $\log g$ determined from the LIKC/APF spectra. Yale-Yonsei 12 isochrones with $[\alpha/\text{Fe}] = +0.4$ and $[\text{Fe}/\text{H}] = -2.5, -3.0, \text{ and } -3.5$ from Demarque 等 (2004) overplotted as reference. ....	36
5.1 $\log \epsilon$ lithium abundances as a function of effective temperature. Red filled star refers to J2216+2232, blue filled stars refer to the determined upper limits, and small open circles refer to the full sample of Roederer 等 (2014a). The dotted line shows the predicted primordial lithium abundance, $\log \epsilon_{Li} = 2.64$ (Spergel 等, 2007). ....	39
5.2 Left panel: $[\text{C}/\text{Fe}]$ versus luminosity for our sample stars. The dash-dotted line indicates the dividing line between carbon-enhanced and carbon-normal stars as defined in Aoki 等 (2007). The dashed line corresponds to $[\text{C}/\text{Fe}] = 1.0$ . Right panel: $[\text{C}/\text{Fe}]$ vs. $[\text{N}/\text{Fe}]$ . The two criteria for NEMP stars suggested by Pols 等 (2012) are respectively shown in dotted ( $[\text{N}/\text{Fe}] \geq 1.0$ and $[\text{N}/\text{C}] \geq 0.5$ ) and dash-dotted lines ( $[(\text{C}+\text{N})/\text{Fe}] > 0.9$ ). The filled red stars refer our sample stars. Non-carbon-enhanced objects studied by previous works (Gratton 等, 2000; Cayrel 等, 2004; Honda 等, 2004; Aoki 等, 2005) are shown by triangles up. Metal-poor stars from Spite 等 (2005) (filled diamonds), and CEMP stars from Aoki 等 (2007) (crosses) are also plotted for comparison. The candidate to CNEMP objects J2114-0616 is marked. ....	41
5.3 $[\text{Eu}/\text{Fe}]$ as a function of $[\text{Ba}/\text{Fe}]$ , the open circles are data take from saga database (Suda 等, 2008) and the magenta star refer to the position of J2114-0616. ....	42
5.4 Comparison between the light-element abundances in our sample stars (red filled star) and the literature C-normal metal-poor stars from Yong 等 (2013) (blue open circles). ....	43
5.5 Selected neutron-capture elements abundances in our sample stars (red filled stars), as a function of metallicity, compared to literature data adopted from François 等 (2007) (blue open circles). ....	44
5.6 Abundance patterns for the neutron-capture elements in our sample. The solid line represents the Solar-system s-process abundance pattern from Burris 等 (2000), scaled to match the observed abundance of Ba in each star. The dotted line represents the Solar-system r-process abundance pattern from Burris 等 (2000), scaled to match the observed abundance of Eu in each star. Note that we only include these stars with measured Ba and Eu.	45

---

5.7 Total energy vs. angular momentum in the z direction for the stars in our sample. Top panel: C-normal stars are represented by black stars, while CEMP stars are denoted by red stars. Bottom panel: the same sample of stars, with blue filled star symbols indicating CEMP-no members of the inner halo, the orange filled square symbol represents the CEMP-no and CEMP-s members of the outer halo. The green dashed curve denotes the locus of the points that possess constant apo-Galactic radius, $r_{apo} = 15$ kpc, while the golden dot-dashed horizontal lines shows the values of the energies delimiting the transition zone. ....	46
5.8 Galactocentric rotational velocity vs metallicity for the program stars color coded as in Figure 12. ....	49
6.1 Selected light-elements abundances of our sample stars (red filled stars) overlaid with [X/Fe] of carbon-normal metal-poor stars adopted from Yong 等 (2013) (blue open circles). Our derived [X/Fe] show no significant differences compared to the literature data. [C/Fe] values do not represent the carbon abundances of the natal gas. ....	52
6.2 The determined abundance ratios [Sr/Ba] of our sample stars (red filled stars), versus [Ba/Fe]. The green and blue open circles denote literature data adapted from François 等 (2007) and Yong 等 (2013), respectively. ....	53
6.3 Elemental abundance patterns for the heavy element distribution in our sample stars (filled circles denote detections, and arrow denotes $3\sigma$ upper limits derived from Eu2 line), compared with scaled solar system r- and s-process components adopted from Burris 等 (2000). The solar system r-process patterns are scaled to match Eu, and the solar system s-process patterns are scaled to match Ba. ....	54
6.4 Neutron-capture element patterns in our sample stars. Filled circles denote detections, and arrow denotes $3\sigma$ upper limits derived from Eu2 line. The dashed gray line denotes the observed abundances for the neutron-capture elements in HD122563 (Honda 等, 2006; Roederer 等, 2012). The solid red line denotes the observed abundances for the neutron-capture elements in CS 22892–052 (Sneden 等, 2003, 2009; Roederer 等, 2009). The dotted blue line denotes predicted yields from s-process nucleosynthesis in TP-AGB stars (Sneden 等, 2008; Bisterzo 等, 2011). The physical meaning of these three lines are discussed in the text. ....	55

6.5 Dtrans as a function of [Fe/H] for our target stars, compared with Yong 等 (2013). The solid green line denotes the scaled solar pattern, the red dashed line denotes the limit of Dtrans based on the model described in Frebel et al. (2007), and the red dotted lines show the uncertainty of the model. The shaded area is the Forbidden Zone, where there is insufficient C and O induced cooling for low-mass star formation. ....	56
6.6 The determined [X/H] abundance ratios of J1630+0953 (left panel) and J2216+0246 (right panel) as a function of atomic number, overlaid with simulated abundance patterns by several best fit models, transparent by their fractional appearance. The best fits and their properties are discussed in the text. ....	57
6.7 Posterior Distributions for $\chi^2$ , of the 10,000 simulations, for J1630+0953 (left panel) and J2216+0246 (right panel). The median and median absolute deviation (MAD) are shown in legends. ....	58
6.8 The left panel shows the Galactic velocities and the right panel shows the orbital parameters for our sample stars as functions of [Fe/H]. The y-axis error bars denote the 16 <sup>th</sup> and 84 <sup>th</sup> percentiles, while the x-axis error bars represent a typical [Fe/H] uncertainty (0.10 ~dex). ....	60
6.9 Lindblad diagram for program stars and data taken from Paper I. Top panel shows the distribution of this sample based on [C/Fe] abundance ratios, carbon normal (black stars) and CEMP stars (red stars). Bottom panel shows the distribution of this sample based on Carollo 等 (2014) criterion. CEMP-no stars are shown as blue filled star, CEMP-r/s as orange filled square, and C-normal stars as black filled star. The green dashed curve represents the locus of the points that possess constant apo-Galactic radius, $r_{apo} = 15$ kpc. The light-gray shaded area encloses the transition zone energies. ....	63

## 表格列表



## 第1章 Introduction

Roughly 20 years had passed since our kindergarten teacher sang that song “Twinkle, twinkle, little star ★★★ How I wonder what you are ★★★ Up above the world so high ★★★ Like a diamond in the sky”. This song triggered my curiosity and led me to ask: what is a star, why it twinkles, and why it is small? This is how my passion for astronomy has started. Before gaining insight into the many details and the dominant physical and chemical processes in the universe, and for the convenience of the reader; it is worth to start this letter by a brief introduction to the history of our universe, its evolution, and definition of some of the fundamental astronomical terminology.

Several popular theories are explaining the origin of our universe (e.g., The Big Bang, the Steady State, and the Oscillating Universe). Nevertheless, it is widely acknowledged that the Big Bang is responsible for the creation of the present cosmos we know. In brief, the Big Bang theory claims that all of the present matter in our universe began as an extremely hot, very dense and very tiny particle (the so-called Singularity [Mitton, 1977](#))<sup>1</sup>. The theory’s name sometimes might be misunderstood, since there was no explosion rather than an expansion in the space everywhere in the universe ([McCrea, 1970](#); [Silk, 1980](#)). The big bang estimates that this expansion happened 13.8 billion years ago. Many cosmologists studied the cosmic microwave background, which reserves a fossil signature of the light and radiation remaining from the Big Bang. This evidence of the Big Bang diffuses in the universe and is noticeable to the microwave detectors, which enables scientists to possible signs of the very early universe.

In the very early second ( $10^{-41}$  s) after the Big Bang, our universe underwent an extreme burst of expansion, this incredible growth spurt known as the universe inflation ([Page, 1983](#); [Ford, 1987](#); [Dolgov 等, 1990](#)). With time our universe kept expanding and cooling down, which allows the elementary particles to form, this is known as the quarks epoch ( $10^{-12}$  s) ([Hawkins, 1962](#); [Harrison, 1967](#); [Parker, 1969](#); [Collins 和 Hawking,](#)

---

<sup>1</sup>Singularity is a mathematical concept of infinite temperature and infinite density packed into a single point of space.

1973; Ellis 等, 1978; Linde, 1984; Efstathiou 等, 1990). This continuous expansion and cooling process allows hadrons, leptons, protons, neutrons, photons, and deuterium<sup>2</sup> to form (1s to three minutes after the Big Bang, Koebke, 1973; Ignat'ev 等, 1979; Turner 和 Schramm, 1979).

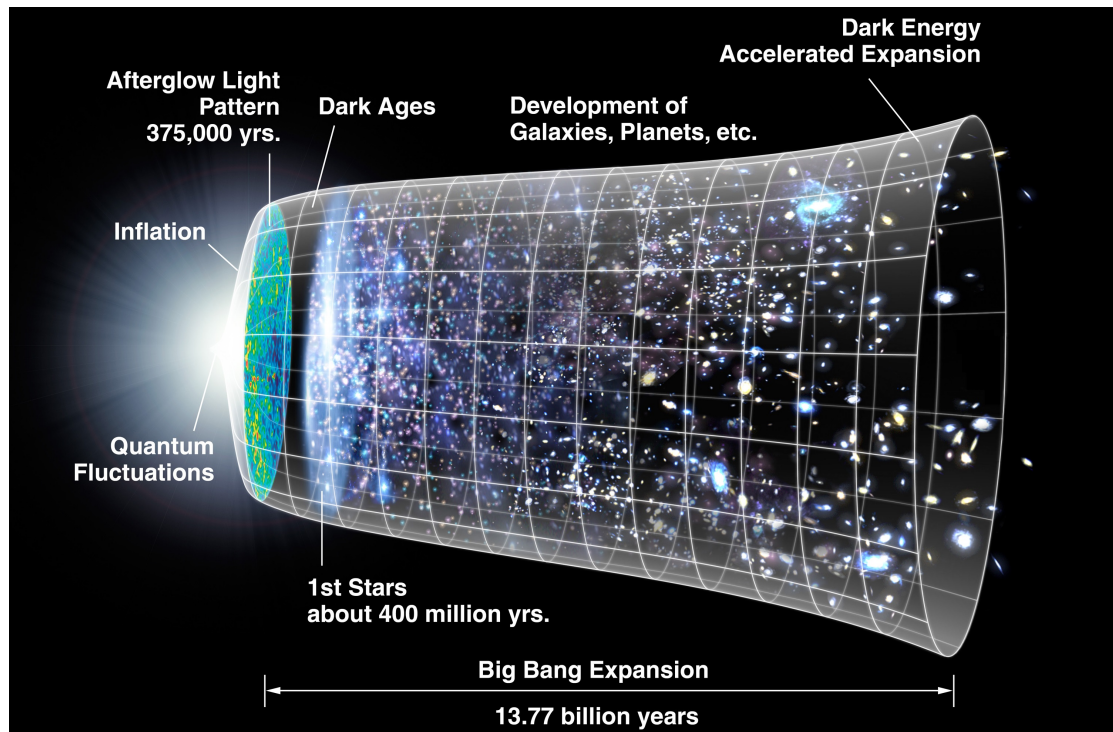


**图 1.1 Timeline of the universe. A representation of the evolution of the universe over 13.77 billion years. The far left depicts the earliest moment we can now probe, the far right represents the present time. Image Credits: NASA/WMAP Science Team**

The first helium nuclei has been synthesized from deuterium. At the same time, helium also can be synthesized, at higher temperatures, directly from four protons (Mozel, 2000; Pagel, 2000). However, these helium nuclei (synthesized from four protons) were instantly annihilated by the highly energetic gamma rays, making the deuterium detour as the dominant source of the helium nucleosynthesis (Greenstein, 1969; Ginzburg, 1969; Alvarez 和 Hakim, 1979). Lithium (the third element in the periodic table) was formed from the collisions of several helium nuclei. In other words, our universe, three minutes after the Big Bang, was built up of three fundamental elements: hydrogen, helium, and trace amount of lithium, with an approximate fractions 75% hydrogen, 75%

<sup>2</sup>Deuterium is also called “heavy hydrogen” because it has the same atomic number as hydrogen, but it is composed of one proton and one neutron.

helium, and merely 0.00000002% lithium (Deliyannis 等, 1990; Ryan, 2000; Murdin, 2000). Afterwards, the universe cooled down enough to allow electrons (belongs to the lepton family) and protons to bound and form the first neutral atoms (hydrogen), this is known as the recombination epoch (100,000 years after the Big Bang) (Dodelson 和 Jubas, 1991; Tegmark, 1994; Puy 和 Signore, 1996; Galli 和 Palla, 2000). About 150 million to 1 billion later, the temperature of the universe had dropped to  $-270^{\circ}\text{C}$  allowing the earliest structures (known as population III stars) to form (Bond, 1981; Ober 等, 1982; Bond 等, 1983; Arimoto, 1983; Silk, 1984; Argast 等, 2000). Figure 1.1 demonstrates the evolution, of the observable part, of our universe from the Big Bang to the present.

The previous two paragraphs try to summary the first phase of the element synthesis. The temperature of our universe had been cooled down too far, and heavier elements couldn't been synthesized from nuclear fusion with hydrogen, helium, and lithium. Nevertheless, our universe was still lacking the elements required to support life (e.g., carbon, nitrogen, oxygen), as well as the remaining elements in the periodic table. These elements were eventually built up, inside stars over billions of years. Therefore, and for the convenience of the reader a brief introduction to stars formation, stellar structure, and stellar evolutions are needed.

## 1.1 Stars Formation

The interior of the main-sequence (MS) or giant stars is in hydrostatic equilibrium; the balanced forces are an inward gravitational force and an outward nuclear force, with a temperature of the order of  $10^7\text{ K}$  (LeBlanc, 2010). The thermodynamic conditions, characterized by the variables temperature and pressure, are sufficient for nuclear fusion to occur, which in term lead to produce adequate energy preventing any further collapse of the star. Stars have very different structures, as they evolve in their lives; however, MS stars have a general structure that is roughly the same and can be illustrated by our sun (see Figure 1.3). Like all stars, our sun is mainly made up of hydrogen and helium, with main parts as follow (Gibson, 1972):

**Interior** : This is the part of the star which is below its surface and cannot be directly

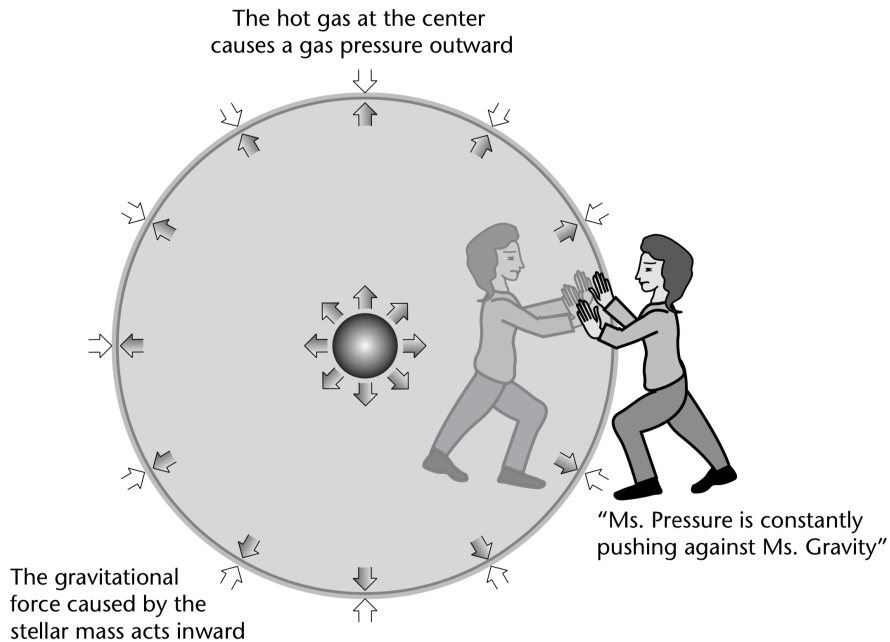


**图 1.2 A schematic view of the hydrostatic equilibrium. The outward force has to balance the inward force. Only then does a star remain in equilibrium and neither collapses nor flies apart. Credits: Peter Palm**

seen ([Archontis 和 Vlahos, 2019](#)). Depending on the types of transport of energy, which is in action, the stellar interiors can be divided into:

1. **The Core:** This is the region located inside the star where temperature and pressure are sufficient to ignite nuclear fusion. The process of converting hydrogen into helium and the release of a tremendous amount of energy occurs in the core. More massive stars will have larger, hotter cores (e.g., [Paczynski, 1970](#); [Voronchev, 2019](#)).
2. **The Radiative Zone:** This is the region where energy transportation is dominated by electromagnetic radiation (gamma rays). The radiative zone extends from a depth of 515,000 km to 200,000 km, concerning the surface of the Sun (e.g., [Menou 和 Le Mer, 2006](#)).
3. **The Convection Zone:** Here the energy transport mechanism is convection. This zone is the outermost layer of the interior, and it extends from 200,000 km up to the visible surface (e.g., [Hotta 等, 2018](#); [Yang 等, 2018](#)).

**Photosphere :** Looking to the Sun, the view becomes more and more opaque, just like

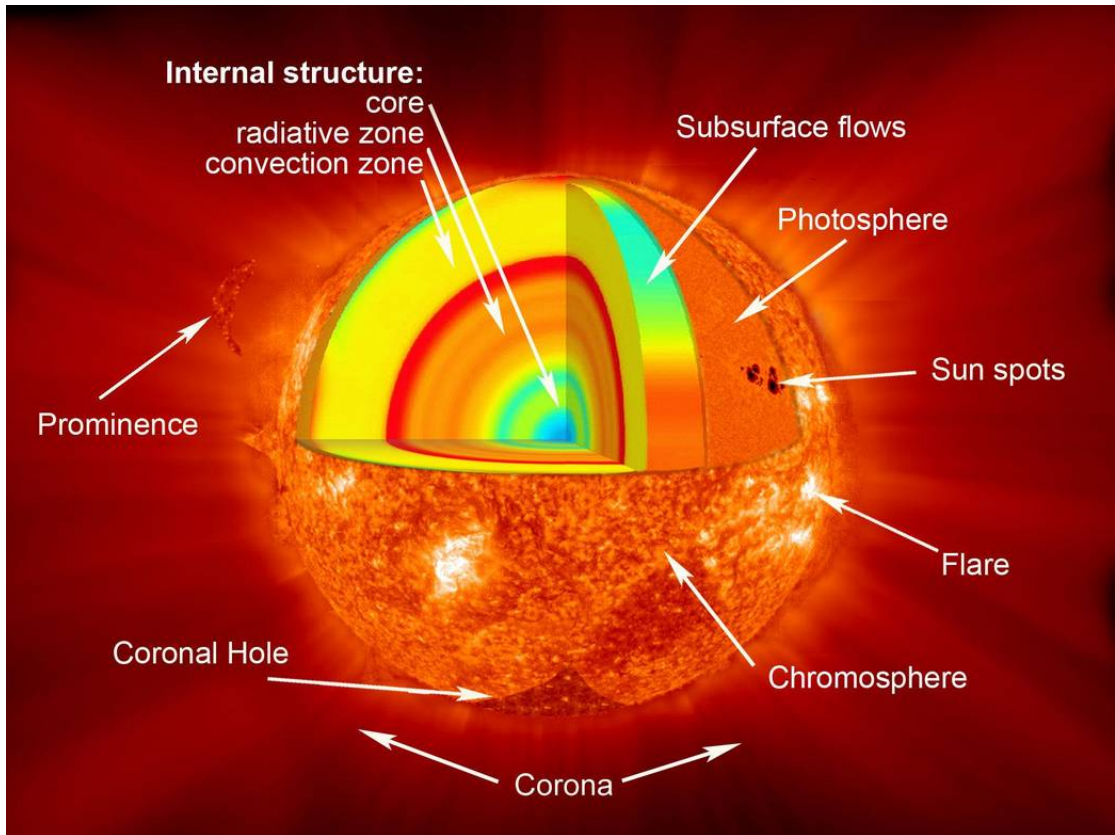


图 1.3 A schematic view of the Sun's structure as an illustrative example of stellar structure.

Credits: NASA/Goddard

seas. The point where the Sun appears to become completely opaque is called the photosphere. Thus, the photosphere may be thought of as the imaginary surface from which the solar light that we see appears to be emitted (e.g., Jurčák 等, 2018; Kessar 等, 2019).

**Atmosphere :** This is the outer part of the sun, where the gamma rays finally reach the space.

## 1.2 Stellar Evolutions

Fusion is the dominant type of nuclear reactions occurring in stars. Inside the cores of these stars, a variety of different nuclear fusion reactions occur, upon their mass and composition. The resulting atomic nuclei, in term of mass, are lighter than the sum of the reactant elements. This mass difference is released as electromagnetic energy according to the well known Einstein's relation for the equivalence between energy and mass ( $E = Mc^2$ ). Based on the dominate fusion nuclear reactions, stars have different

stellar evolutionary phases. Here, we try to give brief introduction to these phases.

### 1.2.1 H-Burning Phase

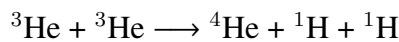
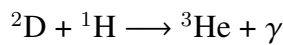
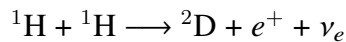
The H-burning mechanism is primarily the nuclear fusion of four hydrogen nuclei ( $^1\text{H}$ ) into one helium nucleus ( $^4\text{He}$ ). The amount of this fuel (hydrogen) is consumed at a lower rate than in any other evolutionary phase; therefore, the H-burning lifetime, for all stars, is longer than the other evolutionary phases (e.g., the H-burning phase is longer by a factor of 100 than the He-burning stage) (e.g., [Chieffi, 2010](#)). The fusion of these four H nuclei can be achieved through two possible reaction chains (namely the p-p chain and the CNO cycle, [Borexino Collaboration 等, 2018](#); [Wiescher, 2018](#)). These two reaction chains usually occur simultaneously, but with relative efficiencies, depending on the stellar mass and the temperature of its core (e.g., [Castellani 等, 1990](#)).

#### 1.2.1.1 The p-p Chain

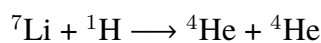
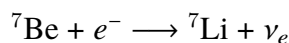
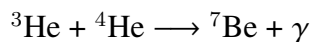
The first reaction in the p-p chain (pp I) requires that protons experience a  $\beta^+$  decay; since it is impossible to form a bound system with two protons. This reaction can occur only if the protons are brought together by a nuclear collision (see Figure 1.4). During this short timescale collision, one of these collided protons has the chance to  $\beta^+$  decay, and then convert into a neutron, a positron, and a neutrino. The neutron can then be captured by the other proton to form a deuteron. This process is governed by weak interaction and therefore has a low probability of occurring; its cross-section is in fact quite low ( $\approx 10^{-23}$  barn; 1 barn =  $10^{-24}$  cm $^2$ ). The pp I chain therefore begins to be important only when the core temperature is of the order of  $5 \times 10^6$  K ([Borexino Collaboration 等, 2018](#)). Until a temperature of the order  $8 \times 10^6$  K is reached, the reactions producing  $^3\text{He}$  are more frequent than those consuming  $^3\text{He}$  and as a consequence the abundance of  $^3\text{He}$  increases. When this temperature is achieved, the nuclear reactions  $^3\text{He} + ^3\text{He}$  and  $^3\text{He} + ^4\text{He}$  become effective, so decreasing the  $^3\text{He}$  abundance. The relative frequency of pp II and pp III depends strongly on the temperature. In particular, the  $^3\text{He} + ^4\text{He}$  reaction becomes competitive with respect to  $^3\text{He} + ^3\text{He}$  for  $T \approx 15 \times 10^6$  K ([LeBlanc, 2010](#)). As a general rule, with increasing temperature the importance of the pp II and pp III increases with respect to pp I if there

is a sufficient concentration of the  $^4\text{He}$  (either produced by the pp I or primordial). In addition, pp III gradually becomes more important than pp II.

### pp I



### pp II



### pp III

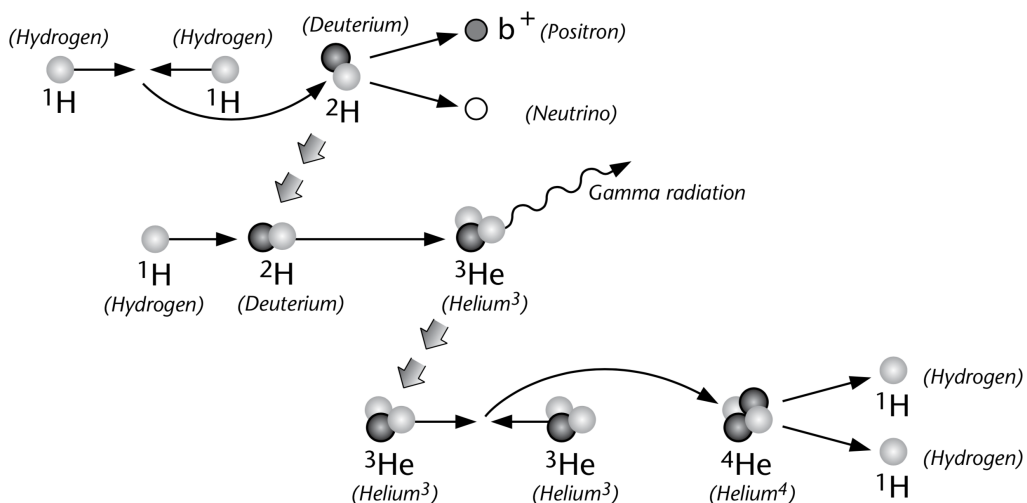
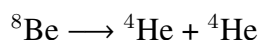
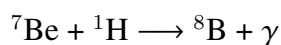
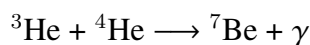


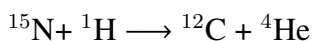
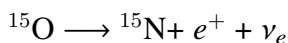
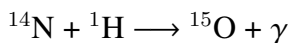
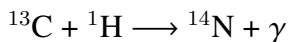
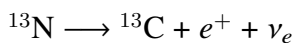
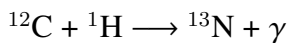
图 1.4 Schematic view of the proton-proton chain, fusion of four hydrogen nuclei into one helium nucleus. This fusion happened in three steps, energy is released in every step.

Credits: Peter Palm

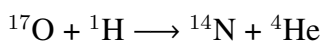
### 1.2.1.2 The CNO Cycle

The CNO cycle is a combination of two separate cycles; CN cycle and NO cycle (see Figure 1.5). The existence of some isotopes (e.g.,  $^{12}\text{C}$ ,  $^{15}\text{N}$ ,  $^{16}\text{O}$ ) are crucial for either cycles to take place (see below the reaction networks involved in this process, [Wiescher, 2018](#)). Carbon and nitrogen are subject to be produced and destroyed throughout these cycles; these elements play the role of catalysts. In the CN cycle, the isotopes of C and N act as catalysts, and so behave as "secondary elements". As a consequence the cycle can start almost from any reaction if the involved isotope is present, and during a complete loop around the cycle the isotope is consumed and then produced again.

#### CN cycle



#### NO cycle



However, this does not mean that the concentrations of the different isotopes will be unchanged as the final abundances depend strongly on the relative rates of the nuclear reactions in the cycle. Only at a high enough temperature ( $T \approx 15 \times 10^6 \text{ K}$ ) the isotopes achieve their equilibrium abundance; the rate of the production is exactly equal to the rate of the destruction. At this point, the abundance of each isotope is inversely proportional to the nuclear cross-section of its destruction. Hence the slowest reaction of the CNO cycle is  $^{14}\text{N}(p,\gamma)^{15}\text{O}$ , because it has the largest cross-section. <sup>3</sup>. The most abundant

<sup>3</sup>Here we have introduced the compact notation  $^{14}\text{N}(p,\gamma)^{15}\text{O}$  instead of  $^{14}\text{N} + ^1\text{H} \longrightarrow ^{15}\text{O} + \gamma$

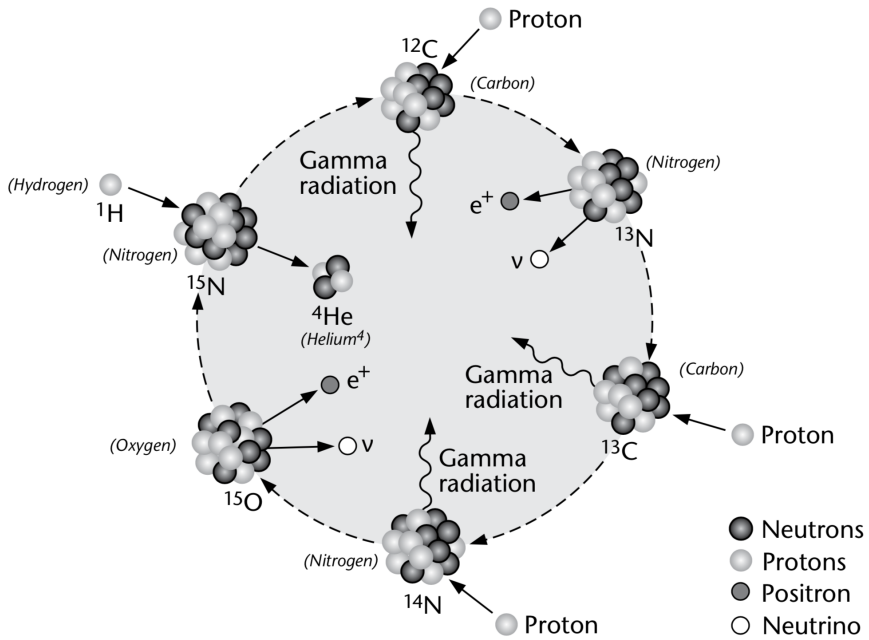


**图 1.5 Schematic view of the CNO cycle. Helium is produced in six steps, energy is released in every step. Credits: Peter Palm**

element in the CNO cycle processed material is  $^{14}\text{N}$  (Sasaki 等, 2016). The branching ratio of the proton captures by  $^{15}\text{N}$ , producing respectively  $^{16}\text{O}$  and  $^{12}\text{C}$ , is of the order of  $10^{-4}$  (Wiescher, 2018), thus the amount of  $^{16}\text{O}$  produced by proton capture on  $^{15}\text{N}$  is negligible. Nevertheless, the small production of  $^{16}\text{O}$  through this channel is important because it allows the  $^{16}\text{O}$  nuclei originally present to take part in the cycle as well, as they are transformed into nitrogen via the NO cycle (Sasaki 等, 2016; Wiescher, 2018). The temperature sensitivity of the complete CNO cycle is much larger than that of the p-p chain, where  $\epsilon_{CNO} \propto T^{18}$  at  $T \approx 10 \times 10^6 \text{ K}$ . This means that the p-p chain dominates at low temperatures ( $T \leq 15 \times 10^6 \text{ K}$ ) in stars with mass lower than  $\approx 1.3 M_\odot$ , while the CNO cycle dominates at higher temperatures for larger stellar masses. In Figure 1.6, the trends of both  $\epsilon_{pp}$  and  $\epsilon_{CNO}$  with temperature are shown. At the center of the sun  $\epsilon_{pp}/\epsilon_{CNO} \approx 10$ , so that the contribution of the CNO cycle to the whole energy budget is of the order of 10 per cent (Caciolli 等, 2011; Sasaki 等, 2016; Wiescher, 2018).

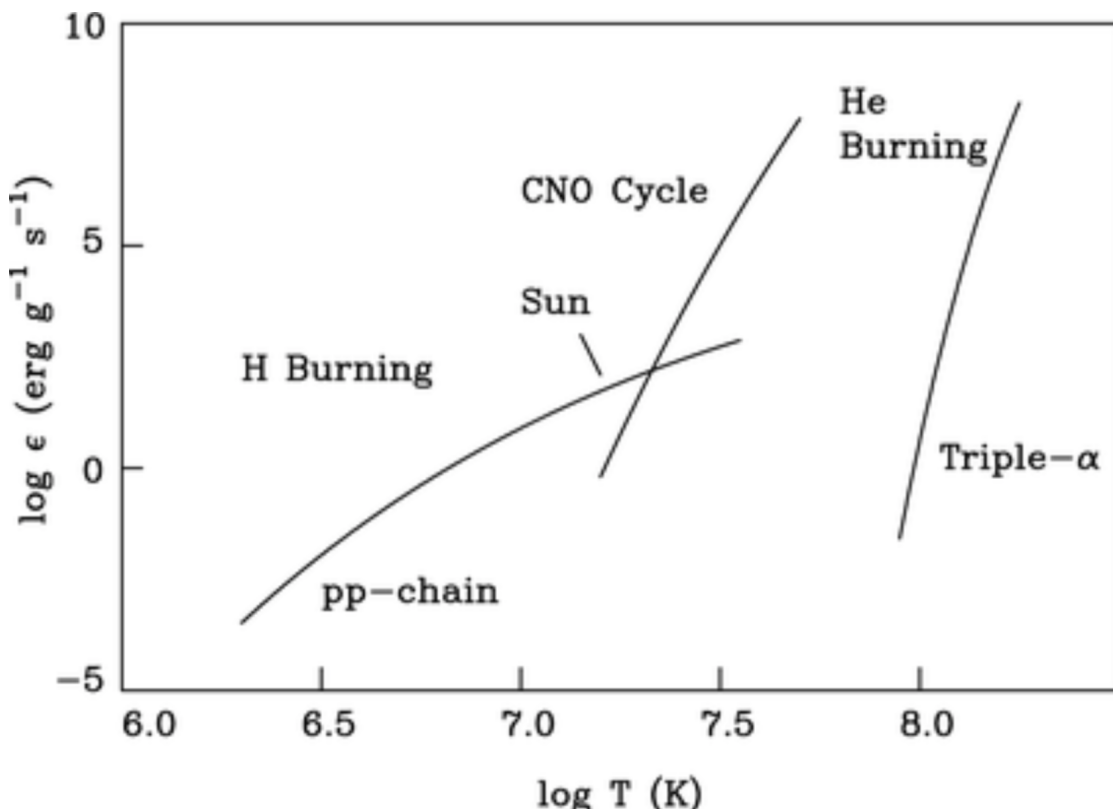
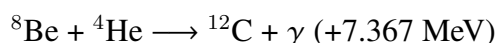
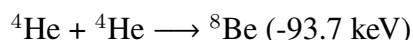


图 1.6 The nuclear energy generation in units of  $\text{erg g}^{-1} \text{s}^{-1}$  as a function of the temperature for the p-p chain and the CNO cycle. The open circle marks the location of the sun in this diagram. Credits: LEBLANC/An introduction to stellar astrophysics

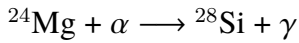
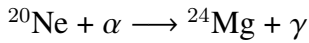
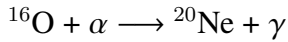
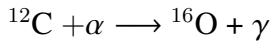
### 1.2.2 The Helium Burning Phase

The helium burning phase is the second stage of a stellar evolution. Unlike during the H-burning phase (discussed previously), the nuclear-physical processes at work in stars of different masses, during the main core He-burning stage are quite similar. The first and fundamental reaction in the He-burning process is the production of  $^{12}\text{C}$  from the fusion of three  $^4\text{He}$  nuclei. This reaction is called the triple alpha ( $3\alpha$ ) reaction (see Figure 1.6). A triple collision being of very low probability, this reaction usually occurs in two separate steps (Hoyle 和 Schwarzschild, 1955; Hayashi 和 Cameron, 1960; Iben 和 Rood, 1970; Woosley, 2019).



The first reaction is endothermic or endoergic, meaning that in a short time, ( $\sim$

$10^{-16}\text{s}$ )  $^8\text{Be}$  decays back into two  $\alpha$  particles. The possibility of the second reaction is therefore extremely low. However, when the interior temperature rises (of the order of  $\sim 1.2 \times 10^8\text{K}$ ) the probability of the second reaction increases (Tur 等, 2010; de Diego 等, 2011; Adams 和 Grohs, 2017; Huang 等, 2019). The other nuclear reactions involved in the He-burning process are:



Only the first two reactions, together with the  $3\alpha$  reaction, are really important, a relevant consequence of the He-burning process is to transform He into a mixture of  $^{12}\text{C}$  and  $^{16}\text{O}$  with traces of  $^{20}\text{Ne}$ . Unfortunately, the alpha capture by  $^{12}\text{C}$  has a resonance and a very low cross-section ( $\sim 10^{-17}$  barn) at low energies. Consequently the nuclear parameters are difficult to measure experimentally or to calculate by theoretical analysis.

### 1.2.3 The Advance Evolutionary Phase

The giant onion is the next evolutionary phase ; after the exhaustion of Helium in the core. This phase is well clear in the asymptotic giant branch (AGB) stars <sup>4</sup>. After He-exhaustion, He-burning shifts to shell around the CO core, whose mass size increases as consequence of the convection of helium to carbon and oxygen in the He-burning shell (Hayashi 和 Cameron, 1962a,b; Sugimoto 等, 1968; Lamb 等, 1976; Sugimoto, 1970; Iben 等, 1997; Siess, 2006). The overlying H-burning shell, which has burnt outwards for some time, extinguishes due to the expansion and consequence drop of its temperature. The latter drop is caused by the onset of He-burning in the shell. In low-mass stars, the onset of the He-burning induces a temporary drop of the surface luminosity and the star crosses the same region of the H-R diagram three times (as during the RGB bump phase). As a consequence, there is a good probability of observing an

<sup>4</sup>corresponds to the He-shell burning phase. The designation asymptotic comes from the fact that in low-mass AGB stars, the effective temperature-luminosity relationship is very similar, a little bit slightly hotter, to that of low-mass stars, the so-called red giant branch stars (RGB) stars. For more massive stars the term asymptotic has no morphological significance

AGB star during this phase, which is called the AGB clump. This is indeed the case in well-populated old galactic stellar system ([Castellani 等, 1991](#); [deg'l'Innocenti 等, 2001](#)). In these stars, the large energy flux produced by the He-burning shell causes the base of the H-rich shell to expand and cool, so that H-burning in the shell immediately is switched off. When this occurs, the outer convection zone penetrates inward, into the H-depleted zone. This process is known as the second dredge up ([Becker 和 Iben, 1979](#)). For lower mass objects, H-burning remains quite efficient, and prevents the outer convection from penetrating deeper into the star (therefore the second dredge up dose not occur, [Becker 和 Iben, 1979](#)).

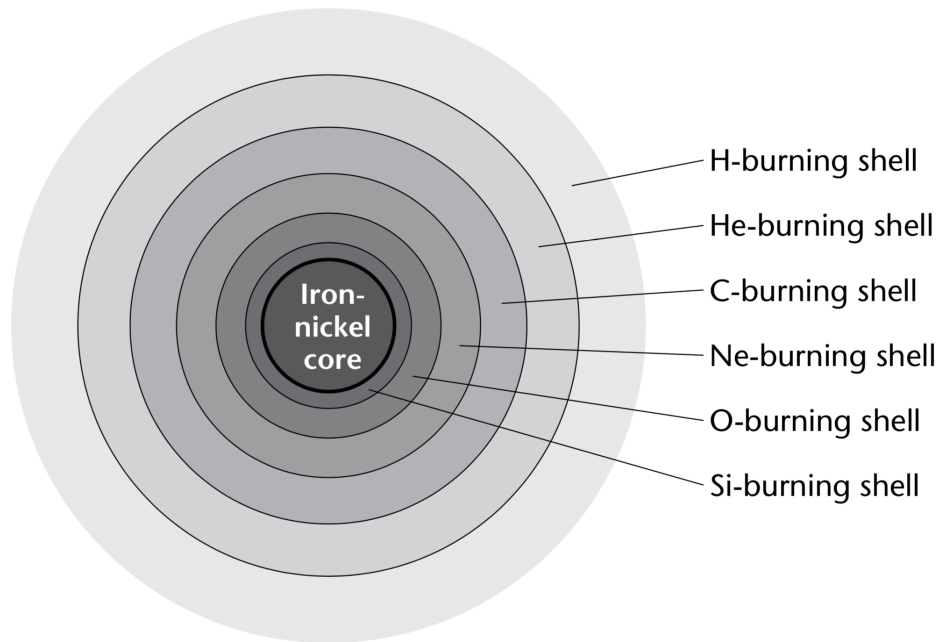


**图 1.7 Schematic view of a massive star with over  $8 M_{\odot}$ . At the end of its cosmic life, such star will have an iron-nickel core surrounded by layers of the recently produced elements. No more energy can be produced by iron fusion in its core. Credits: Peter Palm**

### 1.3 Stellar Populations

There are lots and lots of stars in our Milky Way, likely between 200 and 400  $\times 10^9$  stars (Roth, 2006). Section 1.1 assumes that our universe has an age of  $13.8 \times 10^9$  years ( $165.6 \times 10^9$  months), making a roughly average of one birth per month. Elements are continuously synthesized in all this enormous number of stars, invariably driving chemical evolution onward. Sections 1.1 and 1.2 discuss how stars form and evolve. However, the entire population of stars is like a bustling astronomical menagerie that includes quite a several unusual species besides any ingrained animals. In spite of the fact that it does not all the times appear as before-mentioned; at the moment you are looking at the sky or pictures of stars, there is enormous diversity with each other. Simply as in any handful of people or animals; stars can be classified as younger and elder (in term of age) or larger and smaller (in term of mass). In contrast, a star can change its size. All stars, near the end of their lives, expand toward an evolutionary phase known as red giants. The red giant star "Betelgeuse<sup>5</sup>", has a radius of 1,200 times our Sun's radius; because it is at its stellar deathbed (Kervella 等, 2018).

The stellar size of a star doesn't inevitably indicate anything about its stellar mass, in any case. However, stellar mass is an essential quantity in astrophysics. As an illustrative example, our Sun has a stellar mass of  $2 \times 10^{30}$  kg (roughly  $3 \times 10^5$  the mass of Earth, E Smith 和 Zuber, 2017; Caerols 和 Asenjo, 2019), which serves as an astronomical unit to measure stellar masses (the so-called solar mass). Moreover, stellar masses have a broad range, the smallest stellar mass is about 0.1 solar mass; the minimum mass allows stars to ignite nuclear fusions at their cores. Usually, the term "low-mass star" refers to stars with stellar masses less than  $2 M_{\odot}$ . Stars with stellar masses of  $2\text{-}8 M_{\odot}$  are "intermediate-mass stars". Stars with stellar masses of 8 or more  $M_{\odot}$  are "massive stars". Low-mass stars are much more, number-wise, than massive ones. Statistically, for each massive star ( $M < M_{\odot}$ ), there are  $10^3$  intermediate-mass and  $10^4$  low-mass stars. The vast majority of the stars have stellar masses significantly

<sup>5</sup>Betelgeuse is the tenth brightest star in the night sky before "Hadar" and after "Achernar", and the second-brightest in the constellation of Orion after "Alnilam". It is a reddish, semi-regular variable star, with apparent magnitude alters between +0.0 and +1.3.

less than  $1 M_{\odot}$ ; such as  $0.3 M_{\odot}$  or even lower ([Orcajo 等, 2019](#)).

The chemical composition of stellar objects is an often used distinguishing feature (the so-called star metallicity;  $[Fe/H]$ <sup>6</sup>). The vast majority of stars have chemical compositions similar to that observed in our (metal-rich) Sun. However, few rare stars have lower metallicities—the poorer the star is, the more unique the star is; because it originates from the very early era of the universe, more than  $10 \times 10^9$  years ago. These stars are known as metal-poor stars.

### 1.3.1 The first stars

As reported by many cosmological simulations, the very first stars were created in small mini-halos some several hundred million years later the Big Bang. The primordial gas, left after the Big Bang, lacked sufficient cooling agents (e.g., carbon, oxygen, and silicon); therefore, significant fragmentation was mainly overcome so that the first stellar objects were extremely massive (of the order to  $100 M_{\odot}$ ). However, this is a different case compared with low-mass stars, ruling today's mass function (IMF). These stellar objects are introduced as Population III or Pop III stars, as they have been formed from primordial (metal-free) gas ([Puget 和 Heyvaerts, 1980](#); [Carr, 1987](#); [Hara 和 Miyoshi, 1988](#); [de Araujo 和 Opher, 1990](#); [Welsh 等, 2019](#)). These stellar objects shortly exploded as supernovae (SNe) to either collapse into black holes (progenitor masses of  $25 < M_{\odot} < 140$  and  $M_{\odot} > 260$ ) or to die as energetic pair-instability SNe (PISN;  $140 < M_{\odot} < 260$ ; [Heger 和 Woosley, 2002](#)). During their explosions, these stellar objects provided huge amounts of ionizing emissions (the PISNe also contributes some of the first metals) that altered the surrounding environment; hence the second generation (Population II or Pop II) stars might be less massive ( $M_{\star} \sim 10 M_{\odot}$ ) and long-lived object.

Partially, the ionized stellar gas, which its chemical composition has been altered by the death of the first stars, will support the formation of H<sub>2</sub> and the HD molecule. This, in turn, will facilitate additional effective cooling agents than what is available in zero-metal gas. In addition, the metals or the dust grains, which has been left behind

<sup>6</sup> $[A/B] = \log(N_A/N_B)_{\star} - \log(N_A/N_B)_{\odot}$ , where N is the number density of atoms of a given element in the star ( $\star$ ) and the Sun ( $\odot$ ), respectively.

from PISNe would have the same cooling effects as well. In spite of the fact that not all more massive SNe end in black hole creation. In spite of the fact that not all more massive SNe end in black hole creation, some massive ( $25 M_{\odot}$ ) stars experience solely a partial fall-back; some of the lately synthesized metals get expelled into the surrounding stellar gas (e.g., [Umeda 和 Nomoto, 2003](#)). At that point, enough metals will present to guarantee enough gas fragmentation to support the low-mass ( $<1 M_{\odot}$ ) star formation. These stars, which has been, formed from non-zero (any metal-enriched) stellar gas are known as Population II (Pop II) stars (see Figure 1.8). Besides, higher metal-rich stars (e.g., our Sun), which have been formed in more metal-rich environments are called Population I (Pop I). Stellar archaeology claims that the PopII stars preserve in their atmosphere the composition of the individual SN yields of the previous Pop III (the so called Pop III chemical fingerprint). Therefore, metal-poor stars can contribute to reveal the first nucleosynthesis enrichment in the universe ([Beers 和 Christlieb, 2005](#); [Aoki 等, 2007](#); [Hansen 等, 2016a](#); [Placco 等, 2016](#); [Kielty 等, 2017](#); [Roriz 等, 2017](#); [Cruz 等, 2018](#); [Caffau 等, 2018](#); [Mardini 等, 2019a,b,c](#)).

### 1.3.2 Metal-poor stars

We have mentioned that the first stars (pop III) have been formed from a pristine (zero-metal) gas cloud, shortly after the Big Bang. These stars were thought to be very massive; the absence of sufficient cooling agents (e.g., [Bromm 等, 2002](#)). However, these stars exploded to enrich its surroundings and allow gas fragmentation to support the low-mass ( $<1 M_{\odot}$ ) formation. The nowadays observed metal-poor stars belong to this stellar era. In their atmospheric surface, these stars store information about the chemical composition of their stellar gas cloud. They are providing archaeological data of the most primitive times of our universe. The chemical abundance patterns observed in their atmosphere present unique full information about the formation and evolution of our universe. These pieces of knowledge are valuable for the understanding of the galactic chemical evolution and formation. Metal-poor stars are our neighbors corresponding to the high-redshift universe (e.g., [Senchyna 等, 2019](#)).

The justification for investigating metal-poor stars is that they are long-lived, low-mass stellar objects, the vast majority of the investigated metal-poor stars, in literature,

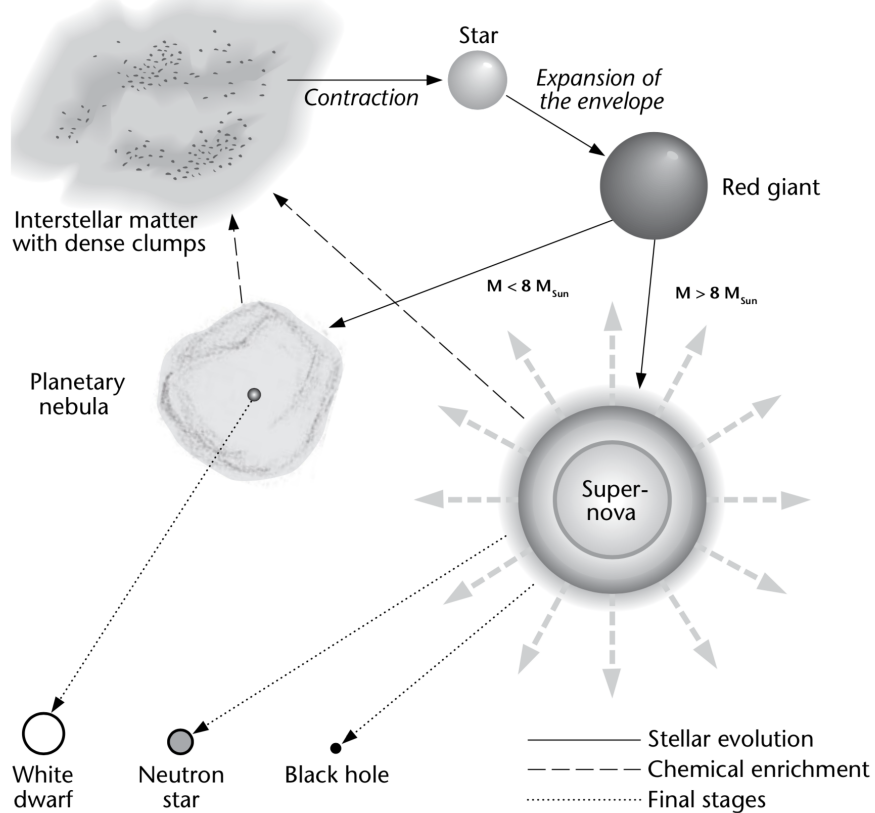


**图 1.8 Schematic view of the cosmic cycle of matter, stars will be formed from interstellar gas.**

**The interstellar medium will be enriched by the elements synthesized in these stars, by either stellar winds or supernova explosions. Therefore, each successive generation of stars will be more metal-rich Credits: Peter Palm**

are main-sequence (MS) and giant stars that have not altered their atmospheric chemical composition and thus preserved the chemical signatures of their birth stellar gas cloud. Assuming that the entire universe was mostly lacking metals at its earliest eras, it is commonly believed (and carried out by investigation) that low metallicity star means and old age star; their masses are of order  $0.6\text{--}0.8 M_{\odot}$  (massive stars consume their fuels faster, therefore die more quickly). By analyzing the current chemical composition of their atmospheric surface, one can travel back in time to the early universe period and learn about its nature. However, metal-poor stars can experience some internal mixing processes or accretion of interstellar material, which would alter the original atmospheric surface abundance. Such an assumption is vital in the metal-poor stars analyses. This field of study, in astronomy and astrophysics, is usually referred to

as “near-field cosmology” or “stellar archaeology” (Christlieb 等, 2002; Umeda 和 Nomoto, 2003; Frebel 等, 2005; Tominaga 等, 2007; Heger 和 Woosley, 2010; Caffau 等, 2011; Ito 等, 2013; Nomoto 等, 2013; Placco 等, 2014a; Keller 等, 2014; Tominaga 等, 2014; Hansen 等, 2016b; Starkenburg 等, 2018; Ezzeddine 等, 2019). The best candidates for such studies are the very metal-poor ( $[Fe/H] < -2.0$ , hereafter VMP), extremely metal-poor ( $[Fe/H] < -3.0$ , hereafter EMP), and ultra metal-poor ( $[Fe/H] < -4.0$ , hereafter UMP) stars. These second-generation objects (Pop II) have formed from low-metallicity gas clouds at redshift  $\gtrsim 6$

The ultimate rationale for studying metal-poor is to gain insights into the early universe. However, still there are many other justifications, here we try to mention the most important of these reasons for analyzing metal-poor stars.

1. The most metal-deficient stars (ultra metal-poor), with no enhancement in the heavy elements ( $Z > 3$ ) abundances, are believed to be the most primitive stars observed until now.
2. The lithium ( $Z = 3$ ) abundances observed in main-sequence-turnoff extreme metal-poor ( $[Fe/H] < -3$ ) have the great potential to place direct constraints on the physical and chemical conditions of the Big Bang.
3. The redshifts epochs  $> 6$  are believed to be the era where the most metal-deficient stellar objects have been formed, and the best candidate to examine the physical and chemical conditions at the time the very first heavy element was built.
4. Metal-poor stars constrain our perception of the nature of the very first stars (Pop III), the initial mass function (IMF), the explosion of supernovae, and how the Pop III ejecta was incorporated into succeeding early stars.
5. The direct comparison of the predicted yields of stellar evolution models and/or the galactic chemical enrichment scenarios significantly constrain the science of the creation and development of the very first stars/galaxies.
6. Some of the metal-poor stars ( $[Fe/H] \sim 3.0$ ) show strong enhancements in the neutron-capture elements, that the detection of Th ( $Z= 90$ ) and U ( $Z= 92$ ) is likely possible and thus the estimation of their age and the universe.
7. Metal-Poor stars with  $[Fe/H] -0.5$  (Hyper metal-poor) acquaint our perception

of the Milky Way growth; the connections between chemical abundance, kinematics and dynamics, and the age distributions, the defining properties of stellar groups, allow votes among the different models of how the Milky Way system formed and has grown.

### 1.3.3 The diversity of the observed chemical abundances of metal-poor stars

For a long, long time, we believed that all field stars would likely show chemical composition similar to our Sun. This assumption came to its end in the mid of the nineteenth century (1940), at the moment that some metal lines detected in stars seemed to be surprisingly weak corresponded with our Sun. The first explanation was that these stars would have peculiar atmospheres or they are hydrogen-deficient stars. However, Chamberlain 和 Aller (1951) presumed that these unique stars would be the foresight of abnormally low amounts of calcium and iron, in their work, they found  $\sim 1/20$ th the solar values. Following studies on before-mentioned stars through the subsequent few decades proved that some stars do certainly have different metallicities that reveal various phases of the chemical evolution experienced by our Milky Way. Chamberlain 和 Aller (1951) observed many stars, including HD140282, which has been a point of many studies in the previous half-century. For example, Norris 等 (2001) studied HD140282 and reported that this subgiant star has peculiar chemical composition with  $[Fe/H]=2.5$ . For the convenience of the reader, and the view of this thesis, the term "metal-poor" will be considered to indicate any low metalicity ( $[Fe/H] < -1.0$ ) object, in our Milky Way; to include all of the metal-poor stars' categories by one term.

Metal-poor stars are significant for constraining and explaining the creation history of our Milky Way, in addition to the physics of the high redshift universe (e.g., initial mass function). The general strategy is to collect such knowledge through the study of the complete elemental abundances patterns of metal-poor stars; many of these stellar objects built from the primordial (zero-metal) gas clouds throughout the very early chemodynamical growth of our galaxy (e.g., Beers 和 Christlieb, 2005). Many Chemical abundance analyses of these metal-poor stars present valuable constraints on the appropriate nucleosynthesis rules and the chemodynamical growth of our early galaxy (Zhao 和 Magain, 1990, 1991; McWilliam 等, 1995; McWilliam, 1998; Cayrel 等, 2004; Barklem 和 Aspelund-Johansson, 2005; Cohen 等, 2008). Recently, notable

attempts have been performed to fully describe the metallicity distribution function (MDF) of the halo system, particularly at the very metal-poor end (e.g., the HK survey and the Hamburg/ESO). These surveys yielded an exciting development in known metal-poor stars. High-resolution spectroscopic investigations of these stars distinguished in the Hamburg/ESO survey have proved the presence of ultra and hyper metal-poor stars in the halo system (Christlieb 等, 2002; Frebel 等, 2005; Norris 等, 2007). All these discovered stars are carbon-rich stars; no entirely metal-free (compose of only hydrogen and helium) stars have been observed thus far. Their results could be employed to place crucial constraints on the IMF. For illustration, semi-analytic models of Galaxy formation show that the absence of zero-metal stars restrains the crucial metallicity should be  $Z_{cr} > 0$  for low-mass stars formation (Schneider 等, 2002; Salvadori 等, 2007).

The full detailed elemental abundance patterns analysis of metal-poor stars can provide more valuable information on the chemical history of the halo system; different processes synthesize various elements, in different masses and timescales. As an illustrative example,  $\alpha$ -elements (nuclei with atomic number integer multiples of four; O, Mg, Si, Ca, and sometimes Ti) built during explosions of massive stars ( $M_\star < 8 M_\odot$ ), just several million years, after their formation. In contrast, iron-peak elements (local peak in the region of iron; Cr, Mn, Fe, Co, and Ni) are synthesized either by Type Ia or Type II supernovae. Moreover, Type Ia supernova is the outcome of the thermonuclear explosion caused by mass transfer onto the surface of a white dwarf star by its companion star, in a binary system, or a consequence of a white dwarf–white dwarf (double-degenerate) collisions, and thus occur on a more protracted timescale, of the order of 0.1 to few Gyr (Matteucci 和 Recchi, 2001). A more extreme example is the Heavy elements (beyond the iron-peak) production. These elements are built by neutron captures; through the slow (s) furthermore rapid (r) processes. The vast majority of these metal-poor stars show high  $\alpha$ -enhancement (typically  $\alpha$ -to-iron ratio  $\sim +0.4$ , Wheeler 等, 1989; Nissen 等, 1994; Carretta 等, 2000).

Another different possible chemical patterns, observed in metal-poor stars, are the carbon-rich or carbon-enhanced metal-poor (CEMP; carbon-to-iron ratio  $> 1.0$  dex

Beers 和 Christlieb, 2005) stars. A number of previous observational studies have indicated that carbon is omnipresent in the early universe (Beers 和 Christlieb, 2005; Aoki 等, 2007; Hansen 等, 2016a; Placco 等, 2016; Cruz 等, 2018; Caffau 等, 2018). Hence, the discovery and analysis of carbon-enhanced metal-poor stars ( $[C/Fe] \geq 0.77$ <sup>7</sup> hereafter CEMP), suggest that this substantial enhancement could be closely linked to their formation. In addition to carbon enhancement, different abundance ratios of neutron-capture elements are often used to distinguish the unique nature of CEMP stars: CEMP-s ( $[C/Fe] \geq +0.7$ ,  $[Ba/Fe] > +1.0$ , and  $[Ba/Eu] > +0.5$ ), CEMP-r/s ( $[C/Fe] \geq +0.7$  and  $0.0 < [Ba/Eu] < +0.5$ ), CEMP-r ( $[C/Fe] \geq +0.7$  and  $[Eu/Fe] > +1.0$ ), and CEMP-no ( $[C/Fe] \geq +0.7$  and  $[Ba/Fe] < 0.0$ ).

The CEMP-s and CEMP-no subclasses represent the predominant populations of the CEMP stars (Beers 和 Christlieb, 2005; Aoki 等, 2007; Hansen 等, 2016a; Yoon 等, 2016). The chemical patterns associated with CEMP-s stars (high enhancement in carbon and s-process elements) can arise from an intrinsic (self-enrichment) or an extrinsic (mass transfer from now white dwarf companion) process. Nevertheless, the overabundance of s-process elements (e.g.,  $[Ba/Fe] > +1.0$ ) support the matter accretion from an asymptotic giant branch (AGB) companion. These s-process elements (e.g., Sr, Ba, and Ce) are believed to be synthesized in low- to intermediate-mass stars (1 to  $3 M_{\odot}$ ), with low neutron densities ( $n_n \approx 10^6 \text{ cm}^{-3} - 10^{10} \text{ cm}^{-3}$ ) and  $^{13}\text{C}(\alpha, n)^{16}\text{O}$  as the main source of neutrons, which are eventually transferred and mixed into the atmosphere of the long-lived companion (observed as a CEMP-s star, Lucatello 等, 2005; Starkenburg 等, 2014).

CEMP-r/s and CEMP-r are much less frequent when compared with other subclasses. The origin of their enhancement (in r-process elements) is still widely debated. In contrast to the s-process elements, a high neutron density ( $n_n > 10^{22} \text{ cm}^{-3}$ ) is the key to synthesize these unstable neutron-rich isotopes (e.g., Eu, Os, and Ir). In the past, there have been many astrophysical sites proposed for r-process production. Still a few can provide such high neutron density environment (see Thielemann 等, 2017, and references therein). Presently, the possible sites are confined to magnetorotation-

<sup>7</sup>Using Aoki 等 (2007), as the criterion for carbon enhancement.

ally jet-driven supernovae (SN), core-collapse SN, neutron stars mergers, and neutron star-black hole mergers (e.g., Frebel, 2018).

The CEMP-no stars, which are believed to be the direct descendants of objects formed shortly after the big bang (Pop III), (Ito 等, 2013; Placco 等, 2014a; Hansen 等, 2016b), dominate the lowest-metallicity regime (e.g., Christlieb 等 2002; Frebel 等 2005; Caffau 等 2011; Keller 等 2014; Starkenburg 等 2018) and reside in the main-sequence, subgiants, or red giant phase. Their evolutionary stages and chemical patterns (excess in carbon with low abundances or absence of neutron-capture elements) suggest that a binary companion or self-enrichment are unlikely the sources of their chemical patterns. Therefore, a distinct enrichment channel may have taken place (e.g., Starkenburg 等 2014; Hansen 等 2016c). A spinstar is one possible candidate; these rapidly rotating massive ultra metal-poor ( $[\text{Fe}/\text{H}] < -6.0$ ) stars can produce large amounts of carbon (Meynet 等, 2006; Hirschi, 2007; Frischknecht 等, 2012; Maeder 等, 2015). Another proposed scenario for the carbon enhancement is pollution from faint supernovae associated with Pop III stars, with mixing-and-fallback (Umeda 和 Nomoto, 2003; Tominaga 等, 2007; Heger 和 Woosley, 2010; Nomoto 等, 2013; Tominaga 等, 2014; Ezzeddine 等, 2019). This faint SN ejects less iron and thus increases the  $[\text{C}/\text{Fe}]$  ratio, as they do not have enough energy to eject all its material into its surroundings. Therefore, only the outer layers with the lightest elements are ejected while the inner part falls back onto the neutron star or black hole. At present, none of the above scenarios can explain the full chemical patterns that have been observed in CEMP-no stars. In general, the unique chemical patterns observed in the sub-classes of CEMP stars result from the differences in the astrophysical sites responsible for the nucleosynthesis products they now mixed in their atmospheres.

## 1.4 The structure of the Milky Way system

We live/exist inside the Milky Way (our Galaxy). Therefore, cosmologists have long attempted to place constraints models on its formation and evolution. However, the glimpse into the cosmos is regrettably somewhat restricted, and thus, creativity is required to figure out what our Galaxy might indeed look like and what it is composed of.

Because of its huge size, we would never be capable of viewing its whole shape neither. Nevertheless, many observations of other galaxies (e.g., Ribas 等, 2005, Andromeda galaxy,) might provide some clues to this vital puzzle. Many ancient civilizations investigated the night sky by the most primitive optical tools (the human eye), to have a similar view, we have to move to the countryside (no light pollution) at a dark night(no bright moonshine). The scene will be somewhat like that the vast majority of our galaxy's stars assembled in a broad, scattered stripe crossed the sky (Jones, 2015).

Going back in time, the famous womanizer and the chief of all Greeks' gods Zeus had procreated a son, Heracles. Zeus' wife, the goddess Hera, was loaded with anger and jealousy. Heracles was not immortal such as the rest of the Greeks' gods; Heracles' mother was a mortal woman. Therefore, the king Zeus resorted to some cunning to cure this flaw; breastfeeding him from Hera was supposed to help, the baby boy, Heracles to earn his immortality. Thus the king Zeus, secretly, used to place Heracles with Hera while she is sleeping. However, the newborn nursed so vigorously and woke Hera up. With anger as hell, Hera threw Heracles away from her breast, that Hera's milk was sprayed all the way up to the heavens, where it seems as the Milky Way (Tidwell 等, 2019). A beautiful small myth to include in this thesis, yet what is the Milky Way in reality?

Few years after the invention of the telescope (around 1600 AC), Galileo Galilei (Italian scientist and inventor) investigated the Milky Way with the recently invented telescope, thus holding all the credits of this pioneering idea (Bolt, 2010). In his examination, he found that the glittering band across the sky composed of countless numbers of faint stars. Three centuries later, William Herschel (English astronomer) examined the night sky and published the first map of the Milky Way. This map shows how our galaxy might look like from a far distance. Nowadays, we acknowledge that the vast majority of the Milky Way's stars gathered inside a flat plate that gives the original appearance of the Milky Way (Cunningham, 2018). Apart from this, what makes these stars order themselves in this unique way?

Many astronomers around 1900 did more and more investigations on the Milky Way's structure, using some stellar statistical techniques, which proved its difficulty

(Pannekoek, 1910; Espin, 1912; Bailey, 1922; Plaskett, 1936; Baker, 1939; Macrae, 1943; Bolton 和 Westfold, 1950; Xu 等, 2018; Chen 等, 2019). However, the situation changed at the time Henrietta Leavitt (American astronomer) made her significant discovery (period-luminosity relation, Leavitt, 1908; Leavitt 和 Pickering, 1912) and finally gave the right means for the progress. A few years later, Harlow Shapley (American astronomer) employed her period-luminosity relation to making the Cepheids' distance measurement, thus establishing the technique of measuring stellar structures' distances inside and outside the Milky Way, as long as Cepheids exist nearby (Shapley, 1927). Afterward, Jan Oort (Dutch astronomer) succeeded to explain and describe our galaxy's motions with geometry and several targeted observations (Oort, 1927). In his study, he found that the Milky Way's stars rotate around its center due to a gravitation force, caused by a heavily compressed mass at its center. Therefore, these stars organized in a disk and act similar to a fluid that revolves slower at the edge than its center. It has primarily been recognized that our galaxy has a complete spiral structure; all the disk's stellar objects (stars, gas, and dust) arranged in several spiral arms. The following years presented innumerable observational evidence that permanently established our galaxy's disk-like shape (Hayes 等, 2018). Moreover, Radio-astronomers detected the preliminary component of the spiral arms (hydrogen gas). As a result, the Milky Way is, now, widely acknowledged as an example of a spiral galaxy such as many other galaxies (e.g., Yew, 2017, Andromeda and NGC 6744).

To create an imaginary idea of our home galaxy, we can imagine it as a very dense griddlecake, with generous coats of jelly jam and cream cover the top and bottom, fulfilled by a centrally located scoop of ice-cream, before serving to Rufina (my beloved girlfriend) add a cherry on the tip of the ice-cream scoop. The jelly jam and cream express various stellar populations spread over our Galaxy's disk that add to the giddlecake's thickness. The ice-cream scoop represents our Galaxy's bulge; large, dense, and the most luminous part of our home galaxy. Many observations show that the spiral arms of the Milky Way, in the inner part, merge to form one bar-shaped structure. At the precise middle of the Milky Way's bulge, there is an overwhelming-massive black hole of  $4 \times 10^6 M_{\odot}$ ; the cherry (see Figure 1.9). This monster black hole swallows enormous

quantities of stellar objects (e.g., stars and gas).

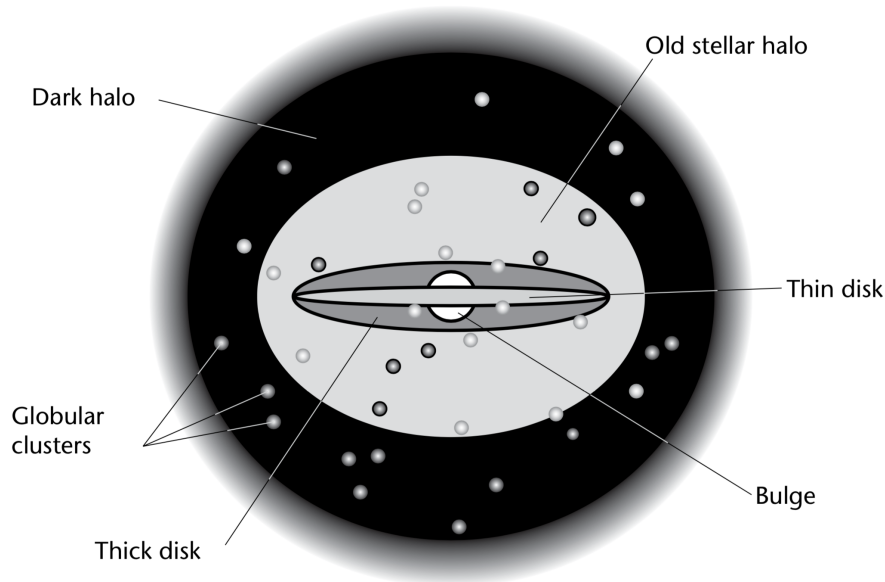


**图 1.9 Schematic view of the Milky Way with its different components indicated. Credits: Peter Palm**

The Milky Way's disk (thick disk, thin disk, and spiral arms) cover a wide area, with 100,000 light-years (ly) diameter, 1,000 ly thick, and 1,000 ly length (Haywood 等, 2019). Our home (the Solar System) is located far away (With respect to the Milky Way's center) in the disk thus the overwhelming-massive black hole creates no threat to our existence. As long as the Earth is orbiting our Sun with a velocity of 30 km/s, the Sun (with the whole Solar System) inside the spiral arm, which it is located at (the Orion-Cygnus Arm)<sup>8</sup>, is revolving around the Milky Way's center, with a velocity of 220 km/s and a somewhat an elliptic orbit. With its 4.6 billion years of age, the Sun has accordingly revolved approximately 20 times around the Milky Way's center that our existence (mammals; came to life somewhat 200 million years ago) does not yet represent to one Galactic revolution (Galactic year).

<sup>8</sup>Our exact position in the Milky Way is in the local spiral arm that is also referred to as the Orion-Cygnus Arm. The Sun and the Solar System lie at the inner edge of this arm. There are four larger and two smaller arms in total. The spiral arm laying in the direction of the center, seen from us, is the Sagittarius Arm, and the one behind us is called the Perseus Arm.

Our sky view is somehow restricted; we live inside the Orion-Cygnus arm. Thus we would be able to observe part of the remaining spiral arms as well as stars and gas from our spiral arm. However, our galaxy approximately divides the sky into two identical regions; the Solar System located in the central plane of the galactic disk. Therefore, when we observe upward or downward, we would be able to see outside the Milky Way. However, we will not see anything except the Milky Way band around us at the moment we look along the galactic disk's plane. This Milky Way band is the result of the spiral structure of the galactic disk; the view of Northern Hemisphere is directly towards the Perseus Arm, while the sight of Southern Hemisphere is directly towards the Sagittarius arm along the galactic center making it looks even more magnificent.

By having a more substantial look at our galaxy on the sky, we will immediately notice that it consist of small and large bright regions rather than being homogeneously lit up. Dark zones intermittent with the lighter ones, and the number of the observable stars can be inconstant. Interstellar dust and gas clouds cause these dark regions (Coalsack)<sup>9</sup>. The galactic disk contains enormous amounts of the stellar dust; particularly at the stellar site(s) where star formation took place. Dust assists star formation; cooling agent, allowing the stellar gas cloud to clump and compress into a star. Furthermore, the only way to observe the galactic center is only by employing radio astronomy.

Young stars densely populate the disk of the Milky Way; 95% of all Galactic stars. The galactic disk is made up by the so-called the thick disk, which surrounds a more substantial part, so-called thin disk (see Figure 1.9; demonstrating the distinguished disks). The disk parts are enclosed in a huge sphere; the stellar halo. The galactic halo has a significantly less star's density than the galactic disk and mainly contains some old stars, star clusters, and dwarf galaxies. This stellar system is uniquely crucial for galactic archaeology; it hosts the oldest and most metal-poor stars. All halo objects rotate around the galactic center, with large reasonably circular orbits. The galactic halo spreads around the Milky Way over several hundred thousands light-years.

Metal poor stars reside primarily in the halo system of the Milky Way, a complex

---

<sup>9</sup>Coalsack is a stellar region where stars light, on its way to us, is entirely blocked by very dense interstellar dust and gas clouds.

old component of the Galaxy that comprises at least two diffuse stellar populations, the inner- and the outer-halo, with different metallicities, kinematics and spatial density profiles (Carollo 等, 2007, 2010; Beers 等, 2012), several streams and overdensities (Grillmair, 2009), and a recently discovered large structure in the inner region, product of a past merger event (Helmi 等, 2018). It has been recognized that 15% – 20% of stars with  $[\text{Fe}/\text{H}] < -2.0$  in the halo system are CEMP and the fraction increases with declining metallicity becoming  $\sim 75\%$  at  $[\text{Fe}/\text{H}] < -4.0$  (see Carollo 等, 2014, and reference therein). There is also evidence for a significant contrast in the frequency of CEMP stars that are kinematically assigned to the inner- and outer-halo components (the inner halo is on-average non rotating, while the outer halo exhibits a significant retrograde signature). The outer halo exhibits a fraction of CEMP stars twice the inner halo in the metallicity interval  $-2.5 < [\text{Fe}/\text{H}] - 2.0$  (Carollo 等, 2012). Such increase in frequency of CEMP stars can be explained as a population driven effect, due to the fact that the outer halo is the dominant component at large distance from the galactic plane and at metallicities,  $[\text{Fe}/\text{H}] < -2.0$ . The chemical differences between the two stellar halo populations were established also in terms of CEMP sub-classes by Carollo 等 (2014). It was shown that the relative numbers of CEMP-no stars compared to CEMP-s varies between the inner- and outer-halo and the frequency of the CEMP-no stars is higher in the outer halo, while the frequency of the CEMP-s stars is higher in the inner halo. The analyses of kinematics and dynamics of our sample stars will establish their inner/outer halo membership and on their origin. The chemical abundance analysis of metal-poor stars and searching of CEMP and NEMP stars provides important constraints on the chemistry evolution of the Galaxy, initial mass function (IMF; Hirano 等 2014) and the models of mass-transfer and evolution of components in binary systems.

## 第 2 章 Target Selection and Observations

### 2.1 Target Selection From LAMOST survey

Our sample stars were chosen from the Large Sky Area Multi-Object Fiber Spectroscopic Telescope (LAMOST) survey (Zhao 等, 2006, 2012; Cui 等, 2012). This national scientific research tools (reflecting Schmidt telescope) served, with its 4000 fibers, the National Astronomical Observatories of China (NAOC). With a view field of 20 deg in the sky, LAMOST obtained more than five million spectra (with a wavelength range of 3690-9100 Å and resolving power of  $R \sim 1800$ ) of various stellar objects (stars, galaxies, quasars, etc.). With SNR larger than 10 for 3,374,398 stellar objects in g- and i-bands, the LAMOST's third data release (DR3<sup>1</sup>) has been published online. The public online data products include many fundamental stellar quantities (e.g., stellar parameters, radial velocities). We ran two separate approaches to estimate the metallicity ([Fe/H]) of each stellar object. The following paragraphs can highlight these two methods:

#### The first approach:

In this approach, we used the stellar synthesis code SPECTRUM<sup>2</sup> (Gray 和 Corbally, 1994) and an interpolated stellar atmosphere models adopted from the 1D ATLAS NEWODF grid of Castelli 和 Kurucz (2003)<sup>3</sup>, to generate grid templates. We have used this grid templates to compare it with LAMOST's spectra to estimate their [Fe/H]. This approach directly depends upon the line indices; 27 lines were have been selected in accordance with SEGUE stellar atmospheric parameter pipeline and Lick indices<sup>4</sup>.

#### The second approach:

In this approach, we have directly correlated the observed flux in a LAMOST's spectrum with a synthetic spectrum. These synthetic spectra have a wavelength

---

<sup>1</sup><http://dr3.lamost.org/>

<sup>2</sup><http://www.appstate.edu/~grayro/spectrum/spectrum.html>

<sup>3</sup><http://kurucz.harvard.edu>

<sup>4</sup><http://astro.wsu.edu/worthey/html/index.table.html>

range of 4360-5500Å; which contain enough numerable chemical features sensitive to the altar of the atmospheric parameters (effective temperature, surface gravity, and metallicity), and prevent any potential CH contamination neighboring the G-band (4300Å).

It is worth mentioning that the initial atmospheric parameters that we have used to generate the synthetic spectra have been selected based on photometrical estimations. We cross match our sample with two catalogs from the Virtual Observatory: The fourth US Naval Observatory CCD Astrograph Catalog (UCAC4, [Zacharias 等 2013](#) ) and the Two Micron All Sky Survey (2MASS, [Skrutskie 等 2006](#)) and then employ [Ramírez 和 Meléndez \(2005\)](#) temperature calibration.

Based on the two approaches, we indicate a star with  $[\text{Fe}/\text{H}] < -2.0$  dex and effective temperature in between 4000 and 7000 K as a potential VMP star candidate. This effective temperature range eliminates low-luminosity, late-type, and blueward MS-turnoff stars. Moreover, WD stars, with reasonably low temperature, and candidate stars with relatively low SNR were discarded. Thirteen stars were selected to obtain high-resolution observations, which represent the data for the following subsection.

## 2.2 High-resolution Observations with Lick/APF

The Automated Planet Finder (APF) is Lick Observatory's latest telescope, which was engaged entirely on the Mt. Hamilton mountain in August 2013. APF telescope with its capability to detect and observe planets that might sustain life in an extrasolar system considered as the first of its kind. This fully robotic optical telescope, with its 2.4-meter mirror and the high-resolution spectrograph (Levy spectrograph), explores nearby stars every night. The supreme aim of APF's research is to find as much as possible of Earth-like planets, which might hold life. Levy spectrograph utilizes a large dispersing prism to deliver the stellar object's light to concentrate on the APF's CCD, to examine and store the spectrum of this object. With a slit width of 2 arc-seconds, an echelle spectrum with resolutions of 100,000 can be efficiently obtained over the whole Iodine region; it may reach 150,000 in some circumstances, and a wavelength range from 3740Å-9700Å. For more information about this telescope and its instruments, we

refer the reader to Radovan 等 (2014). We obtain high-resolution spectra ( $R = 110,000$ ), covering the wavelength range of (3740-9700 Å ), for a sample of 13 stars. In addition, we observed HD2796 as a standard.



## 第3章 Data Reductions

In this chapter, we will discuss the Astronomical codes/programs that we employed in our study. After obtaining these high-resolution spectroscopy observations, for thirteen stars, we had to reduce these observational data and turn them into normalized 1D spectra. We achieved our goal by using the Image Reduction and Analysis Facility ([Tody, 1986, 1993](#), hereafter IRAF) and its packages.

### 3.1 Data reductions with IRAF

This section aims to obtain a wavelength-calibrated spectrum from the two dimensional CCD image; calibrations of CCD data, extraction of the spectrum, wavelength calibration, continuum normalization, and combining spectra of individual echelle orders. Figure 3.1 shows a chart-flow for the echelle reduction procedure.

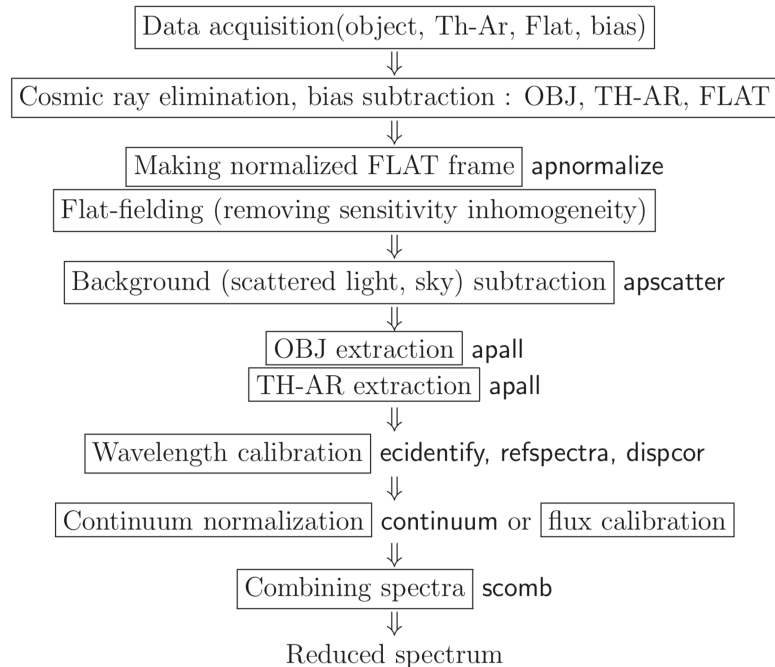


图 3.1 Chart-flow for the echelle reduction procedure.

### **Dark currents and Bias corrections:**

The first step in our data reduction was the bias<sup>1</sup> and dark current<sup>2</sup> corrections.

To improve the data quality we combined several Bias files by using the average Bias value of every pixel; in case of cosmic-ray noise, some pixels will show high Bias values, which makes the statistical median is the right choice rather than average.

### **Extraction of spectra:**

The second step in our data reduction was extraction of spectra. It is useful to generate a reference frame for the consequence steps using the apall task. The second step in our data reduction was extraction of spectra. It is useful to generate a reference frame for the consequence steps using the apall task, which examines the individual echelle orders for spectra and then estimate the aperture's position and size. Moreover, this step can be interactively corrected (see top right panel of Figure 3.2)

### **Flat fielding:**

The third step in our data reduction was the flat fielding. In this step, we did a pixel-to-pixel correction to remove any sensitivity inhomogeneity of the CDD. At the time that a wavelength coverage of the spectrograph is so broad (as the case in the APF data), the flat lamp intensity/strength might not be adequately high in some ranges. Therefore, we alter the exposure time of the flat data, either the filter setting. The APF data has narrow and wide flat data for each CCD. We normalized all the flat frames and then divided the science object frame by the new combined flat frame.

### **Background subtraction:**

The third step in our data reduction was the background subtraction. The IRAF apscatter task did this step. This step can be interactively corrected (see top left panel of Figure 3.2). One might alter the fitting function either its order. Once the fitting seems satisfactory, we proceed with the remaining steps.

### **Extraction of one dimensional spectra:**

---

<sup>1</sup>The Bias can be estimated by obtaining some CCD values with no exposure time (zero seconds);

<sup>2</sup>Dark currents determined without opening the CCD shutter.

The fourth step in our data reduction was extraction of one dimensional spectra. We had used the task apall one more time to extract the spectrum from the object frame, which we previously flat-fielded and background-subtracted.

#### **Wavelength calibration:**

The fifth step in our data reduction was the wavelength calibration. In this step, we linked comparison data, previously mentioned, to produce wavelength scale using refspectra task. Figure 3.2, lower right panel shows the result of this step.

#### **Continuum normalization:**

The sixth step in our data reduction was the continuum normalization. In this step, we obtained normalized spectra by fitting curves. The efficiency of the APF Echelle spectra is somewhat near the CCD center. Moreover, the edges show deficiency at spectra ends/edges. We altered the fitting function and its order until the fitting is pleasing. The exercise wa done for all apertures/orders. Figure 3.2, lower left panel shows the result of this step.

#### **Doppler effect:**

The final step, in our data reduction, was doppler correction. In this step, we prepare our normalized spectra for the chemical abundances' investigation. We shifted our normalized spectra to its rest frame, using FXCOR task. Finally, we used wspectxt task to write the RV corrected spectra into an ASCII file (two columns; wavelength and normalized flux).

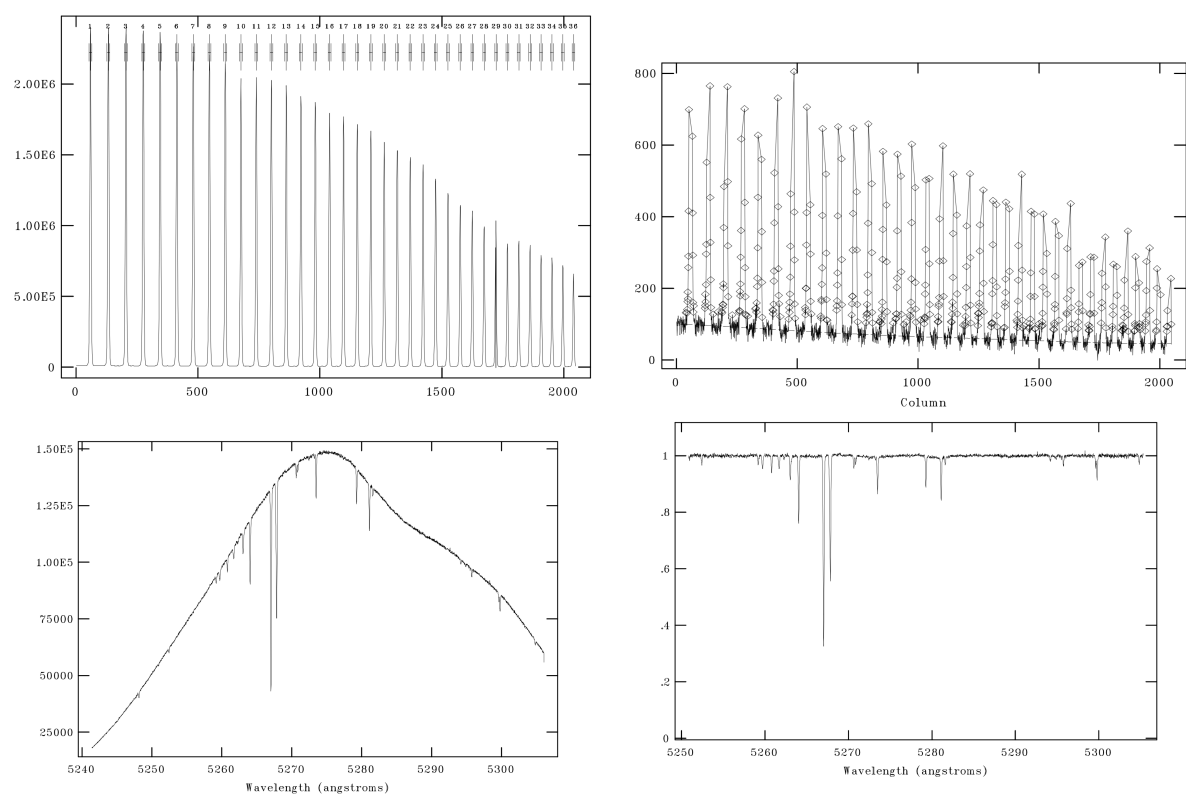


图 3.2 An illustrative example of our data reduction procedures for the major steps.

## 第 4 章 Stellar Parameters

Despite the fact that iron abundances derived from both excitation levels (Fe I and Fe II) are affected by uncertainties in the model atmospheres temperature and NLTE effects (see Mashonkina 等, 2017, and reference therein), many researches still rely on this method (the so-called traditional spectroscopic method) to derive their stellar atmospheric parameters. Our adopted stellar parameters have been determined through this standard spectroscopic method. Additionally, we were able to determine effective temperatures from photometry and surface gravities from parallax/distances.

### 4.1 Effective temperature

The effective temperatures ( $T_{\text{eff}}$ ) were estimated by minimizing the trend between Fe I lines abundances and excitation potential ( $\chi$ ).

To estimate  $T_{\text{eff}}$  from the available colors (B, V, J, H, and K), we cross match our sample with two catalogs from the Virtual Observatory: The fourth US Naval Observatory CCD Astrograph Catalog (UCAC4, Zacharias 等 2013 ) and Two Micron All Sky Survey (2MASS, Skrutskie 等 2006) and then employ Ramírez 和 Meléndez (2005) temperature calibration. These  $T_{\text{eff}}$  (determined from photometric and spectroscopic methods) together with  $T_{\text{eff}}$  taken from Gaia DR2 (Gaia Collaboration 等, 2018) are in good agreement with each other ( $\pm 150$  K).

### 4.2 Surface gravity and microturbulence

We determined the surface gravity ( $\log g$ ) by forcing Fe I abundances to agree with Fe II abundances. In addition, we crossed match our sample with Gaia DR2 distances catalogue (Bailer-Jones 等, 2018), to estimate the distance modulus from the available parallax of Gaia Collaboration 等 (2018) (see Eq. 4.1 and Eq. 4.2).

$$\log \frac{g}{g_{\odot}} = \log \frac{M}{M_{\odot}} + 4 \log \frac{T_{\text{eff}}}{T_{\text{eff}}} + 0.4(M_{\text{bol}} - M_{\text{bol}_{\odot}}) \quad (4.1)$$

$$M_{bol} = V + BC + 5 \log \varpi + 5 \quad (4.2)$$

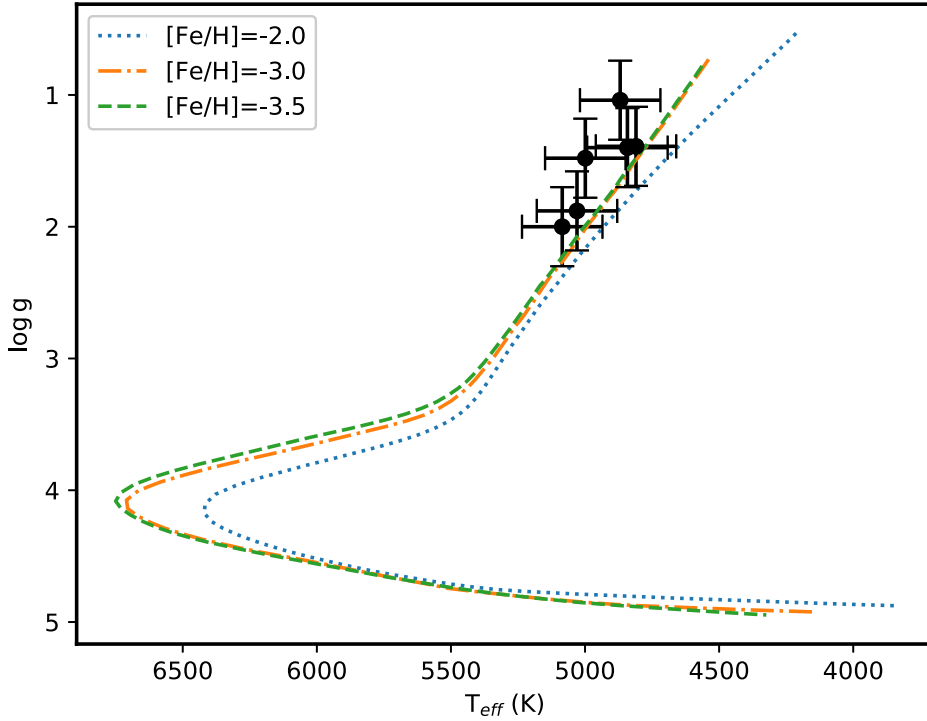


**图 4.1 Our sample shown in an H-R-Diagram, based on the  $T_{\text{eff}}$  and  $\log g$  determined from the LIKC/APF spectra. Yale-Yonsei 12 isochrones with  $[\alpha/\text{Fe}] = +0.4$  and  $[\text{Fe}/\text{H}] = -2.5$ ,  $-3.0$ , and  $-3.5$  from [Demarque 等 \(2004\)](#) overplotted as reference.**

where,  $M$  is the stellar mass,  $M_{bol}$  is the absolute bolometric magnitude,  $V$  is the visual magnitude,  $BC$  is the bolometric correction (see [Alonso 等, 1999](#), Eq. 18), and  $\pi$  is the parallax.

The microturbulence velocities ( $\xi$ ) were determined by removing any trend between Fe I lines abundances with the EWs of those lines.

The  $T_{\text{eff}}$  determined from the photometric and spectroscopic methods show systematically different results. [Frebel 等 \(2013\)](#) have presented an explicit method to adjust the spectroscopic  $T_{\text{eff}}$ . This scheme increases the  $T_{\text{eff}}$  determined for cool red-giants up-to several hundred degrees, on the other hand the  $T_{\text{eff}}$  determined for main-sequence stars are mostly unaffected. Motivated by [Frebel 等 \(2013\)](#) results, the atmospheric

stellar parameters ( $T_{\text{eff}}$ ,  $\log g$  and  $\xi$ ) determined for our sample stars from the spectroscopic method were considered as initial parameters, and then corrected following the same scheme presented in [Frebel 等 \(2013\)](#). It's worthy to note that our parameters were not determined independently. Thus, this procedure was iterated to consistency.

The corrected spectroscopic surface gravities (in cgs units) versus the corrected spectroscopic  $T_{\text{eff}}$  of our programme stars, with 12 Yale-Yonsei isochrones as a reference ([Demarque 等, 2004](#)) are shown in Figure 4.1. The error bars shown in Figure 4.1 represent  $T_{\text{eff}}$  and  $\log g$  one-sigma errors ( $\pm 150$  K and  $\pm 0.3$  cgs, respectively).

### 4.3 Abundance Analysis

We used only non-blended lines with reliable continuum normalization to measure the chemical abundances using EWs analysis. However, for the molecular bands and blended lines, spectral synthesis was used. In other words, our chemical abundances were done by a mixture of spectrum synthesis and equivalent width analysis. Moreover, we considered the deviations from LTE for Li I, Na I and Mg I lines. We adopted the solar  $\log \epsilon_{\odot}(X)$  from [Asplund 等 \(2009\)](#) to obtain our final chemical abundances and [X/Fe] ratios.

### 4.4 LTE and NLTE calculations

We used stellar atmosphere models from 1D ATLAS NEWODF grid of [Castelli 和 Kurucz \(2003\)](#). Our LTE abundances were performed using an updated version of the stellar code MOOG ([Sneden, 1973](#)). In this update, a continuous scattering will be treated as a source function, in other-words the absorption and scattering will be summed rather than treated as true absorption ([Sobeck 等, 2011](#)).

The departures from LTE in the stellar atmospheres were considered for three chemical elements, Li, Na, and Mg. The adopted Na I and Mg I-II model atoms are described in [Alexeeva 等 \(2014\)](#) and [Alexeeva 等 \(2018\)](#), respectively. To solve the radiative transfer and statistical equilibrium equations, we used the code DETAII ([Butler 和 Giddings, 1985](#)) based on the accelerated  $\Lambda$ -iteration method ([Rybicki 和 Hummer, 1991](#)). The obtained departure coefficients,  $b_i = n_{\text{NLTE}}/n_{\text{LTE}}$ , were then used

by the codes `BINMAG3` ([Kochukhov, 2010](#)) and `SYNTHEV-NLTE` ([Ryabchikova 等, 2016](#)) to calculate the synthetic NLTE line profiles. Here,  $n_{\text{NLTE}}$  and  $n_{\text{LTE}}$  are the statistical equilibrium and thermal (Saha-Boltzmann) number densities, respectively.

We constructed the Li I model atom in the same manner as it was described in [Lind 等 \(2009\)](#). The main difference between our model atom and the model atom of [Lind 等 \(2009\)](#) is the collision excitation recipe. We adopted the electron collision data from [Osorio 等 \(2011\)](#), while [Lind 等 \(2009\)](#) used cross-sections for collisional excitation by electrons from [Park \(1971\)](#). We tested our model with Li-enhanced stars and have found a good agreement with [Lind 等 \(2009\)](#).

## 第 5 章 DISCOVERY OF FIVE CARBON-ENHANCED METAL-POOR STARS FROM LAMOST

### 5.1 Results and discussion

#### 5.1.1 Chemical abundance comparison with literature data

We provided stellar parameters and detailed chemical abundances for five metal-poor red giant stars, reported for the first time using high resolution spectroscopy. These stars exhibit similar chemical abundance patterns to, reported in other, very and extremely metal-poor stars (e.g., [François 等, 2007](#); [Yong 等, 2013](#)).

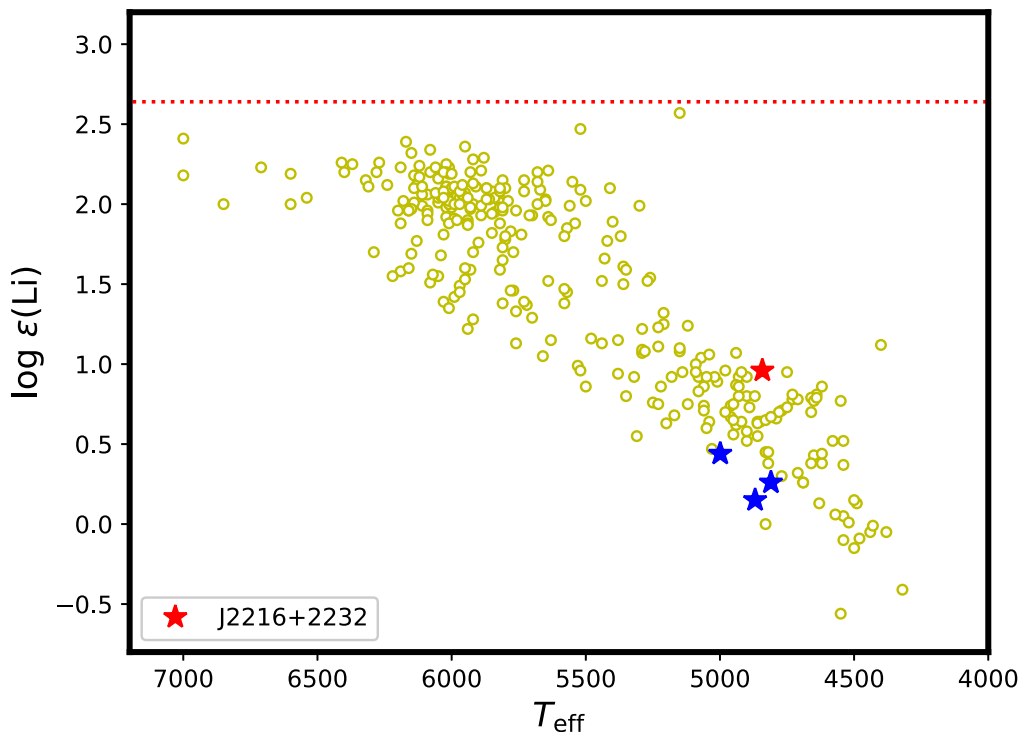


**图 5.1**  $\log \epsilon$  lithium abundances as a function of effective temperature. Red filled star refers to J2216+2232, blue filled stars refer to the determined upper limits, and small open circles refer to the full sample of [Roederer 等 \(2014a\)](#). The dotted line shows the predicted primordial lithium abundance,  $\log \epsilon_{Li} = 2.64$  ([Spergel 等, 2007](#)).

Lithium is considered as a key diagnostic, to test and constrain our understanding of the early Galaxy, of stellar interiors and evolution. Figure 5.1 illustrates the evolution of

lithium as a function of using the halo star sample from Roederer 等 (2014a, including upper limits). The dotted line refers to the primordial lithium abundance predicted by the Standard Big Bang Nucleosynthesis (Spergel 等, 2007). Among the program stars, we could only detect Li in J2216+2232 (shown as red filled star) with  $A(\text{Li}) = 0.95$ . For completeness the upper limits for the rest of our sample stars have been provided (blue filled stars). This is not unexpected, as our sample stars are red-giants, whose Li content in the outer layers have been diluted by the canonical extra mixing and the first dredge-up (FDU) process.

Our sample stars exhibit relatively high [C/Fe] ratios, as shown in Figure 5.2 (left panel), which represents [C/Fe] ratio as a function of luminosity. We adopted a classification of Aoki 等 (2007), who suggest a scheme that takes into consideration the nucleosynthesis and mixing effects in giants. We define the stars that satisfy the following criteria as CEMP stars:  $[\text{C}/\text{Fe}] \geq 0.7$  for stars with  $\log(L/L_\odot) \leq 2.3$  and  $[\text{C}/\text{Fe}] \geq 3.0 - \log(L/L_\odot)$  for stars with  $\log(L/L_\odot) > 2.3$ . The luminosities of our stars were calculated based on the prescription of Aoki 等 (2007), assuming stellar mass of  $0.8 M_\odot$ , following Aoki 等 (2005) and Ryan 等 (2005). For completeness, and due to the fact that our sample stars are giants, we use the carbon evolutionary correction described in Placco 等 (2014b) to assess whether our sample stars could indeed be classified as CEMP, this method suggests that carbon levels decrease as stars evolve into the giant branch phase, due to some level of internal mixing. As a result, the correction increases the C abundances up to several dex, which support our claims that these stars are CEMP stars.

With the Aoki 等 (2007) definition of CEMP stars and the carbon evolutionary correction described in Placco 等 (2014b) in mind, Figure 5.2 (left panel) shows that our program stars are located above the limit. Thus, we point J1054+0528, J1529+0804, J1645+4357, J2114-0616, and J2216+2232 as CEMP stars.

For most of our program stars CN bands are not measurable, we could only measure N abundance for J2114-0616, which exhibits high nitrogen abundance with  $[\text{N}/\text{Fe}] = 1.88$ ,  $[\text{N}/\text{C}] > 0.51$ , and  $[(\text{C}+\text{N})/\text{Fe}] = 1.53$ . Figure 5.2 (right panel) shows [C/Fe] as a function

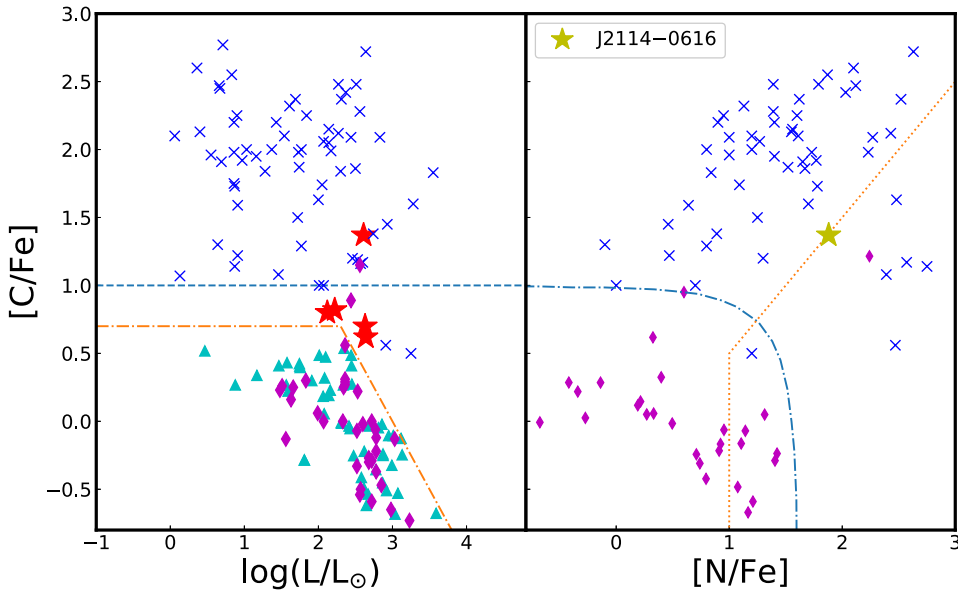


**图 5.2** 左面板: [C/Fe] versus luminosity for our sample stars. The dash-dotted line indicates the dividing line between carbon-enhanced and carbon-normal stars as defined in Aoki 等 (2007). The dashed line corresponds to [C/Fe] = 1.0. 右面板: [C/Fe] vs. [N/Fe]. The two criteria for NEMP stars suggested by Pols 等 (2012) are respectively shown in dotted ( $[N/Fe] \geq 1.0$  and  $[N/C] \geq 0.5$ ) and dash-dotted lines ( $[(C+N)/Fe] > 0.9$ ). The filled red stars refer our sample stars. Non-carbon-enhanced objects studied by previous works (Gratton 等, 2000; Cayrel 等, 2004; Honda 等, 2004; Aoki 等, 2005) are shown by triangles up. Metal-poor stars from Spite 等 (2005) (filled diamonds), and CEMP stars from Aoki 等 (2007) (crosses) are also plotted for comparison. The candidate to CNEMP objects J2114-0616 is marked.

of [N/Fe], with the dotted and dash-dotted lines referring to Pols 等 (2012) NEMP stars criteria. We classify J2114-0616 as a potential nitrogen-enhanced metal-poor (NEMP) star. Since J2114-0616 satisfies both criteria (star with  $[C/Fe] \geq 1.0$  and  $[N/C] \geq 0.5$ ), it can be designated as a carbon and nitrogen-enhanced metal-poor (CNEMP) star.

Moreover, we investigated [Eu/Fe] as a function of [Ba/Fe] to study s-process and r-process enrichment, under the pretext that J2114-0616 shows  $0.0 < [Ba/Eu] < +0.5$ , and  $[Ba/Fe] > 0.5$  (see figure 5.3), we regard it as a CEMP-r/s star. In addition to the enhancements in both slow (s-) and rapid (r-) process species, J2114-0616 shows high

[N/Fe] ratio, along with its high [C/Fe], which suggest that its peculiar chemical pattern may come from mass transfer from an AGB companion, before it tuned to a white dwarf.

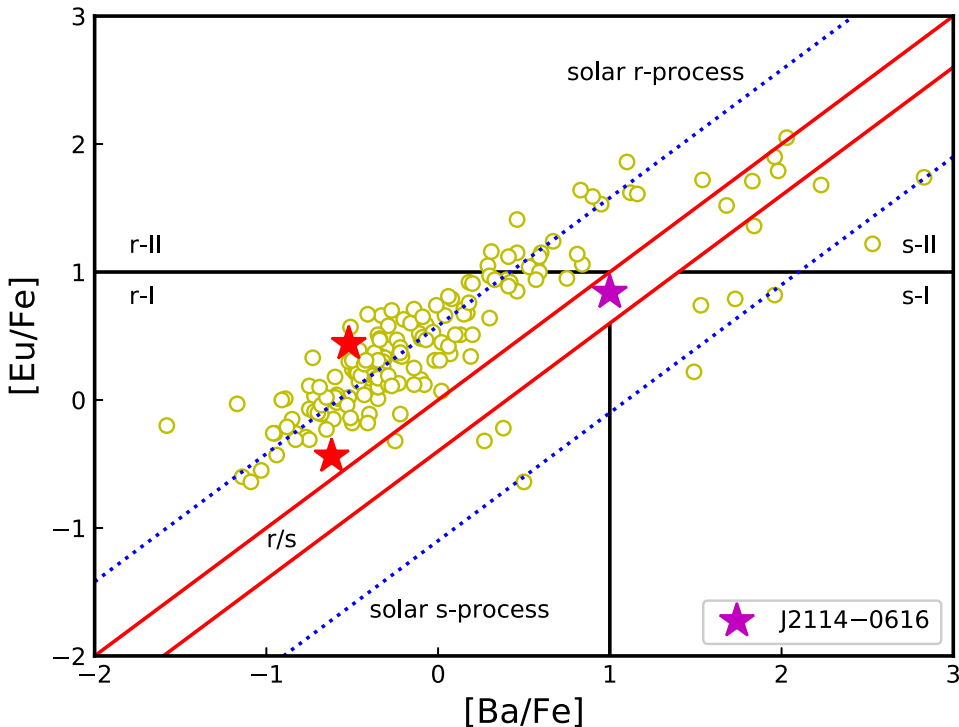
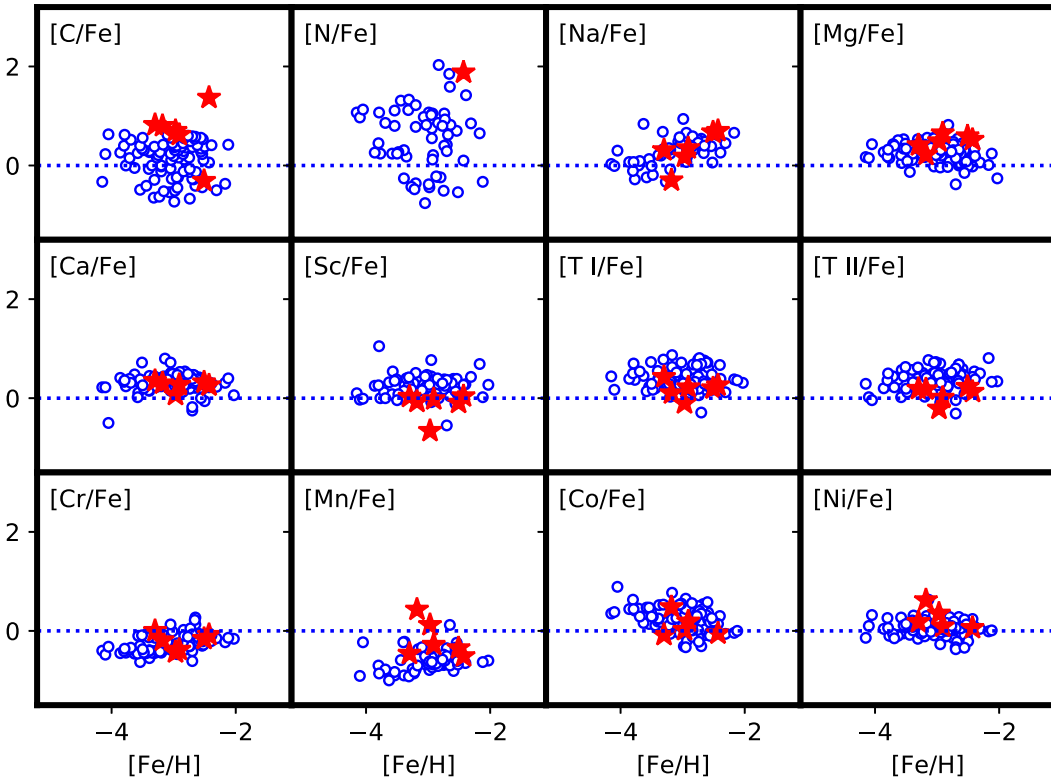


图 5.3 [Eu/Fe] as a function of [Ba/Fe], the open circles are data take from saga database ([Suda 等, 2008](#)) and the magenta star refer to the position of [J2114-0616](#).

Light element distributions in CEMP stars are quite similar to those in non-carbon-enhanced stars (C-normal). The abundance ratios [X/Fe] as a function of [Fe/H] of our sample stars (red filled stars) are presented in Figure 5.4, for the elements from C through Zn, compared with literature data adopted from [Yong 等 \(2013\)](#) (blue open circles). In general, the abundance ratios seen in our sample show good agreement with the abundance ratio trends defined by the literature sample. On the other hand, J1529+0804, which shows enhancement in manganese with  $[\text{Mn}/\text{Fe}] = 0.43$ , is not a good example of this agreement, this enhancement may also be true for J1645+4357 ( $[\text{Mn}/\text{Fe}] = 0.12$ ), keeping in mind that at low metallicities, the NLTE behavior may



**图 5.4 Comparison between the light-element abundances in our sample stars (red filled star) and the literature C-normal metal-poor stars from [Yong 等 \(2013\)](#) (blue open circles).**

systematically increase the manganese abundance up to 0.7 dex (which we will explore in future work) (e.g., [Bergemann 和 Gehren, 2008](#)).

### 5.1.2 Nucleosynthetic signatures of s- and r-process

Only elements lighter than zinc can be produced via nuclear-fusions, on the other hand, heavier elements can be synthesized by either the rapid neutron capture process, r-process, and the slow neutron capture process, s-process (e.g., [Meyer 1994; Arnould 等 2007](#) and references therein). Metal-poor stars provide unique opportunities to attain nucleosynthetic signatures, thus better understanding of the chemical evolution of these elements and the nucleosynthesis occurred in the early Universe.

As mentioned previously, we were able to determine abundances for up to 10 heavy elements, including the light trans-iron elements ( $38 \leq Z \leq 46$ ) and the second r-process peak elements. The abundances of selected neutron-capture elements for our sample stars (red filled stars), as a function of the metallicity, overlaid with literature

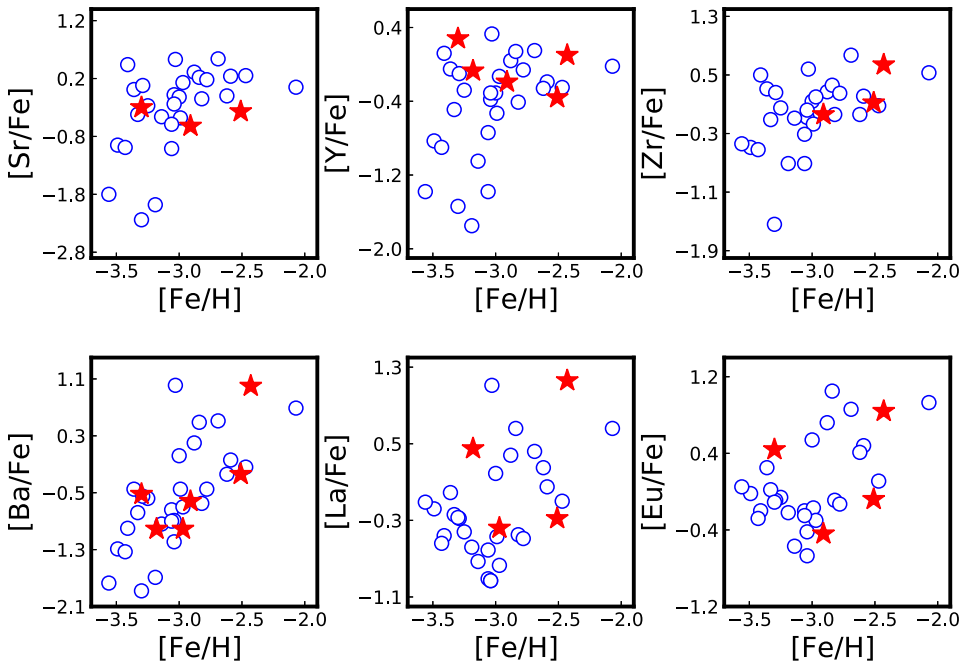


**图 5.5 Selected neutron-capture elements abundances in our sample stars (red filled stars), as a function of metallicity, compared to literature data adopted from François 等 (2007) (blue open circles).**

data adopted from François 等 (2007) (blue open circles) are shown in Figure 5.5. No significant discrepancies are found between the selected neutron-capture elements abundances of our sample stars and the literature data.

Figure 5.6 shows the neutron-capture element abundances for HD2796 and three sample stars, compared with the Solar System s-process (normalized to Ba - solid line) and r-process (normalized to Eu - dotted line) components. The s- and r- fractions were taken from Burris 等 (2000). Abundances for the first-peak s-process elements (Sr, Y, and Zr) are well described by the Solar s-process for HD2796 and J2216+2232, while for J1054+0528 and J2114-0616 they are roughly consistent with the r-process component. At the same time, the noticeable deviations from the light elements might interestingly be related to the effects of core-collapse supernovae. In contrast, for the second-peak s-process elements, there is an excellent agreement between measurements and the Solar s-process component for J2114-0616 which, combined with its enhancements in carbon and nitrogen, supports the hypothesis of mass transfer in a

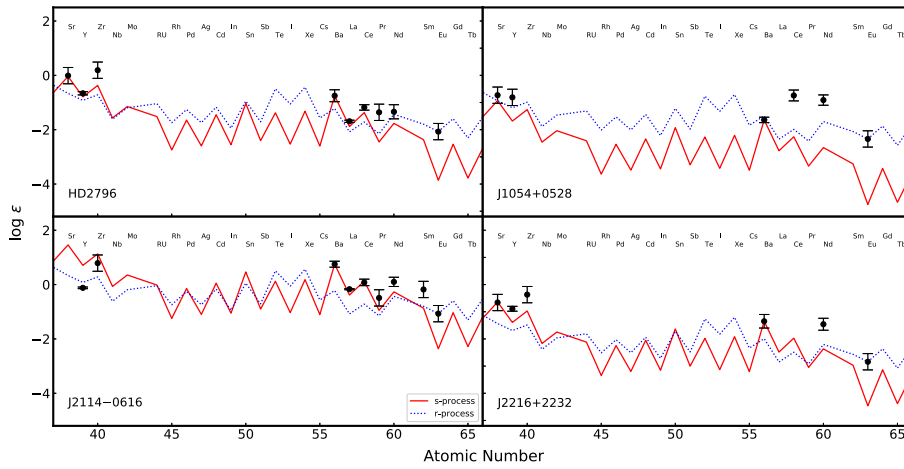


**图 5.6** Abundance patterns for the neutron-capture elements in our sample. The solid line represents the Solar-system s-process abundance pattern from Burris 等 (2000), scaled to match the observed abundance of Ba in each star. The dotted line represents the Solar-system r-process abundance pattern from Burris 等 (2000), scaled to match the observed abundance of Eu in each star. Note that we only include these stars with measured Ba and Eu.

binary system from an AGB companion. For J1054+0528, it appears that all the neutron-capture element abundances are a result of an r-process event, with no contributions from the s-process component.

We could only detect weak Ba II lines in the spectrum of J1645+4357, which results in a relatively low Ba abundance while no other s-process elements can be detected. Such chemical patterns (high carbon, low barium, and absence of other s-process elements) suggests that J1645+4357 was formed out of pristine gas. The common definition of strongly r-process-enhanced star is  $[{\rm Eu}/{\rm Fe}] > +1.0$  and  $[{\rm Ba}/{\rm Eu}] < 0$  and moderately r-process-enhanced star is (r-II stars)  $+0.3 \geq [{{\rm Eu}/{\rm Fe}}] \leq +1.0$  and  $[{\rm Ba}/{\rm Eu}] < 0$  (e.g., Frebel, 2018), adopting this criterion we suggest that J1054+0528 ( $[{{\rm Eu}/{\rm Fe}}]=0.44$ ) is a new member of the moderately r-process-enhanced stars (r-I stars). On the other hand, J2114-0616 exhibits different chemical abundance patterns, enhancement of s-process species along with relatively high magnesium abundance suggesting that  $^{22}{\rm Ne}(\alpha, n)^{25}{\rm Mg}$  may have operate as a main neutron source in J2114-0616 (Masseron 等, 2010). Moreover, it turns out that the neutron density linked to this reaction favors the

production of cerium (81% synthesized by s-process) and europium (97% synthesized by r-process), suggesting that these elements can't be explained by s-process only, and additional r-process is required to describe this behavior (Gallino 等, 1998; Goriely 和 Mowlavi, 2000).

### 5.1.3 Kinematics and dynamics

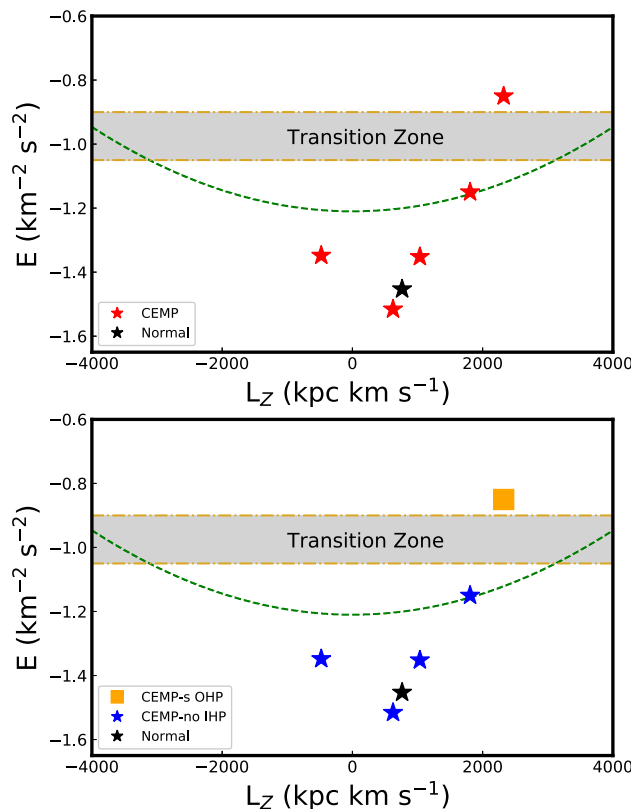


**图 5.7 Total energy vs. angular momentum in the z direction for the stars in our sample.** Top panel: C-normal stars are represented by black stars, while CEMP stars are denoted by red stars. Bottom panel: the same sample of stars, with blue filled star symbols indicating CEMP-no members of the inner halo, the orange filled square symbol represents the CEMP-no and CEMP-s members of the outer halo. The green dashed curve denotes the locus of the points that possess constant apo-Galactic radius,  $r_{apo} = 15 \text{ kpc}$ , while the golden dot-dashed horizontal lines shows the values of the energies delimiting the transition zone.

The full space motion is derived by combining the observables obtained by Gaia DR2, positions and proper motions ( $\alpha$ ,  $\delta$ ,  $\mu_\alpha$ ,  $\mu_\delta$ ). We utilize the software TOPCAT to cross match our sample with two catalogs from the Virtual Observatory: Gaia DR2 (Gaia Collaboration 等, 2018, for proper motions) and Gaia DR2 distances (Bailer-Jones 等, 2018, for distances). Radial velocities are obtained through cross-correlation with synthetic spectra after the heliocentric corrections to the observed spectra are applied. The velocities calculated in the Local Standard of Rest (LSR) are referred to as  $(U, V, W)$  which are corrected for the motion of the Sun by adopting the values  $(U, V, W) = (-9, 12, 7)$  km s<sup>-1</sup> (Mihalas 和 Binney, 1981). The velocity component  $U$  is taken to be positive in the direction towards the Galactic anti-centre, the  $V$  component is positive in the direction towards Galactic rotation, and the  $W$  component is positive toward the north Galactic pole. We also compute the rotational velocity component about the Galactic centre in a cylindrical frame, denoted as  $V_\phi$ , and is calculated assuming that the LSR is on a circular orbit with a value of 220 km s<sup>-1</sup> (Kerr 和 Lynden-Bell, 1986). The orbital parameters are derived by adopting a Stäckel type gravitational potential (which consists of a flattened, oblate disk, and a nearly spherical massive dark-matter halo; a complete description is given by Chiba 和 Beers (2000, Appendix A) and integrating their orbital paths based on the starting point obtained from the observations.

In addition, we evaluate the integrals of motion for any given orbit, deriving the energy,  $E$ , and the angular momentum in the vertical direction,  $L_Z = R \times V_\phi$ . Note that  $R$  represents the distance from the Galactic center projected onto the disk plane. Typical errors on the orbital parameters (at  $Z_{\text{max}} < 50$  kpc; Carollo 等, 2010) are:  $\sigma_{rperi} \sim 1$  kpc,  $\sigma_{rapo} \sim 2$  kpc,  $\bar{C}_{ecc} \sim 0.1$ ,  $\bar{C}_{Zmax} \sim 1$  kpc.

Carollo 等 (2014) established a method for assigning the membership to the inner- and outer-halo stellar populations based on the integrals of motion (total energy and vertical angular momentum) of a large sample of SDSS/SEGUE DR7 calibration stars. Inner halo stars are mostly highly bound to the Galaxy (lower energy values,  $E < -1.1$  km<sup>2</sup> s<sup>-2</sup>) and possess orbits with apo-galactic distance  $r_{apo} < 15$  kpc, while outer halo stars are less bound to the Galaxy (higher energy values,  $E > -0.9$  km<sup>2</sup> s<sup>-2</sup>) and possess orbits with  $r_{apo} > 15$  kpc. Stars with  $r_{apo} > 15$  kpc and  $E < -1.1$  km<sup>2</sup> s<sup>-2</sup> can be

also considered pure inner halo stars. In general, stars in the outer halo are dominated by retrograde orbits but can also possess rotational velocities less retrograde or highly prograde, due to the large velocity dispersion of the outer halo ( $\sim 165 \text{ km s}^{-1}$ ; [Carollo 等, 2010](#)). This is clearly evident in the right panel of Figure 4 in ([Carollo 等, 2014](#)) . Figure 5.7 shows the total energy,  $E$ , as a function of the angular momentum in the vertical direction,  $L_Z$ , for the program stars. In the top panel, the black filled star symbol represents HD2796, while the red filled star symbols denote the CEMP stars. The grey horizontal area shows the range of binding energy values defining the *transition zone* between the inner- and the outer-halo components ( $-1.1 \text{ km}^2 \text{ s}^{-2} < E < -0.9 \text{ km}^2 \text{ s}^{-2}$ ), which is defined as the energy range where stars have similar probability to be members of these components. The green dashed curve represents the locus of stars possessing orbits with constant apo-galactic radius  $r_{\text{apo}} = 15 \text{ kpc}$ . In the bottom panel the magenta star symbols denote the CEMP-no stars in the inner halo, classified according to their value of binding energy and apo-galactic distance, the CEMP-r/s star (J2114–0616) is represented by an orange filled square and it is member of the outer halo.

Figure 5.8 shows the galactocentric rotational velocity as a function of the metallicity for the program stars. It is interesting to note that J2114–0616 possesses a prograde motion (rotate in the same direction of the galactic disk) with velocities within  $\sim 2\sigma$  (CEMP-r/s; J2114–0616) of the mean rotational velocity of the outer halo population ( $-80 \text{ km s}^{-1}$ ). Highly prograde stars in the outer halo were also found in the sample of CEMP stars reported in [Carollo 等 \(2014\)](#) ; Figure 4).

Numerical cosmological simulations of MW-mass galaxies predict that stars in the inner halo of the MW formed mainly from massive subgalactic fragments that experienced an extended star formation activity ([Zolotov 等, 2009](#); [Font 等, 2011](#); [McCarthy 等, 2012](#); [Tissera 等, 2013, 2014](#)), while outer halo stars formed predominantly in lower-mass subgalactic fragments with short or truncated star formation history ([Carollo 等, 2007, 2010](#); [Beers 等, 2012](#); [Tissera 等, 2013, 2014](#); [Carollo 等, 2016, 2018](#)). The central regions of simulated halos (within  $\sim 15 \text{ kpc}$ ) have an important contribution of in-situ stars (formed in the main progenitor galaxy) which have various possible origins ([Brook 等, 2004](#); [Zolotov 等, 2009](#); [Font 等, 2011](#); [House 等, 2011](#); [Tissera 等, 2013](#);

Cooper 等, 2015; Pillepich 等, 2015; Monachesi 等, 2016). On the contrary, stars in the outer halo formed primarily in low-mass subgalactic systems which were subsequently accreted. The origin of halo stars can be understood by inspecting a combination of their orbital parameters and integrals of motion. In case of our sample, J2114–0616, possesses orbital parameters, energy and vertical angular momentum that place it in the outer halo population and it likely were formed in low-mass systems outside the virial radius of the progenitor galaxy and accreted later on. The orbital parameters and binding energy of the remaining CEMP stars, J1054+0528, J1529+0804, J1645+4357 and J2216+2232, suggest that they are members of the inner halo population. However, their metallicity and C-enhancement indicate that they may have formed not in situ but in small mass subgalactic fragments which were accreted very early on and contributed to the old central regions of the halo system (Tissera 等, 2018; Carollo 等, 2018).

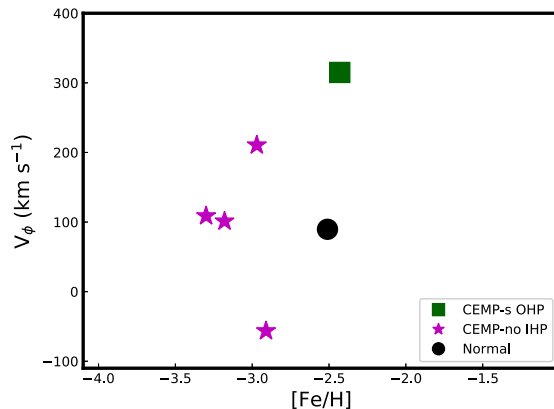


**图 5.8 Galactocentric rotational velocity vs metallicity for the program stars color coded as in Figure 12.**



## 第 6 章 Chemodynamical Analysis of Six Low-Metallicity Stars in the Galactic Halo

### 6.1 Results and Discussion

#### 6.1.1 Chemical Abundance Comparison with Literature Data

To identify any possible chemical peculiarities in our sample, we compared our determinations with data from the literature. Figure 6.1 shows some of the light-element abundances, compared to C-normal stars taken from [Yong 等 \(2013\)](#). The detectable light-elements have similar abundance ratios to those reported in literature halo stars, suggesting that our sample stars have been likely formed from a well-mixed gas cloud.

All our sample stars have been evolved into the red giant branch, suggesting that some internal mixing occurred and thus the atmospheric carbon abundances have been altered. [Placco 等 \(2014b\)](#) studied a sample of 505 metal-poor stars and developed a correction procedure that recovers the initial atmospheric carbon abundance. We obtained high  $[C/Fe]_{corr}$  values for J1630+0953 and J2216+0246 ( $[C/Fe]_{corr} = +0.62$  and 0.42 dex, respectively), which brings the final abundances to  $[C/Fe]=1.26$  and 0.70. From these final values and the definition of the CEMP (CEMP  $[C/Fe] \geq 0.7$ ; [Aoki 等 2007](#)), we classify J1630+0953 and J2216+0246 as carbon-enhanced metal-poor stars, while the rest of our program stars are carbon-intermediate.

The substantial depletion of carbon in J1630+0953 and J2216+0246 suggests that the chemical patterns observed in these two stars should be accompanied with nitrogen enhancement. However, we were only able to detect nitrogen in the spectrum of J1630+0953 ( $[N/Fe]=0.88$ ), which is in line with its evolutionary status, while J2216+0246 spectrum show no reliable CN features.

We have determined chemical abundances for up to nine neutron-capture elements in our sample stars. Of particular interest, the observed Sr and Ba abundances could help us better understand their nucleosynthesis pathway(s), considering that Sr (first s-process peak) may be synthesized by the main or weak s-process, while Ba (second s-process peak) primarily synthesized by the main s-process ([Qian 和 Wasserburg, 2003, 2008; Andrievsky 等, 2011; Hansen 等, 2014](#)). Furthermore, [Cristallo 等 \(2009,](#)

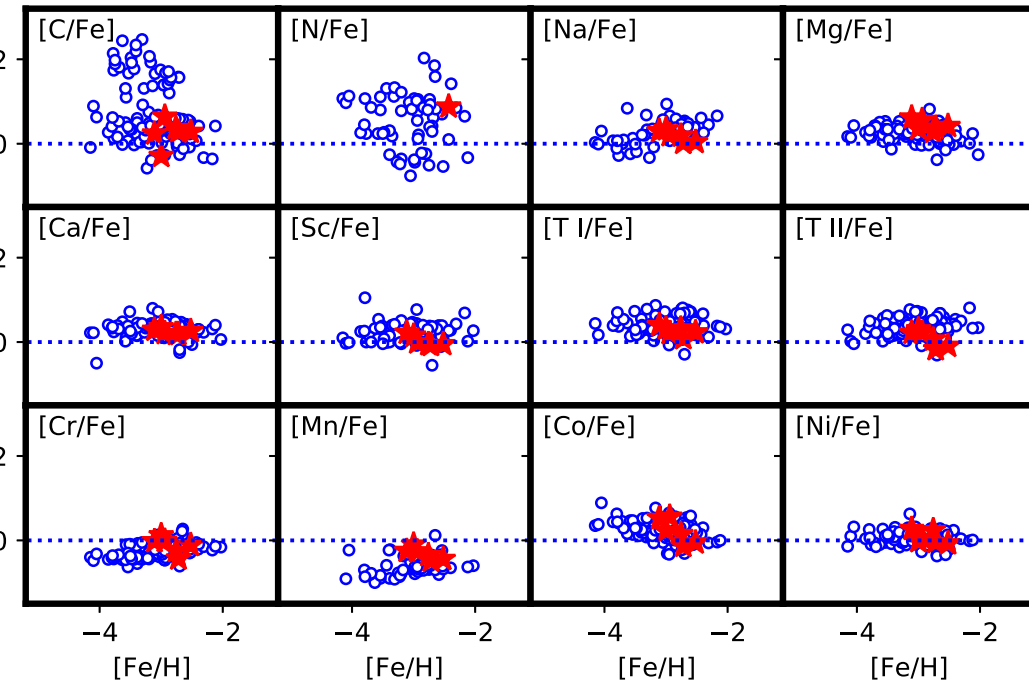


**图 6.1 Selected light-elements abundances of our sample stars (red filled stars) overlaid with  $[X/Fe]$  of carbon-normal metal-poor stars adopted from [Yong 等 \(2013\)](#) (blue open circles). Our derived  $[X/Fe]$  show no significant differences compared to the literature data.  $[C/Fe]$  values do not represent the carbon abundances of the natal gas.**

[2011](#)) and [Lugardo 等 \(2012\)](#) predicted that low and high  $[Sr/Ba]$  ratios could help discriminate between low-mass and massive metal-poor AGB stars, respectively. This further suggests that the production of Sr and Ba are linked to various astrophysical sites. On the other hand, [Aoki 等 \(2013\)](#) suggested that these elements could be synthesized in the same event, and the observed  $[Sr/Ba]$  ratios can be explained by the stars collapse time into a black-hole.

Figure 6.2 shows the  $[Sr/Ba]$  abundance ratios of our program stars (filled red stars) and carbon-normal stars from [François 等 \(2007\)](#) (green open circles) [Yong 等 \(2013\)](#) (blue open circles), as a function of  $[Ba/Fe]$ . All of the sample stars show no significant differences from the trends presented by [François 等 \(2007\)](#) and [Yong 等 \(2013\)](#). However, abundances from elements in the first s-process peak in J0326+0202 ( $[Sr/Ba] = 0.14$ ) and J1413+1727 ( $[Sr/Ba] = 0.20$ ) appear to be enriched more than the second peak, thus an additional process is required to explain these high  $[Sr/Ba]$

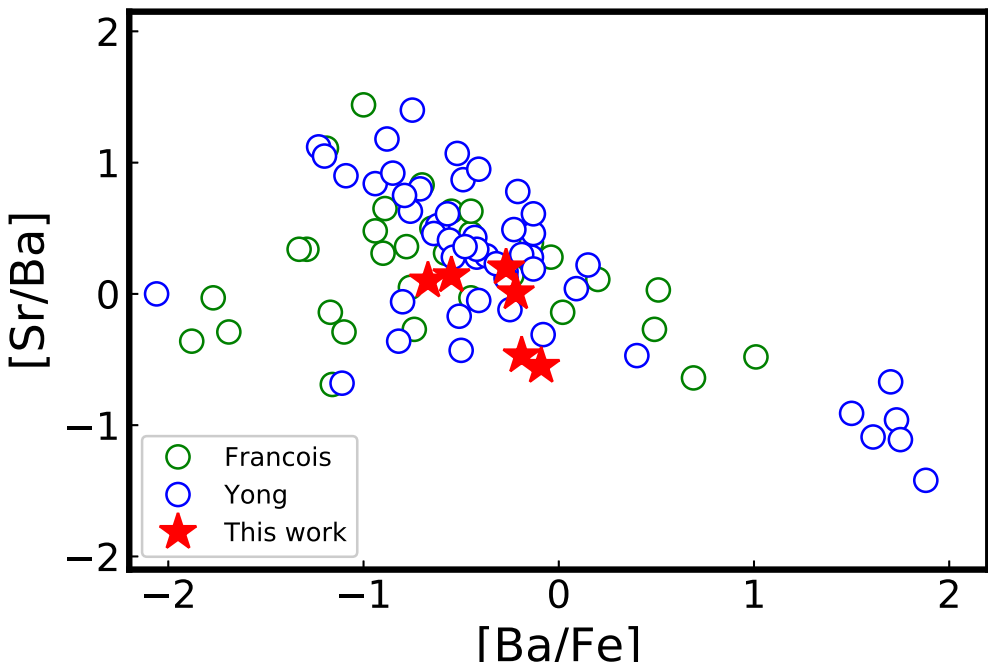
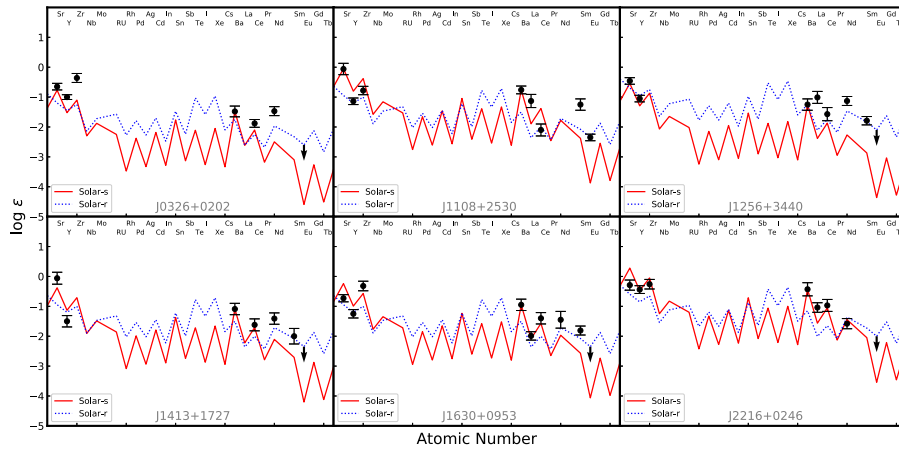


图 6.2 The determined abundance ratios  $[\text{Sr}/\text{Ba}]$  of our sample stars (red filled stars), versus  $[\text{Ba}/\text{Fe}]$ . The green and blue open circles denote literature data adapted from [François 等 \(2007\)](#) and [Yong 等 \(2013\)](#), respectively.

ratios. J1630+0953 and J2216+0246 satisfied the CEMP definition ( $[\text{C}/\text{Fe}] \geq 0.7$ ; [Aoki 等 2007](#)). In addition, we determined low Ba abundances ( $[\text{Ba}/\text{Fe}] < 0.0$ ) for these stars. Therefore, J1630+0953 and J2216+0246 can be classified as CEMP-no stars ([Beers 和 Christlieb, 2005](#); [Aoki 等, 2007](#); [Placco 等, 2014b](#)).

By comparing the observed neutron-capture abundance patterns in our sample stars with the solar system (SS) r- and s-fractions, we can gain insights into the nature of their heavy element enrichment. Figure 6.3 shows the heavy element abundance patterns of our sample stars compared with the SS r- and s-fractions, adopted from [Burris 等 \(2000\)](#). The SS s-process components are normalized to match the observed Ba (solid line), and the SS r-process patterns are normalized to match the observed Eu (dotted line). The derived abundances for Sr, Y, and Zr (within observational errors) in J0326+0202 seem to be inconsistent with the SS distributions. These discrepancies require an additional process(es) to interpret the overall neutron-capture abundance pattern observed in this star. However, these elements seem to be consistent with the SS s-process distributions



**图 6.3** Elemental abundance patterns for the heavy element distribution in our sample stars (filled circles denote detections, and arrow denotes  $3\sigma$  upper limits derived from Eu2 line), compared with scaled solar system r- and s-process components adopted from [Burris 等 \(2000\)](#). The solar system r-process patterns are scaled to match Eu, and the solar system s-process patterns are scaled to match Ba.

for the rest of our sample stars. Heavier elements ( $Z \geq 56$ ) in J0326+0202, J1256+3440, J1413+1727, and J1630+0953 are in better agreement with the normalized SS r-process than the normalized SS s-process. The heavier elements in J2216+0246 seem to favor the normalized SS s-process. The abundance pattern in J1108+2530 is not in agreement with the SS abundance pattern.

Figure 6.4 shows the heavy element abundance patterns in our sample stars compared with abundance patterns of HD 122563 (the dashed gray line, [Honda 等, 2006](#); [Roederer 等, 2012](#)), CS 22892–052 (the solid red line, [Sneden 等, 2003, 2009](#); [Roederer 等, 2009](#)), and predicted yields from s-process nucleosynthesis in TP-AGB stars (the dotted blue line, [Sneden 等, 2008](#); [Bisterzo 等, 2011](#)). These patterns can be used as weak component of the r-process (HD 122563), main component of the r-process (CS 22892–052), and main component of the s-process (TP-AGB yields) representatives ([Roederer 等, 2014b](#)). The abundance pattern of HD122563 and CS 22892–052 are renormalized to match the observed Eu, and the dotted blue line is renormalized to match the observed Ba. The abundance patterns for the heavy elements ( $Z \geq 56$ ) observed in the sample stars are in better agreement with the weak component of the r-process (represented by

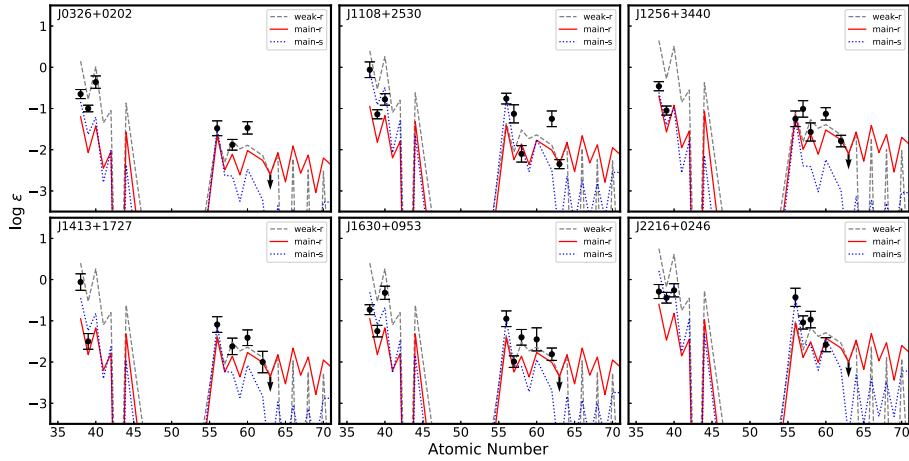


**图 6.4** Neutron-capture element patterns in our sample stars. Filled circles denote detections, and arrow denotes  $3\sigma$  upper limits derived from Eu2 line. The dashed gray line denotes the observed abundances for the neutron-capture elements in HD122563 (Honda 等, 2006; Roederer 等, 2012). The solid red line denotes the observed abundances for the neutron-capture elements in CS 22892-052 (Sneden 等, 2003, 2009; Roederer 等, 2009). The dotted blue line denotes predicted yields from s-process nucleosynthesis in TP-AGB stars (Sneden 等, 2008; Bisterzo 等, 2011). The physical meaning of these three lines are discussed in the text.

HD 122563), with a partial s-process contribution in J1108+2530, J1630+0953, and J2216+0246.

In addition to the possible nucleosynthesis pathway(s) suggested above, it is now commonly acknowledged that the formation of Pop II low-mass stars requires additional coolants compared to the formation of Pop III massive stars (e.g., Yoshida 等, 2006; Glover, 2013; Greif, 2015). At present, a widely acceptable scenario tries to explain the transition from Pop III to Pop II stars by the notion of the fine-structure cooling of the C2 and O1 lines (e.g., Bromm 和 Loeb, 2003; Santoro 和 Shull, 2006). Therefore, C- and O-poor stars can place crucial constraints on the conditions under which metallicity of the ISM the Pop II stars may have been formed.

Frebel 等 (2007) suggested a criterion for the transition to Pop II (“transition discriminant” –  $D_{trans} = -3.5$ ), which combines logarithmic abundance ratios of [C/H] and [O/H]. Figure 6.5 shows the calculated  $D_{trans}$  for our sample stars and

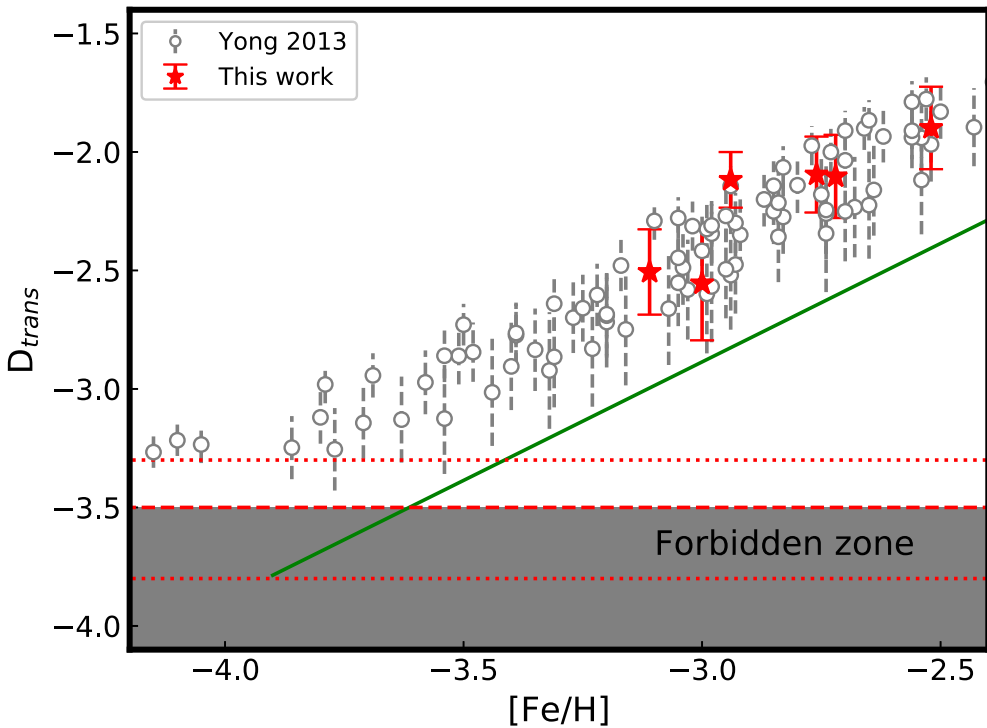
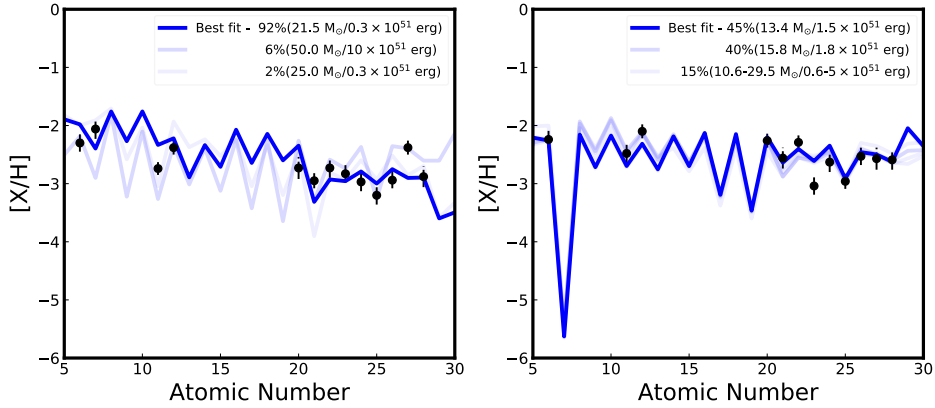


图 6.5  $D_{trans}$  as a function of  $[Fe/H]$  for our target stars, compared with [Yong 等 \(2013\)](#). The solid green line denotes the scaled solar pattern, the red dashed line denotes the limit of  $D_{trans}$  based on the model described in [Frebel et al. \(2007\)](#), and the red dotted lines show the uncertainty of the model. The shaded area is the Forbidden Zone, where there is insufficient C and O induced cooling for low-mass star formation.

carbon-normal stars adopted from [Yong 等 \(2013\)](#). The green solid line denotes the solar  $D_{trans}$  values adopted from [Asplund 等 \(2009\)](#), the red dashed and the red dotted lines denote the limit of  $D_{trans}$  and its associated uncertainty, respectively, and the gray shaded area represents the Forbidden Zone. Even though the empirical formula of the  $D_{trans}$  requires both abundances ( $[C/H]$  and  $[O/H]$ ), it is possible to calculate  $D_{trans}$  where only one of these abundance ratios is known. Here we assume that  $[O/Fe] = 0.88 \pm 0.28$ , following the linear relation between the  $[C/O]$  and  $[C/Fe]$  suggested by [Cayrel 等 \(2004\)](#). We can notice that our sample stars are located above the solar  $D_{trans}$  values and the Forbidden Zone, suggesting that they may have likely formed from a gas cloud exhibiting fine-structure cooling process.



**图 6.6 The determined  $[X/H]$  abundance ratios of J1630+0953 (left panel) and J2216+0246 (right panel) as a function of atomic number, overlaid with simulated abundance patterns by several best fit models, transparent by their fractional appearance. The best fits and their properties are discussed in the text.**

### 6.1.2 J1630+0953 and J2216+0246 Possible Progenitors

Under the assumption that J1630+0953 and J2216+0246 are CEMP-no stars, we decided to gain insights into their putative progenitors, by comparing their abundance patterns with theoretical predictions from Heger 和 Woosley (2010). For the convenience of the reader, it is worth mentioning that this grid does not consider rotation and has a  $\chi^2$  matching algorithm over 16,800 models. The parameter space includes progenitor masses ( $10\text{-}100 M_\odot$ ), explosion energies ( $0.3\text{-}10 \times 10^{51}$  erg), and mixing factor ( $f_{mix}$ ) ranging from no mixing to nearly complete mixing (see Heger 和 Woosley, 2010, for more information).

We sampled  $10^4$  sets of the determined chemical abundances of J1630+0953 and J2216+0246, assuming a normal distribution. To facilitate this exercise, we use the determined  $\log \epsilon(X)$  of J1630+0953 and J2216+0246 as the central values and dispersions given by the associated uncertainties. This allowed us to generate  $10^4$  abundance patterns for each star. We use the publicly available STARFIT code (Heger 和 Woosley, 2010) to find the progenitor mass and explosion energy for the  $10^4$  abundance patterns. Figure 6.6 shows the determined abundances of J1630+0953 and J2216+0246 (black filled circles), with error bars representing their associated uncertainties, overlaid with abundance patterns generated by several best fit models. Figure 6.7 shows posterior

distributions for the mean squared residuals of the  $10^4$  fittings, for both stars. Legends show the median value and the median absolute deviation (MAD). The MAD can be used as a robust estimator on how the data spreads out. In other words, the larger the MAD, the greater the variability in  $\chi^2$ .

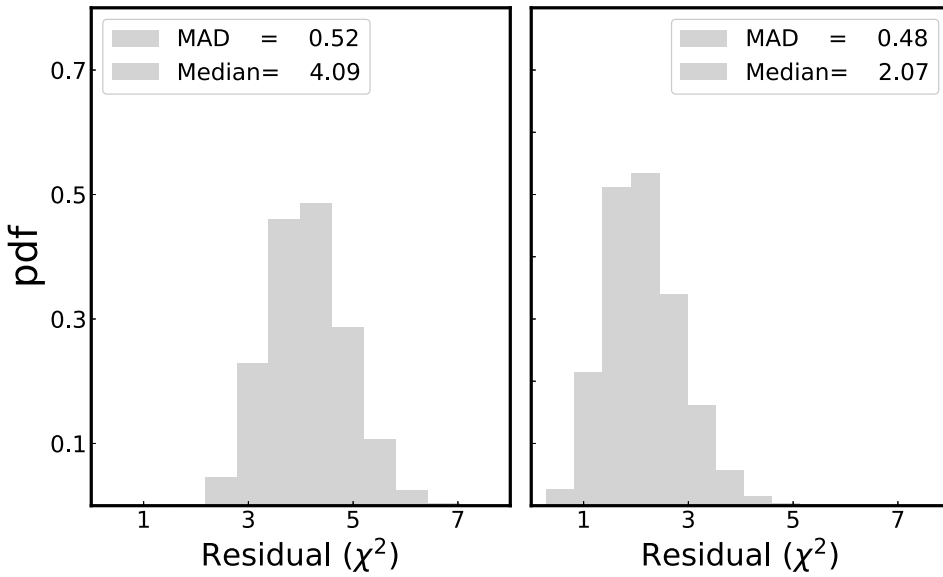


**图 6.7 Posterior Distributions for  $\chi^2$ , of the 10,000 simulations, for J1630+0953 (left panel) and J2216+0246 (right panel). The median and median absolute deviation (MAD) are shown in legends.**

For J1630+0953, an SN model with mass  $21.5 M_{\odot}$  and explosion energy  $0.3 \times 10^{51}$  erg was the most frequent model (92 %) to fit the generated abundance patterns. Another model with mass  $50.0 M_{\odot}$  and explosion energy  $10.0 \times 10^{51}$  erg fit 6 % of the generated abundance patterns, while the remaining of the  $10^4$  generated abundance patterns (249) had best fit models with mass  $25.0 M_{\odot}$  and explosion energy  $0.3 \times 10^{51}$  erg.

For J2216+0246, a larger number of SN models were able to fit our  $10^4$  generated abundance patterns. About 45 % (4532) of the generated abundance patterns had best fit with an SN model with mass of  $13.4 M_{\odot}$  and explosion energy of  $1.5 \times 10^{51}$  erg. Another SN model with mass  $15.8 M_{\odot}$  and explosion energy  $1.8 \times 10^{51}$  erg was the best fit of 40 % (3976) of the generated abundance patterns; while 21 different SN models correspond to the best fit for the rest of the  $10^4$  generated abundance patterns (1492). In total, 23 different SN models were the best fits for the  $10^4$  generated abundance patterns.

of J2216+0246, in the mass range  $10.6\text{-}29.5 M_{\odot}$  and explosion energies  $0.6\text{-}5 \times 10^{51}$  erg. The abundance patterns simulated by these 23 models are shown in the right panel of Figure 6.6, and color-coded by their fractional appearance.

Regarding the most frequent SN model in the exercise of J1630+0953, it can be seen through either visual checking or  $\chi^2$ , that the carbon ( $Z=6$ ) and nitrogen ( $Z=7$ ) abundances are well reproduced (within  $\sim 2 \sigma$ ). Sodium ( $Z=11$ ) is overproduced, while magnesium ( $Z=12$ ) is well reproduced (within  $\sim 1 \sigma$ ). Elements from calcium to iron ( $Z=20\text{-}26$ ) are also well reproduced (within  $\sim 2 \sigma$ ). The cobalt ( $Z=27$ ) abundance is underproduced, which is not unusual for theoretical models, where an SN model with higher mass, explosion energy, and mixing factor may result better Co fitting, although this could worsen other elements fittings (see [Tominaga 等, 2014](#), and references therein), while the Nickel ( $Z=28$ ) is well reproduced. The predicted yields in  $\sim 85\%$  of the SN models reproduced the observed abundances for J2216+0246 within  $\sim 2 \sigma$ .

In general, J1630+0953 has possible progenitor with  $21\text{-}25 M_{\odot}$  stellar mass and explosion energy  $0.3 \times 10^{51}$  erg, while the mass and explosion energy of the possible progenitors of J2216+0246 are somewhat lower ( $10.6\text{-}29.5 M_{\odot}$ ,  $0.6\text{-}5 \times 10^{51}$  erg). Recently, [Ishigaki 等 \(2018\)](#) compared the abundance patterns of 219 EMP stars with supernova yields of metal-free stars to find that the best fitting progenitor SNe of most EMP stars are PopIII stars in the range  $15\text{-}25 M_{\odot}$ . The analysis presented in this paper supports this hypothesis and suggests that the peak around  $20 M_{\odot}$  may reflect the Pop III initial mass function and more massive SN might be more energetic that their ejecta escape from the halo and would never been incorporated into the next generation of stars.

### 6.1.3 Kinematics and Dynamics

The full space motion of our sample stars can be derived by combining positions ( $\alpha, \delta$ ), proper motions ( $\mu_{\alpha} \cos \delta, \mu_{\delta}$ ), available in Gaia DR2 ([Gaia Collaboration 等, 2018](#)), the line-of-sight velocities ( $V_r$ ), derived from our high-resolution spectra, and a Galactic potential model. Errors are provided in Gaia DR2, thus the inversion of the parallax ( $\varpi$ ) to calculate the stellar distance is not appropriate (see [Luri 等, 2018](#), for a recent discussion). Therefore, we adopted distances from [Bailer-Jones 等 \(2018\)](#),

who inferred distances to all stars, with published parallaxes, in Gaia DR2 using a weak distance prior. Gaia DR2 ID source, positions, proper motions, distances, and the associated uncertainties for these quantities.

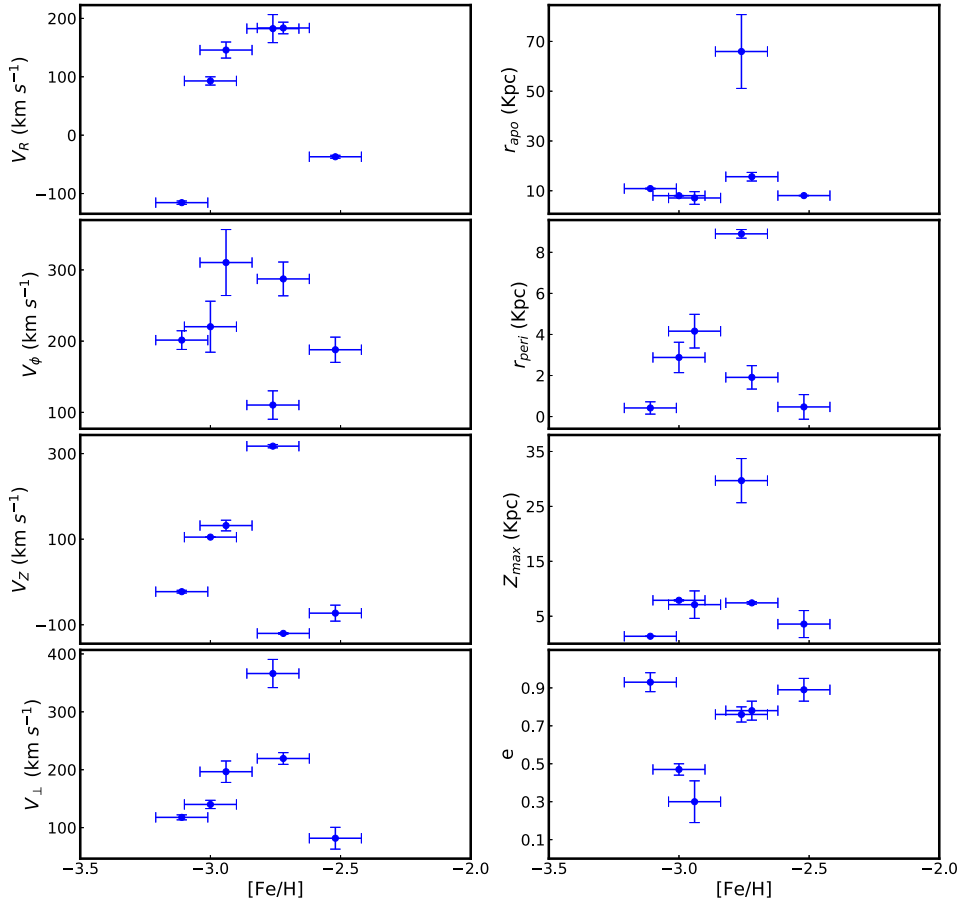


**图 6.8** The left panel shows the Galactic velocities and the right panel shows the orbital parameters for our sample stars as functions of  $[\text{Fe}/\text{H}]$ . The y-axis error bars denote the 16<sup>th</sup> and 84<sup>th</sup> percentiles, while the x-axis error bars represent a typical  $[\text{Fe}/\text{H}]$  uncertainty (0.10 ~dex).

We sampled  $10^4$  sets of the observed astrometric quantities (RA, DEC,  $\varpi$ , RV,  $\mu_\alpha \cos \delta$ ,  $\mu_\delta$ ) from the measurement errors of each quantity for each star in our sample. We assume that the Sun has an offset above the Galactic midplane of  $z_\odot = 25 \text{ pc}$  (Jurić 等, 2008),  $R_\odot = 8.2 \text{ kpc}$  (Bland-Hawthorn 和 Gerhard, 2016) as the distance from the Galactic center, circular velocity  $v_0 = 232.8 \text{ km s}^{-1}$  at the Solar position (McMillan, 2017),

and solar peculiar motion  $(U_\odot, V_\odot, W_\odot) = (11.1, 12.24, 7.25) \text{ km s}^{-1}$  ([Bland-Hawthorn 和 Gerhard, 2016](#)). We calculate the Galactocentric Cartesian  $(X_{GC}, Y_{GC}, Z_{GC})$  coordinates as follows:

$$\begin{aligned} X_{GC} &= R_\odot - d \cos(b) \cos(\ell) \\ Y_{GC} &= -d \cos(b) \sin(\ell) \\ Z_{GC} &= d \sin(b) + z_\odot \end{aligned}$$

We calculated and corrected the Galactic space-velocity components  $(U, V, W)$  using the Astropy Galactocentric frame package ([Astropy Collaboration 等, 2013, 2018](#)): U (positive toward the Galactic center), V (positive in the direction of Galactic rotation) and W (positive toward the North Galactic Pole). Moreover, we define the angle  $\phi = \tan^{-1}(Y_{GC}/X_{GC})$  and then calculate the cylindrical velocities components for our sample as follows:

$$\begin{aligned} V_R &= U \cos(\phi) + V \sin(\phi) \\ V_\phi &= U \sin(\phi) - V \cos(\phi) \\ V_z &= W \end{aligned}$$

We adopted the `MWPotential2014` as a Galactic potential model (see [Bovy, 2015](#), for more information) to integrate the corresponding stellar orbits, apocentric ( $r_{\text{apo}}$ ) and pericentric ( $r_{\text{peri}}$ ) radii, the maximum offset from the Galactic midplane ( $Z_{\text{max}}$ ), and eccentricity, defined as  $e = (r_{\text{apo}} - r_{\text{peri}})/(r_{\text{apo}} + r_{\text{peri}})$ . In addition, we derived the total orbital energy, defined as  $E = (1/2)\mathbf{v}^2 + \Phi(\mathbf{x})$  and the angular momentum in the vertical direction, defined as  $L_z = R \times \mathbf{V}_\phi$ , where  $R$  denotes the distance from the Galactic center projected onto the disk plane.

Figure 6.8 shows the behavior of the calculated velocities and orbital properties, for our sample stars, as a function of [Fe/H]. Error bars denote typical [Fe/H] uncertainty

(x-axis) and the 16th and 84th percentiles (y-axis). It is possible to see that 66 % of our sample is moving away ( $V_R > 0$ ) from the Galactic center, 100% on prograde ( $V_\phi > 0$ ) orbits, and 50 % moving north ( $V_Z > 0$ ), as they pass through the Galactic disk. The right panel shows that only J1108+2530 and J1256+3440 have  $r_{\text{apo}} > 15.0$  kpc and  $e > 0.7$  and the majority of our sample stars pass the Galactic center at  $r_{\text{peri}} = 4.16$ . Also, 66% of our sample stars travel at least 7 kpc above or below the Galactic plane.

An additional tool that can be used for this analysis is the Lindblad diagram. By plotting the total orbital energy vs. angular momentum in the vertical direction, one can assess the accretion origin of the sample stars. [Carollo 等 \(2014\)](#) explored kinematics, integrals of motion, and orbital properties of 323 VMP stars, to establish a method to assign membership to the inner- and outer-halo populations. In this context, stars with total energy  $> -0.9 \text{ km}^2 \text{ s}^{-2}$  and  $r_{\text{apo}} > 15$  kpc can be considered as outer-halo stars. Otherwise, stars can be considered as members of the inner-halo population.

Figure 6.9 shows the Lindblad diagram (top panel) and the [Carollo 等 \(2014\)](#) criterion (bottom panel) for the sample stars, compared to stars taken from Paper I. CEMP-no stars are shown as blue filled stars, CEMP-r/s star as orange filled square, and C-normal stars as black filled stars. The green dashed curve represents the locus of the points that possess constant apo-Galactic radius,  $r_{\text{apo}} = 15$  kpc. The light-gray shaded area encloses the transition zone energies. It is possible to see that J1630+0953 and J2216+0246, within the error bars, are likely to have inner-halo kinematics.

Many numerical cosmological simulations suggest that the main origin of the Milky Way inner and outer-halo stars are massive and low-mass subgalactic fragments, respectively ([Zolotov 等, 2009](#); [Font 等, 2011](#); [McCarthy 等, 2012](#); [Beers 等, 2012](#); [Tissera 等, 2013, 2014](#)). In general, We can understand the origin of our stars by examining a combination of their orbital parameters and integrals of motion. The derived orbital parameters and the calculated total energy of J1630+0953 and J2216+0246 suggest that they probably belong to the inner-halo population. However, their metallicity and C-enhancement indicate that they may have formed not in situ but in small mass subgalactic fragments that were accreted very early on and contributed to the old central regions of the halo system (e.g., [Tissera 等, 2018](#)).

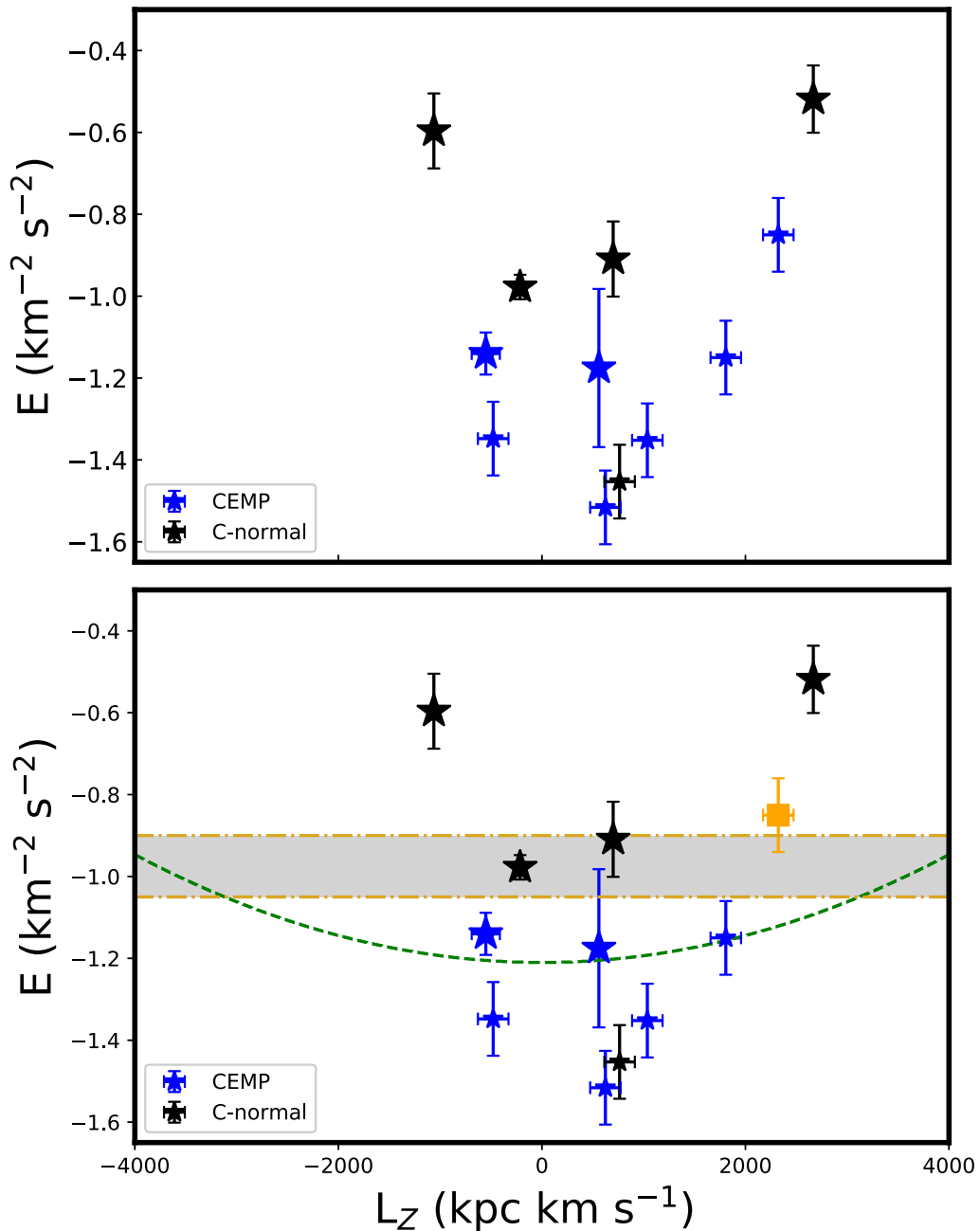


图 6.9 Lindblad diagram for program stars and data taken from Paper I. Top panel shows the distribution of this sample based on [C/Fe] abundance ratios, carbon normal (black stars) and CEMP stars (red stars). Bottom panel shows the distribution of this sample based on Carollo 等 (2014) criterion. CEMP-no stars are shown as blue filled star, CEMP-r/s as orange filled square, and C-normal stars as black filled star. The green dashed curve represents the locus of the points that possess constant apo-Galactic radius,  $r_{apo} = 15$  kpc. The light-gray shaded area encloses the transition zone energies.



## 第7章 Conclusions

In this work, we analyzed 12 metal-poor stars chosen from the LAMOST database and followed-up, for the first time, with high-resolution observations using Lick/APF. We have presented stellar parameters and full detail chemical abundances (25 individual elements from C to Eu), for these stars. Our analysis shows no significant differences compared with the general abundance trends as reported in previous studies of metal-poor stars. In particular, the chemical abundance patterns of our sample stars reveal that our sample contain five carbon normal stars and seven carbon-enhanced metal-poor (CEMP) stars: (i)The CEMP-r/s star J2114–0616 with  $[C/Fe]=1.37$ ,  $[N/Fe]=1.88$ ,  $[Ba/Fe]=1.00$ , and  $[Eu/Fe]=0.84$ , (ii) The CEMP-r star J1054+0528 with  $[C/Fe]=0.82$ ,  $[Eu/Fe]=0.44$  and  $[Ba/Fe]=-0.52$  (iii) The CEMP-no ( $[C/Fe] \geq +0.7$  and  $[Ba/Fe] < 0.0$ ) stars J1529+0804, J1630+0953, J1645+4357, J2216+0246, and J2216+2232..

We have attempted to characterize the formation scenario and the progenitors of our CEMP-no stars. Our program stars are located above the solar  $D_{trans}$  values and the Forbidden Zone, suggesting that they may have likely formed from a gas cloud exhibiting fine-structure cooling process. Furthermore, we have compared  $10^4$  generated sets of the determined chemical abundances of the light-element abundances of J1630+0953 and J2216+0246 with predicted yields from nonrotating massive-star models. About  $\sim 94\%$  of the models predicted that the mass and explosion energy of the J1630+0953 progenitor, could be in the  $21\text{--}25 M_\odot$  mass range and  $0.3 \times 10^{51}$  erg, respectively, and only about  $\sim 6\%$  with mass of  $50 M_\odot$  and explosion energy of  $10.0 \times 10^{51}$  erg. In about  $\sim 85\%$  of the models predicted  $13\text{--}16 M_\odot$  mass range and explosion energy of  $1.5\text{--}1.8 \times 10^{51}$  erg for the progenitor of J2216+0246, while the remaining models ( $\sim 15\%$ ) predicted  $10.6\text{--}29.5 M_\odot$  mass range and explosion energy  $0.6\text{--}5 \times 10^{51}$  erg. In general, our comparison suggested that massive stellar progenitors shall be the pollutant source of their birth cloud, and these pollutants then acted as cooling agents. Our result is consistent with recent conclusions given by [Ishigaki 等 \(2018\)](#), which suggest possible progenitors in the  $15\text{--}25 M_\odot$  mass range. This peak ( $\sim 20 M_\odot$ ) may reflect the Pop III

initial mass function. However, this brings the possibility as to whether more massive SN might be more energetic and therefore destroy their host halo and not allow for EMP star formation afterwards.

We have further investigated the kinematics and dynamics of the sample stars, based on Gaia DR2 data. Our results show that all stars are members of the inner-halo population. Nevertheless, the deficiency in iron and enhancement in carbon abundances of J1630+0953 and J2216+0246 strongly suggest that these stars were born in low-mass sub-galactic systems and later accreted during the initial phases of Galaxy assembly and contributed to the old stellar populations of the inner halo.

**Table 1.** Log of the Lick/APF observations.

	ID	Date	RA	DEC	<i>r</i> (mag)	Exptime (s)	S/N (pixel <sup>-1</sup> )	<i>V<sub>r</sub></i> (km s <sup>-1</sup> )
1	HD2796	18 Nov 2015	00 31 16.91	-16 47 40.8	8.51	900*2	43	-60.51
2	J1054+0528	28 May 2015	10 54 33.10	+05 28 12.7	12.65	1800*4	42	82.36
3	J1529+0804	30 May 2015	15 29 53.94	+08 04 48.1	12.49	1800*4	46	23.40
4	J1645+4357	28 May 2015	16 45 14.95	+43 57 12.0	12.79	1800*4	40	-83.20
5	J2114-0616	23 Sep 2015	21 14 01.52	-06 16 10.3	10.81	1200*4	46	-160.32
6	J2216+2232	27 July 2015	22 16 39.31	+22 32 50.4	12.03	1800*4	47	-339.38

NOTE—The S/N ratio per pixel was measured at  $\lambda \sim 4500 \text{ \AA}$ .

**Table 2.** Equivalent widths of our sample.

$\lambda$ (Å)	Species	$\chi$ eV	$\log g f$	HD2796 mÅ	J1054+0528 mÅ	J1529+0804 mÅ	J1645+4357 mÅ	2114–0616 mÅ	J2216+2232 mÅ
4049	C(CH)	—	—	—	syn	—	—	syn	—
4218	C(CH)	—	—	syn	syn	—	—	syn	syn
4248	C(CH)	—	—	—	—	syn	syn	syn	—
4253	C(CH)	—	—	syn	—	syn	—	syn	syn
4261	C(CH)	—	—	—	—	—	syn	—	—
4273	C(CH)	—	—	—	syn	—	syn	syn	syn
4279	C(CH)	—	—	—	—	—	syn	syn	syn
4281	C(CH)	—	—	syn	—	—	—	syn	syn
4292	C(CH)	—	—	—	syn	syn	—	syn	—
4310	C(CH)	—	—	—	—	syn	—	—	syn
4313	C(CH)	—	—	syn	—	—	syn	syn	—
4362	C(CH)	—	—	—	syn	—	—	—	syn
4366	C(CH)	—	—	—	—	—	syn	—	syn
4214	N(CN)	—	—	—	—	—	—	syn	—
6970	N(CN)	—	—	—	—	—	—	syn	—
5889.95	Na I	0.00	0.10	169.6	118.7	66.4	174.2	195.0	140.0
5895.92	Na I	0.00	-0.20	164.8	120.4	65.1	161.1	181.8	159.4
4702.99	Mg I	4.33	-0.44	77.2	26.1	8.8	64.5	73.0	51.3
5172.68	Mg I	2.71	-0.45	217.9	124.4	209.7	211.0	183.6	
5183.60	Mg I	2.72	-0.24	260.2	145.6	147.8	232.1	267.0	218.5
5528.40	Mg I	4.35	-0.50	68.7	36.2	33.7	72.7	81.3	48.0
5711.09	Mg I	4.35	-1.72	3.5	10.5	—	—	9.7	5.3
4283.01	Ca I	1.89	-0.22	60.9	—	15.2	54.9	78.5	59.9
4318.65	Ca I	1.89	-0.21	64.7	—	—	—	22.2	40.0
4425.44	Ca I	1.88	-0.36	50.9	27.2	19.3	—	52.9	—
4454.78	Ca I	1.90	0.26	81.9	31.9	46.5	42.1	76.4	64.9
4455.89	Ca I	1.90	-0.53	43.9	—	18.8	—	38.7	15.9
5261.71	Ca I	2.52	-0.58	15.9	2.3	12.4	—	15.8	9.7
5265.56	Ca I	2.52	-0.11	33.2	—	—	—	34.3	23.1
5512.98	Ca I	2.93	-0.45	8.0	—	17.3	—	—	2.3
5581.97	Ca I	2.52	-0.56	15.3	1.1	1.9	—	6.4	6.1
5588.76	Ca I	2.53	0.36	56.7	—	23.9	25.8	56.0	32.9
5590.12	Ca I	2.52	-0.57	16.2	—	2.0	—	14.0	—
5594.47	Ca I	2.52	0.10	45.8	14.5	11.1	—	50.9	22.9
5598.49	Ca I	2.52	-0.09	36.1	—	6.4	13.9	40.7	19.5
5601.29	Ca I	2.53	-0.52	17.4	—	3.5	2.1	24.7	—
5857.45	Ca I	2.93	0.24	30.6	10.1	11.0	3.8	27.0	18.2
6102.72	Ca I	1.88	-0.77	41.7	16.7	21.3	10.9	37.8	24.5
6122.22	Ca I	1.89	-0.32	70.3	27.3	26.7	43.5	69.4	40.4
6439.07	Ca I	2.53	0.39	69.2	30.2	26.0	27.9	71.3	42.5
6449.81	Ca I	2.52	-0.50	20.9	—	2.3	12.8	21.8	8.0
6493.78	Ca I	2.52	-0.11	62.0	2.5	12.9	22.6	83.8	9.9
6717.69	Ca I	2.71	-0.52	12.4	3.1	3.4	—	15.2	6.0
4246.82	Sc II	0.31	0.24	126.7	70.7	62.3	64.1	143.3	—
4314.10	Sc II	0.62	0.10	101.4	—	—	45.7	106.9	—
4320.75	Sc II	0.61	-0.25	93.8	36.2	—	7.8	85.7	68.5
4325.00	Sc II	0.60	-0.44	81.1	14.4	31.2	15.4	64.6	63.0
4374.46	Sc II	0.62	-0.42	84.1	—	15.0	48.5	—	47.1
4400.40	Sc II	0.61	-0.54	79.7	22.4	38.4	19.8	66.9	52.9
4415.56	Sc II	0.60	-0.67	76.6	27.9	18.7	14.6	60.0	47.1
4670.41	Sc II	1.36	-0.58	26.9	—	—	—	37.9	23.4
5031.02	Sc II	1.36	-0.40	42.6	—	—	—	54.6	21.2
5526.79	Sc II	1.77	0.02	40.7	—	5.5	—	45.8	18.8

**Table 2.** Continued.

$\lambda$ (Å)	Species	$\chi$	$\log gf$	HD2796 eV	J1054+0528 mÅ	J1529+0804 mÅ	J1645+4357 mÅ	2114-0616 mÅ	J2216+2232 mÅ
5641.00	Sc II	1.50	-1.13	—	—	—	—	19.8	—
5667.16	Sc II	1.50	-1.31	6.5	—	—	—	8.9	—
5669.06	Sc II	1.50	-1.20	8.0	3.1	—	—	12.8	—
6604.58	Sc II	1.36	-1.31	10.1	—	2.6	—	10.7	—
4534.78	Ti I	0.84	0.34	47.5	13.3	—	—	46.4	23.9
4544.69	Ti I	0.82	-0.45	15.7	—	12.9	—	13.4	—
4548.76	Ti I	0.83	-0.28	15.0	—	14.5	—	—	—
4656.47	Ti I	0.00	-1.29	16.9	—	28.0	14.5	10.9	10.3
4681.91	Ti I	0.05	-1.02	25.5	12.0	3.1	—	25.3	15.9
4840.87	Ti I	0.90	-0.45	11.8	—	1.7	—	12.1	—
4981.73	Ti I	0.85	0.57	62.3	11.7	8.6	22.0	46.9	41.5
4991.07	Ti I	0.84	0.45	58.7	17.4	14.3	16.6	65.1	43.9
4999.50	Ti I	0.83	0.32	51.8	19.2	—	17.3	70.3	23.5
5007.21	Ti I	0.82	0.17	55.2	14.2	16.1	22.4	56.7	32.5
5016.16	Ti I	0.85	-0.48	13.8	—	—	2.2	8.8	6.3
5020.02	Ti I	0.84	-0.33	19.8	2.8	—	—	—	5.3
5035.90	Ti I	1.46	0.26	17.9	4.8	—	1.3	18.1	10.4
5036.46	Ti I	1.44	0.19	11.1	—	—	—	—	6.2
5064.65	Ti I	0.05	-0.94	31.2	8.5	17.2	8.0	39.3	21.8
5173.74	Ti I	0.00	-1.06	25.9	4.3	9.1	15.5	34.9	19.3
5192.97	Ti I	0.02	-0.95	23.2	19.0	—	11.8	40.2	20.9
5210.38	Ti I	0.05	-0.82	38.9	7.4	3.3	12.4	37.9	24.1
5866.45	Ti I	1.07	-0.78	—	2.5	—	—	—	—
4053.82	Ti II	1.89	-1.07	61.0	8.5	—	15.2	—	14.8
4161.53	Ti II	1.08	-2.09	52.6	3.3	—	16.6	54.5	—
4163.64	Ti II	2.59	-0.13	57.4	7.0	—	14.1	29.9	28.4
4287.87	Ti II	1.08	-1.82	67.5	36.2	11.0	36.2	53.5	40.8
4300.04	Ti II	1.18	-0.46	117.8	66.4	—	—	—	—
4330.70	Ti II	1.18	-2.09	36.4	—	—	—	45.3	13.5
4337.92	Ti II	1.08	-0.96	105.5	28.1	—	63.1	78.9	62.8
4344.29	Ti II	1.08	-1.93	67.4	17.5	5.9	—	—	12.2
4395.03	Ti II	1.08	-0.54	132.6	67.7	77.1	98.9	99.0	89.2
4395.84	Ti II	1.24	-1.93	51.9	20.1	11.8	4.9	27.0	—
4399.77	Ti II	1.24	-1.20	93.6	—	47.3	30.9	97.4	55.8
4417.72	Ti II	1.16	-1.19	102.1	38.9	44.7	—	84.8	50.4
4418.33	Ti II	1.24	-1.99	56.0	2.7	7.5	17.3	30.7	16.2
4443.80	Ti II	1.08	-0.71	124.6	50.1	75.9	55.9	116.1	89.0
4444.55	Ti II	1.12	-2.20	51.8	—	14.2	6.8	50.6	27.2
4450.48	Ti II	1.08	-1.52	81.0	28.3	40.3	48.5	69.5	61.4
4464.45	Ti II	1.16	-1.81	73.0	—	29.6	—	73.8	38.2
4468.49	Ti II	1.13	-0.63	126.9	65.6	66.8	—	123.8	67.9
4470.83	Ti II	1.16	-2.28	53.6	—	8.5	—	42.2	—
4501.27	Ti II	1.12	-0.77	121.9	52.1	—	88.7	104.2	66.8
4533.97	Ti II	1.24	-0.77	126.3	47.5	63.6	88.3	130.4	95.0
4563.77	Ti II	1.22	-0.96	114.8	72.9	58.1	81.6	110.1	62.5
4571.97	Ti II	1.57	-0.31	119.1	24.9	58.8	71.7	117.8	61.9
4589.92	Ti II	1.24	-1.79	74.1	23.3	—	29.3	74.4	38.9
4708.65	Ti II	1.24	-2.37	34.9	21.5	—	15.0	9.9	19.4
4779.98	Ti II	2.05	-1.37	38.8	—	13.8	12.5	43.7	20.0
4805.08	Ti II	2.06	-0.96	55.5	26.1	12.0	17.2	63.6	33.2
4865.61	Ti II	1.12	-2.81	26.1	—	17.4	—	24.2	—
5129.16	Ti II	1.88	-1.34	48.3	—	—	18.0	64.8	25.8
5154.07	Ti II	1.57	-1.78	48.8	13.9	8.6	8.2	61.6	—

**Table 2.** Continued.

$\lambda$ (Å)	Species	$\chi$	$\log gf$	HD2796 eV	J1054+0528 mÅ	J1529+0804 mÅ	J1645+4357 mÅ	2114-0616 mÅ	J2216+2232 mÅ
5185.90	Ti II	1.89	-1.35	42.3	11.9	10.6	7.3	59.4	21.3
5226.54	Ti II	1.57	-1.23	78.9	26.1	30.6	33.2	79.9	50.0
5336.78	Ti II	1.58	-1.63	56.7	15.2	11.3	13.3	65.3	—
4379.23	V I	0.30	0.58	25.3	8.7	—	—	—	2.6
4254.33	Cr I	0.00	-0.09	—	35.5	—	106.5	—	77.9
4274.80	Cr I	0.00	-0.22	—	40.9	70.5	114.2	—	87.3
4289.72	Cr I	0.00	-0.37	100.8	62.2	62.7	122.8	112.8	—
4600.75	Cr I	1.00	-1.26	17.7	83.2	—	12.5	—	—
4616.14	Cr I	0.98	-1.19	—	—	13.4	—	31.8	8.8
4626.19	Cr I	0.97	-1.32	19.2	—	12.0	—	16.4	8.6
4646.15	Cr I	1.03	-0.74	36.2	23.2	10.2	—	43.8	24.0
4651.29	Cr I	0.98	-1.46	11.8	—	2.5	—	14.2	4.6
4652.15	Cr I	1.00	-1.04	25.5	—	7.6	—	30.1	6.4
5206.04	Cr I	0.94	0.02	90.8	40.4	37.0	—	90.5	67.4
5208.42	Cr I	0.94	0.17	100.3	44.8	46.6	64.0	—	69.5
5247.56	Cr I	0.96	-1.64	13.9	4.3	4.9	1.6	12.1	1.5
4055.54	Mn I	2.14	-0.08	25.6	—	—	—	—	—
4783.43	Mn I	2.30	0.04	18.5	—	23.1	—	17.3	10.1
4823.52	Mn I	2.32	0.14	25.5	3.4	25.2	36.7	18.1	20.5
4062.44	Fe I	2.85	-0.86	41.7	11.5	16.1	21.5	—	—
4109.80	Fe I	2.85	-0.89	46.6	7.2	—	24.2	—	27.6
4114.44	Fe I	2.83	-1.30	28.9	—	7.8	—	22.7	16.9
4132.90	Fe I	2.85	-1.01	—	—	—	—	30.5	31.1
4134.68	Fe I	2.83	-0.65	—	15.1	17.1	—	57.0	43.8
4143.42	Fe I	3.05	-0.20	67.9	—	—	56.9	—	47.1
4147.67	Fe I	1.49	-2.10	—	—	14.1	51.8	62.5	43.2
4152.17	Fe I	0.96	-3.23	53.2	—	7.2	—	—	19.8
4153.90	Fe I	3.40	-0.32	39.0	—	—	—	43.2	19.5
4156.80	Fe I	2.83	-0.81	55.1	—	—	—	54.1	22.8
4157.78	Fe I	3.42	-0.40	36.5	—	—	24.6	49.5	27.6
4174.91	Fe I	0.92	-2.97	73.6	27.5	—	46.9	—	—
4175.64	Fe I	2.85	-0.83	—	—	—	38.5	—	—
4181.75	Fe I	2.83	-0.37	72.0	31.5	33.2	—	—	57.6
4195.33	Fe I	3.33	-0.49	39.6	8.8	13.1	16.9	—	23.5
4199.10	Fe I	3.05	0.16	—	48.1	—	79.2	—	—
4233.60	Fe I	2.48	-0.58	76.9	—	—	57.8	—	—
4250.12	Fe I	2.47	-0.41	92.1	—	49.2	—	—	—
4250.79	Fe I	1.56	-0.71	118.1	—	—	—	—	95.8
4260.47	Fe I	2.40	0.08	110.4	—	—	113.4	—	—
4271.15	Fe I	2.45	-0.34	98.4	—	—	—	100.8	—
4282.40	Fe I	2.18	-0.78	85.6	—	53.3	—	—	75.2
4337.05	Fe I	1.56	-1.70	83.8	—	34.7	—	—	63.7
4352.73	Fe I	2.22	-1.29	68.1	—	20.0	—	—	—
4375.93	Fe I	0.00	-3.02	113.6	—	70.1	100.4	—	78.1
4407.71	Fe I	2.18	-1.97	—	—	—	30.8	—	11.8
4415.12	Fe I	1.61	-0.62	124.7	—	—	—	—	95.8
4422.57	Fe I	2.85	-1.11	43.0	5.6	5.5	15.6	28.4	14.1
4427.31	Fe I	0.05	-2.92	112.8	54.6	74.1	120.4	—	—
4430.61	Fe I	2.22	-1.66	54.5	12.1	21.6	—	43.5	28.7
4442.34	Fe I	2.20	-1.25	77.7	21.4	44.2	38.3	—	61.7
4443.19	Fe I	2.86	-1.04	41.8	—	20.5	—	36.1	26.5
4447.72	Fe I	2.22	-1.34	68.8	15.2	10.8	57.5	60.7	56.4
4459.12	Fe I	2.18	-1.28	81.6	—	43.0	41.0	78.3	64.1

**Table 2.** Continued.

$\lambda$ (Å)	Species	$\chi$ eV	$\log gf$	HD2796 mÅ	J1054+0528 mÅ	J1529+0804 mÅ	J1645+4357 mÅ	2114-0616 mÅ	J2216+2232 mÅ
4461.65	Fe I	0.09	-3.21	103.7	—	49.7	—	98.6	86.2
4466.55	Fe I	2.83	-0.60	75.5	—	22.7	53.7	—	—
4476.02	Fe I	2.85	-0.82	68.4	19.7	18.0	—	45.0	34.5
4484.22	Fe I	3.60	-0.86	10.5	3.4	—	—	21.3	—
4489.74	Fe I	0.12	-3.97	64.8	—	19.2	77.9	69.6	60.7
4494.56	Fe I	2.20	-1.14	79.0	43.1	15.5	—	78.1	64.1
4528.61	Fe I	2.18	-0.82	100.1	—	38.1	—	—	74.5
4531.15	Fe I	1.49	-2.15	79.2	21.8	23.9	80.8	80.3	—
4592.65	Fe I	1.56	-2.45	57.3	7.0	16.4	54.3	54.0	41.2
4602.94	Fe I	1.49	-2.21	74.4	—	16.4	—	77.6	48.1
4632.91	Fe I	1.61	-2.91	27.2	4.1	8.2	19.7	28.5	12.8
4647.44	Fe I	2.95	-1.35	28.2	5.3	—	11.7	16.4	13.0
4678.85	Fe I	3.60	-0.83	21.7	—	—	—	21.4	—
4691.41	Fe I	2.99	-1.52	21.2	—	2.7	—	21.3	—
4707.27	Fe I	3.24	-1.08	30.9	—	5.4	19.5	20.9	9.5
4710.28	Fe I	3.02	-1.61	16.3	2.1	—	9.1	—	3.3
4733.59	Fe I	1.49	-2.99	—	4.4	—	16.2	23.8	22.0
4736.77	Fe I	3.21	-0.75	46.5	7.3	17.6	30.9	49.5	25.0
4786.81	Fe I	3.02	-1.61	13.8	—	—	—	15.8	—
4789.65	Fe I	3.55	-0.96	11.7	—	—	5.8	—	—
4859.74	Fe I	2.88	-0.76	—	—	41.5	48.4	64.2	39.7
4871.32	Fe I	2.87	-0.36	83.0	—	—	—	83.9	48.5
4872.14	Fe I	2.88	-0.57	74.3	—	—	55.2	68.3	51.8
4890.75	Fe I	2.88	-0.39	79.8	21.7	54.3	69.1	—	51.4
4891.49	Fe I	2.85	-0.11	93.2	44.3	53.8	66.6	92.1	69.2
4903.31	Fe I	2.88	-0.93	53.2	14.4	13.9	42.7	58.4	30.9
4918.99	Fe I	2.87	-0.34	81.0	48.3	—	55.6	80.5	62.2
4920.50	Fe I	2.83	0.07	—	68.4	—	91.6	—	79.4
4924.77	Fe I	2.28	-2.26	26.2	—	9.7	8.8	23.6	—
4938.81	Fe I	2.88	-1.08	42.1	—	9.3	—	43.0	27.9
4939.69	Fe I	0.86	-3.34	50.6	—	17.2	60.5	53.8	36.8
4966.09	Fe I	3.33	-0.87	34.0	—	6.4	25.5	32.4	25.6
4994.13	Fe I	0.92	-2.96	70.7	—	25.9	74.9	64.0	53.1
5006.12	Fe I	2.83	-0.61	72.2	24.5	—	61.5	73.0	50.5
5012.07	Fe I	0.86	-2.64	95.2	33.4	50.4	105.7	93.8	83.5
5014.94	Fe I	3.94	-0.30	27.0	—	—	10.3	20.6	11.6
5022.24	Fe I	3.98	-0.53	15.4	—	—	—	15.7	9.4
5028.13	Fe I	3.57	-1.12	9.2	—	—	—	16.4	6.0
5041.07	Fe I	0.96	-3.09	70.8	13.4	—	—	57.3	39.2
5041.76	Fe I	1.49	-2.20	79.6	20.8	31.3	70.1	79.3	63.1
5049.82	Fe I	2.28	-1.34	69.7	—	17.8	44.8	70.2	48.9
5051.63	Fe I	0.92	-2.80	79.1	—	42.3	91.4	82.9	64.8
5068.77	Fe I	2.94	-1.04	35.3	—	16.2	21.0	49.7	28.8
5074.75	Fe I	4.22	-0.20	25.3	—	7.6	—	—	—
5079.22	Fe I	2.20	-2.07	42.1	4.4	—	28.8	37.8	25.9
5079.74	Fe I	0.99	-3.22	62.7	—	20.4	55.5	—	39.1
5083.34	Fe I	0.96	-2.96	70.2	27.4	—	58.4	74.9	53.7
5090.77	Fe I	4.26	-0.40	8.0	—	2.3	—	10.7	7.4
5098.70	Fe I	2.18	-2.03	46.5	8.0	12.4	34.5	42.7	31.8
5123.72	Fe I	1.01	-3.07	66.6	—	—	—	—	53.7
5125.12	Fe I	4.22	-0.14	19.7	—	—	14.8	26.3	—
5127.36	Fe I	0.92	-3.31	59.0	14.8	—	42.8	65.1	43.3
5131.47	Fe I	2.22	-2.51	18.2	—	—	5.2	—	5.8

**Table 2.** Continued.

$\lambda$ (Å)	Species	$\chi$	$\log gf$	HD2796 eV	J1054+0528 mÅ	J1529+0804 mÅ	J1645+4357 mÅ	2114-0616 mÅ	J2216+2232 mÅ
5133.69	Fe I	4.18	0.14	36.7	—	6.5	25.8	46.1	—
5137.38	Fe I	4.18	-0.40	18.1	—	—	6.1	19.5	—
5141.74	Fe I	2.42	-1.96	—	—	—	—	18.9	15.0
5142.93	Fe I	0.96	-3.08	—	14.6	19.9	37.3	71.5	55.0
5150.84	Fe I	0.99	-3.07	61.2	13.6	—	52.0	61.9	41.1
5151.91	Fe I	1.01	-3.32	44.6	—	19.1	—	—	18.6
5162.27	Fe I	4.18	0.02	31.5	—	3.3	16.7	29.0	13.2
5166.28	Fe I	0.00	-4.20	73.1	24.5	29.8	71.4	67.8	43.8
5171.60	Fe I	1.49	-1.79	100.1	58.1	58.0	115.1	99.3	81.0
5191.46	Fe I	3.04	-0.55	60.6	16.5	27.6	44.8	72.1	43.0
5192.34	Fe I	3.00	-0.42	69.7	16.6	12.6	57.2	68.5	52.2
5194.94	Fe I	1.56	-2.09	83.8	25.1	51.4	85.5	80.1	44.5
5198.71	Fe I	2.22	-2.13	32.8	—	4.7	14.6	34.8	24.7
5202.34	Fe I	2.18	-1.84	56.5	11.2	11.8	49.8	52.3	22.9
5216.27	Fe I	1.61	-2.15	72.2	23.6	23.1	75.2	65.7	54.6
5217.39	Fe I	3.21	-1.07	23.4	—	—	5.3	20.2	9.2
5225.52	Fe I	0.11	-4.79	30.2	—	6.7	—	—	18.6
5232.94	Fe I	2.94	-0.06	91.9	45.6	46.7	—	84.8	68.8
5242.49	Fe I	3.63	-0.97	13.4	—	6.6	—	14.3	8.8
5247.05	Fe I	0.09	-4.95	23.6	—	—	—	—	11.9
5254.96	Fe I	0.11	-4.76	38.1	—	6.0	—	—	23.2
5263.31	Fe I	3.27	-0.88	29.6	—	5.1	10.7	32.0	14.4
5266.56	Fe I	3.00	-0.39	74.0	—	—	60.4	79.7	56.3
5269.54	Fe I	0.86	-1.32	155.8	—	113.7	—	148.6	131.1
5281.79	Fe I	3.04	-0.83	39.5	—	12.0	33.2	44.5	23.1
5283.63	Fe I	3.24	-0.52	45.8	—	13.5	43.2	55.8	27.9
5302.30	Fe I	3.28	-0.72	34.0	—	—	24.3	45.6	25.1
5307.36	Fe I	1.61	-2.99	26.8	—	7.2	21.1	30.2	17.3
5324.18	Fe I	3.21	-0.10	67.3	27.6	—	—	75.3	52.0
5328.04	Fe I	0.92	-1.47	146.8	—	121.6	—	140.1	118.5
5455.61	Fe I	1.01	-2.10	—	67.3	80.1	136.8	—	79.3
5497.52	Fe I	1.01	-2.85	82.6	—	39.6	86.4	—	67.6
5501.46	Fe I	0.96	-3.05	74.1	—	—	—	75.0	59.0
5506.78	Fe I	0.99	-2.80	81.4	22.2	54.0	87.5	87.1	58.5
5569.62	Fe I	3.42	-0.54	37.1	—	7.4	33.5	48.0	16.6
5572.84	Fe I	3.40	-0.28	50.6	—	16.0	25.2	60.1	27.7
5586.75	Fe I	3.37	-0.10	63.8	17.1	—	41.0	61.6	—
5615.64	Fe I	3.33	0.05	69.4	25.6	37.4	70.2	77.6	46.9
5624.54	Fe I	3.42	-0.75	27.3	—	13.0	19.2	21.7	14.7
5658.82	Fe I	3.40	-0.79	26.8	—	8.7	11.1	29.2	16.9
5701.54	Fe I	2.56	-2.22	17.4	—	4.3	—	19.2	9.7
5753.12	Fe I	4.26	-0.69	4.2	—	—	1.3	—	—
6137.69	Fe I	2.59	-1.40	51.9	18.5	—	35.4	53.0	39.1
6191.56	Fe I	2.43	-1.42	58.6	18.9	11.0	57.3	57.3	36.4
6213.43	Fe I	2.22	-2.48	—	—	—	19.5	21.4	—
6219.28	Fe I	2.20	-2.43	21.4	—	6.5	20.7	31.1	17.6
6230.72	Fe I	2.56	-1.28	58.8	14.7	11.1	55.0	—	48.4
6246.32	Fe I	3.60	-0.73	18.9	—	2.1	—	24.1	6.6
6252.56	Fe I	2.40	-1.77	49.7	7.9	—	42.7	38.8	35.1
6254.26	Fe I	2.28	-2.44	23.9	—	—	—	20.4	13.6
6265.13	Fe I	2.18	-2.54	20.8	—	4.2	16.6	25.0	12.4
6335.33	Fe I	2.20	-2.18	32.9	—	3.8	29.9	34.6	21.9
6336.83	Fe I	3.69	-1.05	17.5	1.3	—	9.5	9.6	5.2

**Table 2.** Continued.

$\lambda$ (Å)	Species	$\chi$ eV	$\log gf$	HD2796 mÅ	J1054+0528 mÅ	J1529+0804 mÅ	J1645+4357 mÅ	2114-0616 mÅ	J2216+2232 mÅ
6355.03	Fe I	2.85	-2.37	6.7	—	—	4.8	—	—
6393.60	Fe I	2.43	-1.43	53.9	—	—	46.7	45.2	37.1
6411.65	Fe I	3.65	-0.60	25.2	—	13.8	6.2	35.4	16.1
6421.35	Fe I	2.28	-2.03	42.1	10.9	11.4	—	44.4	26.9
6430.85	Fe I	2.18	-2.01	49.4	—	4.8	—	50.7	48.5
6494.98	Fe I	2.40	-1.24	78.4	34.2	41.6	87.1	74.6	56.4
6592.91	Fe I	2.73	-1.47	34.1	—	9.6	30.9	43.0	28.7
6593.87	Fe I	2.43	-2.42	17.3	3.7	3.5	14.8	18.4	—
6663.44	Fe I	2.42	-2.48	19.0	—	3.1	—	17.8	6.1
6677.99	Fe I	2.69	-1.47	48.0	10.3	15.0	37.0	43.2	33.9
4178.86	Fe II	2.58	-2.51	67.2	—	21.5	31.2	—	29.8
4233.17	Fe II	2.58	-1.97	90.0	37.2	—	65.1	93.2	49.9
4515.34	Fe II	2.84	-2.60	53.4	11.4	7.0	22.0	48.9	29.8
4520.22	Fe II	2.81	-2.65	—	—	5.8	17.0	47.2	—
4522.63	Fe II	2.84	-2.25	72.2	11.4	24.8	—	79.9	36.2
4555.89	Fe II	2.83	-2.40	59.3	—	—	42.9	46.1	40.0
4583.84	Fe II	2.81	-1.93	86.3	—	—	56.2	85.3	58.9
4731.44	Fe II	2.89	-3.36	19.3	—	—	—	—	—
4923.93	Fe II	2.89	-1.26	111.7	59.5	57.0	—	105.2	81.6
5018.45	Fe II	2.89	-1.10	123.4	—	61.6	119.3	111.9	90.1
5234.63	Fe II	3.22	-2.18	53.5	10.9	16.0	41.9	47.1	32.8
5276.00	Fe II	3.20	-2.01	57.8	11.7	9.9	47.3	—	29.9
5534.83	Fe II	3.24	-2.93	21.9	4.0	—	—	24.7	—
6247.54	Fe II	3.89	-2.51	13.9	—	—	—	14.4	—
6432.68	Fe II	2.89	-3.55	9.8	—	—	—	13.0	—
4092.39	Co I	0.92	-1.11	—	3.2	15.1	19.2	—	30.6
4118.77	Co I	1.05	-0.48	—	16.6	39.2	—	53.0	44.5
4121.31	Co I	0.92	-0.33	—	—	63.0	—	71.1	60.3
4604.99	Ni I	3.48	-0.29	—	—	—	14.5	9.4	—
4648.66	Ni I	3.42	-0.16	—	—	1.8	—	15.8	10.9
4714.42	Ni I	3.38	0.25	—	7.5	7.4	29.3	33.2	12.8
4829.03	Ni I	3.54	-0.33	—	—	—	—	—	4.0
4831.18	Ni I	3.61	-0.42	—	—	6.5	—	8.8	—
4855.41	Ni I	3.54	0.00	—	—	9.7	—	18.2	6.3
4904.41	Ni I	3.54	-0.17	—	—	—	11.7	13.4	7.0
4980.16	Ni I	3.61	-0.11	—	3.4	—	7.2	14.8	8.5
5035.37	Ni I	3.63	0.29	—	—	12.8	15.9	18.0	10.4
5137.08	Ni I	1.68	-1.99	—	5.6	22.0	30.3	27.6	—
5476.90	Ni I	1.83	-0.78	—	29.8	19.8	83.8	76.4	64.9
6643.63	Ni I	1.68	-2.22	—	—	—	19.4	16.7	13.8
4722.15	Zn I	4.03	-0.39	21.2	—	6.8	—	24.4	9.5
4810.53	Zn I	4.08	-0.17	26.6	—	—	—	24.4	12.0
4077.71	Sr II	0.00	0.15	149.1	102.1	3.4	—	—	106.7
4854.86	Y II	0.99	-0.38	13.1	—	—	—	28.5	6.6
4883.69	Y II	1.08	0.07	26.8	11.3	4.6	—	—	—
4900.11	Y II	1.03	-0.09	26.2	—	6.7	—	40.2	14.4
4161.21	Zr II	0.71	-0.59	29.7	—	—	—	53.3	9.1
4554.04	Ba II	0.00	0.17	131.9	—	30.4	—	192.3	78.1
4934.09	Ba II	0.00	-0.16	—	36.5	25.1	47.3	190.4	—
6141.73	Ba II	0.70	-0.07	78.3	17.3	—	23.0	155.0	26.1
6496.91	Ba II	0.60	-0.41	79.2	10.3	—	17.1	—	40.9
4086.71	La II	0.00	-0.07	15.3	—	—	—	—	—
4196.55	La II	0.32	-0.30	—	26.7	2.3	—	52.8	—

**Table 2.** Continued.

$\lambda$ (Å)	Species	$\chi$	$\log gf$	HD2796	J1054+0528	J1529+0804	J1645+4357	2114–0616	J2216+2232
		eV		mÅ	mÅ	mÅ	mÅ	mÅ	mÅ
4920.98	La II	0.13	-0.58	5.7	—	—	1.4	54.4	—
4073.47	Ce II	0.48	0.21	—	—	5.8	—	33.5	—
4137.64	Ce II	0.52	0.40	6.9	7.2	7.9	—	—	—
4562.36	Ce II	0.48	0.21	5.5	—	—	—	44.8	—
4628.16	Ce II	0.52	0.14	6.5	8.5	—	—	44.6	—
4143.12	Pr II	0.37	0.61	—	—	17.9	—	—	—
4179.40	Pr II	0.20	0.48	17.5	—	—	—	49.5	—
4023.00	Nd II	0.56	0.04	—	—	—	—	—	4.4
4061.08	Nd II	0.47	0.55	13.8	8.6	8.2	—	—	7.5
4109.07	Nd II	0.06	-0.16	17.2	9.2	—	—	47.3	7.2
4109.45	Nd II	0.32	0.35	14.0	19.8	—	—	74.8	5.3
4156.08	Nd II	0.18	0.16	6.3	22.0	—	—	79.6	—
4177.33	Nd II	0.06	-0.10	—	8.0	3.1	—	53.9	—
4462.98	Nd II	0.56	0.04	—	4.0	7.8	—	46.3	—
4706.54	Nd II	0.00	-0.71	3.6	2.6	—	—	28.4	—
5255.51	Nd II	0.20	-0.67	4.0	4.6	—	—	34.4	1.1
5319.82	Nd II	0.55	-0.14	1.6	5.9	—	—	45.8	—
4434.32	Sm II	0.38	-0.07	—	—	18.3	—	46.8	—
4519.63	Sm II	0.54	-0.35	—	—	6.3	—	—	—
4129.72	Eu II	0.00	0.22	22.2	6.7	—	—	63.8	4.1

**Table 3.** Stellar Parameters of the Program Stars.

ID	Lick/APF (adopted)				LAMOST			Gaia DR2		Photometry	Luminosity
	$T_{\text{eff}}$ (K)	$\log g$ (cgs)	[Fe/H]	$\xi$ ( $\text{km s}^{-1}$ )	$T_{\text{eff}}$ (K)	$\log g$ (cgs)	[Fe/H]	$T_{\text{eff}}$ (K)	$\log g$ (cgs)	$T_{\text{eff}}$ (K)	$L_*/L_{\odot}$ ( $\text{erg s}^{-1}$ )
	HD2796	4869	1.04	-2.51	2.01	...	...	...	4995	2.15	...
J1054+0528	5030	1.88	-3.30	1.94	5094	1.76	-3.23	5080	1.89	4981	166.94
J1529+0804	5085	2.00	-3.18	2.34	5026	1.54	-3.27	5041	1.90	4913	132.27
J1645+4357	4810	1.39	-2.97	2.93	4715	2.14	-3.05	4886	1.39	4652	431.38
J2114–0616	4999	1.48	-2.43	2.11	4377	1.55	-2.95	4870	1.66	4831	409.09
J2216+2232	4842	1.40	-2.91	1.79	4902	2.65	-3.13	5018	2.05	4815	432.89

NOTE—The tenth column was measured using parallaxes adopted from Gaia DR2 and stellar mass of  $\sim 0.8 M_{\odot}$

**Table 4.** LTE Abundances of Individual Elements for the Program Stars.

	HD2796				J1054+0528				J1529+0804			
	$\log \epsilon(X)$	[X/Fe]	$\sigma$	$N$	$\log \epsilon(X)$	[X/Fe]	$\sigma$	$N$	$\log \epsilon(X)$	[X/Fe]	$\sigma$	$N$
Li I	...	...	...	...	...	...	...	...	...	...	...	...
C(CH)	5.60	-0.31	0.05	5	5.95	0.82	0.09	6	6.05	0.80	0.11	4
(CH) <sub>corr</sub>	...	0.74	...	...	...	0.04	...	...	...	0.01	...	...
N(CN)	...	...	...	...	...	...	...	...	...	...	...	...
Na I	4.40	0.67	0.05	2	3.25	0.31	0.05	2	2.76	-0.30	0.24	2
Mg I	5.68	0.59	0.05	4	4.71	0.41	0.12	5	4.64	0.22	0.10	4
Ca I	4.15	0.32	0.10	21	3.39	0.35	0.29	11	3.46	0.30	0.18	17
Sc II	0.55	-0.09	0.05	13	-0.12	0.03	0.24	6	-0.10	-0.07	0.05	3
Ti I	2.64	0.20	0.09	18	2.08	0.43	0.25	13	1.87	0.10	0.30	11
Ti II	2.67	0.23	0.12	33	1.84	0.19	0.30	25	1.95	0.18	0.32	24
V I	1.36	-0.06	0.11	1	0.93	0.30	0.13	1	...	...	...	...
Cr I	2.97	-0.16	0.10	9	2.34	0.00	0.30	5	2.27	-0.19	0.29	8
Mn I	2.57	-0.35	0.12	3	1.67	-0.46	0.10	1	2.68	0.43	0.02	2
Fe I	4.99	0.00	0.12	217	4.20	0.00	0.16	84	4.32	0.00	0.26	146
Fe II	4.99	0.00	0.09	24	4.20	0.00	0.18	8	4.32	0.00	0.25	17
Co I	...	...	...	...	1.61	-0.08	0.20	2	2.29	0.48	0.06	3
Ni I	...	...	...	...	3.10	0.18	0.13	4	3.66	0.62	0.32	7
Zn I	2.33	0.28	0.03	2	...	...	...	...	1.95	0.57	0.12	1
Sr II	-0.01	-0.37	0.10	1	-0.73	-0.30	0.13	1	...	...	...	...
Y II	-0.66	-0.36	0.06	3	-0.81	0.28	0.16	1	-1.04	-0.07	0.19	2
Zr II	0.19	0.12	0.12	1	...	...	...	...	...	...	...	...
Ba II	-0.57	-0.24	0.22	3	-1.64	-0.52	0.10	3	-2.01	-1.01	0.13	2
La II	-1.69	-0.28	0.04	2	...	...	...	...	-1.63	0.45	0.13	1
Ce II	-1.18	-0.25	0.10	3	-0.74	0.98	0.20	2	-0.77	0.84	0.11	2
Pr II	-1.36	0.43	0.17	1	...	...	...	...	-0.88	1.58	0.19	1
Nd II	-1.34	-0.25	0.26	7	-0.91	0.97	0.19	9	-0.71	1.05	0.58	5
Sm II	...	...	...	...	...	...	...	...	-0.60	1.62	0.05	2
Eu II	-2.07	-0.08	0.11	1	-2.34	0.44	0.14	1	...	...	...	...

**Table 4.** Continued.

J1645+4357					J2114–0616					J2216+2232					Sun	
	$\log \epsilon(X)$	[X/Fe]	$\sigma$	N	$\log \epsilon(X)$	[X/Fe]	$\sigma$	N	$\log \epsilon(X)$	[X/Fe]	$\sigma$	N	$\log \epsilon(X)$			
Li I	...	...	...	...	...	...	...	...	0.96	2.82	0.04	1	1.05			
C(CH)	6.16	0.70	0.04	6	7.37	1.37	0.05	10	6.14	0.62	0.05	8	8.43			
(CH) <sub>corr</sub>	...	0.45	...	...	...	0.17	...	...	...	0.45	...	...	...	...		
N(CN)	...	...	...	...	7.28	1.88	0.17	2	...	...	...	...	7.83			
Na I	3.45	0.18	0.04	2	4.69	0.88	0.05	2	3.68	0.35	0.05	2	6.24			
Mg I	5.12	0.49	0.05	4	5.69	0.52	0.12	5	5.34	0.65	0.02	4	7.60			
Ca I	3.44	0.07	0.28	11	4.17	0.26	0.29	20	3.70	0.27	0.17	18	6.34			
Sc II	-0.48	-0.66	0.23	4	0.75	0.04	0.25	13	0.22	-0.02	0.14	8	3.15			
Ti I	1.88	-0.10	0.26	11	2.78	0.26	0.16	15	2.26	0.22	0.13	15	4.95			
Ti II	1.76	-0.21	0.25	25	2.65	0.13	0.31	30	2.05	0.01	0.27	26	4.95			
V I	...	...	...	...	...	...	...	...	...	...	...	...	3.93			
Cr I	2.24	-0.43	0.30	6	3.13	-0.08	0.09	8	2.35	-0.38	0.22	10	5.64			
Mn I	2.58	0.12	0.08	2	2.49	-0.51	0.03	2	2.24	-0.28	0.21	2	5.43			
Fe I	4.53	0.00	0.22	150	5.07	0.00	0.14	156	4.58	0.00	0.18	181	7.50			
Fe II	4.53	0.00	0.20	18	5.07	0.00	0.17	24	4.58	0.00	0.19	20	7.50			
Co I	2.04	0.02	0.09	1	2.51	-0.05	0.03	2	2.27	0.19	0.11	3	4.99			
Ni I	3.60	0.35	0.16	8	3.85	0.06	0.10	11	3.40	0.09	0.15	9	6.22			
Zn I	...	...	...	...	2.43	0.30	0.12	2	1.92	0.27	0.04	2	4.56			
Sr II	...	...	...	...	...	...	...	...	-0.66	-0.62	0.08	1	2.87			
Y II	...	...	...	...	-0.12	0.10	0.03	2	-0.89	-0.19	0.09	2	2.21			
Zr II	...	...	...	...	0.79	0.64	0.13	1	-0.37	-0.04	0.10	1	2.58			
Ba II	-1.80	-1.01	0.15	3	0.75	1.00	0.11	3	-1.35	-0.62	0.25	3	2.18			
La II	-2.25	-0.38	0.11	1	-0.17	1.16	0.02	2	...	...	...	...	1.10			
Ce II	...	...	...	...	0.08	0.93	0.12	3	...	...	...	...	1.58			
Pr II	...	...	...	...	-0.49	1.22	0.15	1	...	...	...	...	0.72			
Nd II	...	...	...	...	0.10	1.11	0.17	8	-1.46	0.03	0.22	5	1.42			
Sm II	...	...	...	...	-0.18	1.29	0.12	1	...	...	...	...	0.96			
Eu II	...	...	...	...	-1.07	0.84	0.13	1	-2.84	-0.44	0.12	1	1.07			

NOTE—N refers to the number of lines adopted for determination of the elemental abundances.

**Table 5.** Li, Na, Mg NLTE abundances

Star	log $\epsilon$ (Li)		log $\epsilon$ (Na)		[Na/Fe] <sub>NLTE</sub>		log $\epsilon$ (Mg)		[Mg/Fe] <sub>NLTE</sub>	
	LTE	NLTE	LTE	NLTE	LTE	NLTE	LTE	NLTE	LTE	NLTE
HD2796	< 0.14	< 0.15	4.40	3.65	-0.08	5.68	5.69	0.60		
J1054+0528	...	...	3.25	2.91	-0.03	4.71	4.81	0.51		
J1529+0804	< 0.30	< 0.32	2.76	2.53	-0.53	4.64	4.75	0.33		
J1645+4357	< 0.24	< 0.26	3.45	2.97	-0.30	5.12	5.10	0.47		
J2114–0616	< 0.44	< 0.44	4.69	3.88	0.07	5.69	5.69	0.52		
J2216+2232	0.95	0.96	3.68	3.06	-0.27	5.34	5.33	0.64		

NOTE—J1054+0528 has defect in the spectrum at the region of the Li I line.

**Table 6.** Uncertainties of  $\log \epsilon(X)$  Propagated from the Stellar Parameters, Computed for HD2796 as an Example.

Ion	$\Delta\text{Teff}$	$\Delta\log g$	$\Delta\xi$
	+ 150 K	+ 0.3 dex	+ 0.3 km s <sup>-1</sup>
CH(C)	0.32	-0.12	0.02
CN(N)	0.50	-0.10	0.01
Na I	0.16	-0.05	-0.03
Mg I	0.14	-0.11	-0.03
Ca I	0.05	-0.02	-0.11
Sc II	0.09	-0.12	-0.13
Ti I	-0.03	0.00	-0.02
Ti II	0.11	-0.12	-0.13
V II	-0.04	0.00	-0.02
Cr II	-0.02	-0.01	-0.01
Mn I	0.01	-0.01	-0.08
Fe I	0.16	-0.03	-0.15
Fe II	0.15	-0.13	-0.219
Co I	-0.04	0.01	0.03
Ni I	-0.01	-0.05	-0.13
Zn I	0.06	-0.06	-0.18
Sr II	0.06	-0.07	0.08
Y II	0.07	-0.13	-0.17
Zr I	0.07	-0.12	-0.16
Ba II	0.02	-0.12	0.08
La II	0.04	-0.12	-0.14
Ce II	0.05	-0.12	-0.15
Pr II	0.03	-0.12	-0.13
Nd II	0.03	-0.12	-0.13
Eu II	0.05	-0.12	-0.14

**Table 7.** Parallaxes, Proper Motions and Distances

Star	<i>Gaia</i> DR2 source ID	$\varpi$	error	pmra	error	pmdec	error	Distance	d1	d2
		(mas)		(mas yr $^{-1}$ )		(mas yr $^{-1}$ )		(kpc)		
HD2796	2367454697327877504	1.4859	0.0626	-1.375	0.164	-51.052	0.084	0.661	0.027	0.028
J1054+0528	3864140775805950208	0.2149	0.0393	-8.678	0.073	-4.183	0.055	3.548	0.404	0.502
J1529+0804	1164484488577137792	0.2365	0.0362	-2.401	0.056	-9.169	0.05	3.628	0.425	0.544
J1645+4357	1357725650023190784	0.0454	0.0207	0.327	0.033	-5.663	0.042	8.355	0.996	1.215
J2114-0616	6910940758263238912	0.4496	0.0373	-20.444	0.067	-6.376	0.068	2.082	0.153	0.178
J2216+2232	1878089211702170880	0.3721	0.0384	-4.454	0.056	-1.477	0.058	2.440	0.211	0.253

NOTE—The d1 and d2 columns indicate the 16th percentile and 84th percentile confidence intervals.

**Table 8.** Kinematics parameters

Star ID	$V_R$	$V_\Phi$	$V_Z$	$V_\perp$	$Z_{max}$	$R_{apo}$	$R_{peri}$	e	E	$L_z$
HD2796	-95.03	89.62	37.81	102.28	1.02	9.59	2.28	0.62	-1.45	763.40
J1054+0528	82.98	108.74	-15.88	84.49	3.59	10.81	3.60	0.50	-1.35	1036.00
J1529+0804	-86.75	101.22	-8.18	87.13	3.01	7.43	2.52	0.50	-1.52	624.00
J1645+4357	-74.40	210.51	-58.18	94.45	7.67	14.50	7.82	0.30	-1.15	1807.00
J2114-0616	-220.45	314.95	37.41	223.60	4.70	33.16	5.64	0.71	-0.85	2323.00
J2216+2232	-35.03	-56.42	182.30	185.64	8.70	9.22	4.08	0.41	-1.35	-478.40

**Table 1.** Log of the Lick/APP Observations

	ID	Date	RA	DEC	<i>r</i>	Exptime	S/N	<i>V<sub>r</sub></i>
					(mag)	(s)	(pixel <sup>-1</sup> )	(km s <sup>-1</sup> )
1	J0326+0202	18 Nov 2015	03 26 53.88	+02 02 28.1	11.55	1800*4	45	116.2
2	J1108+2530	16 Mar 2015	11 08 47.18	+25 30 47.2	12.16	1800*4	32	-114.62
3	J1256+3440	30 May 2015	12 56 42.41	+34 40 58.9	12.64	1800*4	30	284.06
4	J1413+1727	24 Jun 2015	14 13 15.67	+17 27 20.8	11.85	1800*4	42	106.18
5	J1630+0953	23 Jun 2015	16 30 35.82	+09 53 17.0	12.98	1800*4	30	57.82
6	J2216+0246	24 Jun 2015	22 16 35.96	+02 46 17.0	12.47	1800*4	32	-94.88

NOTE—The S/N ratio per pixel was measured using IRAF at  $\lambda \sim 4500 \text{ \AA}$ .

**Table 2.** Equivalent Widths of Our Sample.

$\lambda$	Species	$\chi$	$\log gf$	J0326+0202	J1108+2530	J1256+3440	J1413+1727	J1630+0953	J2216+0246
(Å)		eV		mÅ	mÅ	mÅ	mÅ	mÅ	mÅ
4312	C(CH)	—	—	syn	syn	syn	syn	syn	syn
4323	C(CH)	—	—	syn	syn	syn	syn	syn	syn
4214	N(CN)	—	—	syn	syn	syn	syn	syn	syn
5889.95	Na I	0.00	0.10	99.5	132.5	146.6	158.0	144.0	142.3
5895.92	Na I	0.00	-0.20	122.0	115.2	58.3	125.0	136.3	110.4
4057.50	Mg I	4.35	-0.89	45.9	31.6	24.0	—	—	26.0
4167.27	Mg I	4.35	-0.71	32.7	31.5	45.4	—	33.3	59.0
4571.10	Mg I	0.00	-5.69	22.4	46.3	—	34.3	55.8	68.6
4702.99	Mg I	4.33	-0.44	44.5	57.2	24.1	53.7	73.4	76.7
5172.68	Mg I	2.71	-0.45	—	—	—	168.1	—	—
5183.60	Mg I	2.72	-0.24	—	—	—	178.8	—	—
5528.40	Mg I	4.35	-0.50	42.7	60.2	41.3	48.3	58.9	88.4
4283.01	Ca I	1.89	-0.22	—	28.3	27.0	40.6	34.6	62.2
4318.65	Ca I	1.89	-0.21	—	38.7	40.2	39.1	47.9	50.4
4425.44	Ca I	1.88	-0.36	14.2	26.6	32.9	35.7	26.9	28.5
4454.78	Ca I	1.90	0.26	50.4	51.6	23.2	60.7	42.5	70.0
4455.89	Ca I	1.90	-0.53	17.1	30.3	—	—	15.4	27.3
5261.71	Ca I	2.52	-0.58	2.7	—	—	9.1	8.5	—
5265.56	Ca I	2.52	-0.11	7.5	21.1	—	17.1	17.8	17.5
5512.98	Ca I	2.93	-0.45	2.4	3.4	—	1.8	—	—
5581.97	Ca I	2.52	-0.56	2.0	9.0	—	5.4	10.8	16.1
5588.76	Ca I	2.53	0.36	—	40.2	—	32.5	31.8	50.7
5590.12	Ca I	2.52	-0.57	3.8	7.9	—	7.5	2.3	16.5
5594.47	Ca I	2.52	0.10	15.0	23.5	—	1.1	29.4	54.5

NOTE—(This table is available in machine-readable form.)

**Table 3.** Stellar Parameters of the Program Stars.

ID	Lick/APF (corrected & adopted)				Lick/APF (spectroscopic)				Photometry		Gaia DR2
	$T_{\text{eff}}$	$\log g$	[Fe/H]	$\xi$	$T_{\text{eff}}$	$\log g$	[Fe/H]	$\xi$	$T_{\text{eff}}(\text{V-J})$	$T_{\text{eff}}(\text{V-K})$	$\log g$
	(K)	(cgs)		( $\text{km s}^{-1}$ )	(K)	(cgs)		( $\text{km s}^{-1}$ )	(K)	(K)	(cgs)
J0326+0202	5080	2.03	-3.11	2.01	4900	1.59	-3.26	1.92	5083	5187	2.06
J1108+2530	5003	2.05	-2.72	1.08	4815	1.52	-2.89	1.09	5136	5141	2.15
J1256+3440	5215	1.74	-2.76	2.37	5050	1.36	-2.89	2.30	5074	5142	1.87
J1413+1727	4914	1.25	-3.00	1.92	4716	0.72	-3.20	2.02	4709	4704	1.23
J1630+0953	4783	1.02	-2.94	2.14	4570	0.40	-3.04	2.28	4693	4723	1.30
J2216+0246	4945	1.53	-2.52	1.68	4750	1.05	-2.67	1.67	4899	4936	1.87

**Table 4.** LTE Abundances of Individual Elements for the Program Stars

	J0326+0202				J1108+2530				J1256+3440			
	log $\epsilon$ (X)	[X/Fe]	$\sigma$	N	log $\epsilon$ (X)	[X/Fe]	$\sigma$	N	log $\epsilon$ (X)	[X/Fe]	$\sigma$	N
C(CH)	5.56	0.24	0.04	2	5.99	0.28	0.05	2	6.04	0.37	0.05	2
(CH) <sub>corr</sub>	...	0.02	...	...	...	0.04	...	...	...	0.24	...	...
(CH) <sub>natal</sub>	...	0.26	...	...	...	0.32	...	...	...	0.61	...	...
N(CN)	...	...	...	...	...	...	...	...	...	...	...	...
Na I	3.43	0.30	0.18	3	3.54	0.02	0.03	2	3.64	0.19	0.14	2
Mg I	5.11	0.62	0.16	5	5.26	0.38	0.16	6	5.09	0.28	0.12	4
Ca I	3.52	0.29	0.14	18	3.81	0.19	0.13	20	3.77	0.19	0.11	11
Sc II	0.26	0.22	0.13	6	0.36	-0.07	0.11	13	0.34	-0.05	0.18	9
Ti I	2.24	0.40	0.09	15	2.32	0.09	0.12	19	2.51	0.32	0.19	13
Ti II	2.06	0.22	0.11	28	2.06	-0.17	0.17	33	2.25	0.06	0.15	27
V I	0.71	-0.11	0.12	1	0.67	-0.54	0.11	1	1.01	-0.16	0.10	1
Cr I	2.51	-0.02	0.08	7	2.49	-0.43	0.16	12	2.63	-0.25	0.16	7
Mn I	2.07	-0.25	0.12	2	2.23	-0.48	0.11	3	2.32	-0.35	0.12	1
Fe I	4.39	0.00	0.16	118	4.78	-0.00	0.12	131	4.74	0.00	0.16	123
Fe II	4.38	-0.01	0.18	13	4.77	-0.01	0.12	20	4.74	0.00	0.15	14
Co I	2.41	0.53	0.12	2	2.14	-0.13	0.15	3	2.38	0.15	0.10	1
Ni I	3.38	0.27	0.18	7	3.46	-0.04	0.17	12	3.70	0.24	0.19	6
Zn I	1.77	0.32	0.13	1	1.75	-0.09	0.17	2	2.12	0.32	0.11	1
Sr II	-0.65	-0.41	0.11	1	-0.06	-0.21	0.19	1	-0.46	-0.57	0.11	1
Y II	-1.00	-0.10	0.08	1	-1.14	-0.63	0.11	3	-1.05	-0.50	0.12	1
Zr II	-0.36	0.17	0.15	1	-0.78	-0.64	0.14	4	...	...	...	...
Ba II	-1.48	-0.55	0.18	2	-0.76	-0.22	0.13	2	-1.25	-0.67	0.19	3
La II	...	...	...	...	-1.13	0.01	0.22	2	-1.01	0.65	0.20	2
Ce II	-1.88	-0.35	0.13	1	-2.10	-0.10	0.20	1	-1.57	-0.39	0.22	2
Nd II	-1.47	0.22	0.15	1	...	...	...	...	-1.13	0.21	0.15	2
Sm II	...	...	...	...	-1.25	0.50	0.19	3	-1.79	0.01	0.14	1
Eu II	< -2.60	-0.01	0.13	1	-2.35	-0.15	0.11	1	< -2.10	0.14	0.14	1

**Table 4.** Continued.

J1413+1727				J1630+0953				J2216+0246				
	$\log \epsilon(X)$	[X/Fe]	$\sigma$	$N$	$\log \epsilon(X)$	[X/Fe]	$\sigma$	$N$	$\log \epsilon(X)$	[X/Fe]	$\sigma$	$N$
C(CH)	5.14	-0.29	0.07	2	6.13	0.64	0.05	2	6.19	0.28	0.09	2
(CH) <sub>corr</sub>	...	0.65	...	...	...	0.62	...	...	...	0.42	...	...
(CH) <sub>natal</sub>	...	0.36	...	...	...	1.26	...	...	...	0.70	...	...
N(CN)	...	...	...	...	5.77	0.88	0.17	1	...	...	...	...
Na I	3.58	0.34	0.13	3	3.50	0.20	0.11	2	3.76	0.04	0.15	3
Mg I	4.96	0.36	0.16	2	5.22	0.56	0.12	5	5.50	0.42	0.12	6
Ca I	3.69	0.35	0.18	11	3.61	0.21	0.19	18	4.08	0.26	0.12	17
Sc II	0.30	0.15	0.17	7	0.20	-0.01	0.13	10	0.59	-0.05	0.18	9
Ti I	2.27	0.32	0.11	9	2.22	0.21	0.17	14	2.66	0.23	0.12	14
Ti II	2.25	0.30	0.12	14	2.23	0.22	0.13	28	2.34	-0.09	0.13	32
V I	0.88	-0.05	0.16	1	1.10	0.11	0.15	1	0.89	-0.53	0.15	1
Cr I	2.76	0.12	0.11	6	2.67	-0.01	0.16	8	3.01	-0.11	0.17	7
Mn I	2.33	-0.10	0.10	1	2.23	-0.26	0.16	1	2.47	-0.44	0.13	2
Fe I	4.50	0.00	0.19	119	4.56	-0.00	0.15	127	4.97	-0.01	0.15	139
Fe II	4.50	0.00	0.17	11	4.56	-0.00	0.17	12	4.98	-0.01	0.19	14
Co I	2.22	0.23	0.11	2	2.61	0.56	0.12	1	2.42	-0.05	0.19	2
Ni I	3.20	-0.02	0.17	7	3.34	0.06	0.18	9	3.63	-0.07	0.17	10
Zn I	1.88	0.32	0.13	1	2.04	0.42	0.13	1	2.25	0.21	0.19	1
Sr II	-0.06	-0.07	0.20	1	-0.73	-0.66	0.12	1	-0.29	-0.64	0.17	1
Y II	-1.50	-0.38	0.19	1	-1.25	-0.52	0.14	1	-0.44	-0.13	0.13	2
Zr II	...	...	...	...	-0.32	0.04	0.16	1	-0.26	-0.32	0.16	1
Ba II	-1.09	-0.27	0.19	3	-0.95	-0.19	0.19	3	-0.43	-0.09	0.22	3
La II	...	...	...	...	-1.99	-0.15	0.14	1	-1.04	0.39	0.16	2
Ce II	-1.62	0.13	0.20	3	-1.40	-0.04	0.19	1	-0.97	-0.03	0.20	1
Nd II	-1.41	0.50	0.19	9	-1.45	0.07	0.28	2	-1.58	-0.48	0.17	4
Sm II	-2.00	0.37	0.26	2	-1.81	0.17	0.15	1	...	...	...	...
Eu II	< -2.35	0.13	0.16	1	< -2.35	0.07	0.15	1	< -2.00	0.00	0.19	1

NOTE—N refers to the number of lines adopted for determination of the elemental abundances.

**Table 5.** Estimated Abundance Uncertainties in the Element Abundance Ratios [X/Fe] for J1630+0953. The Other Sample Stars Yield Quite Similar Results.

Element	Ion	Random error	$\Delta T_{\text{eff}}$	$\Delta \log g$	$\Delta v_{\text{micr}}$	Root Mean
			+100 K	+0.3 dex	+0.3 km s $^{-1}$	Square
C	CH	0.05	0.19	0.11	0.00	0.23
N	NH	0.17	0.22	0.11	0.00	0.30
Na	1	0.11	0.09	-0.01	-0.02	0.14
Mg	1	0.12	0.09	-0.06	0.06	0.17
Ca	1	0.19	0.08	-0.01	-0.03	0.21
Sc	2	0.13	0.07	0.11	-0.02	0.19
Ti	1	0.17	0.10	-0.01	-0.01	0.19
Ti	2	0.13	0.04	0.08	-0.12	0.19
V	2	0.15	0.05	0.10	0.00	0.19
Cr	1	0.16	0.12	-0.01	-0.03	0.20
Mn	1	0.15	0.12	0.00	-0.01	0.19
Fe	1	0.17	0.12	-0.02	-0.08	0.18
Fe	2	0.12	0.02	0.11	-0.01	0.16
Co	1	0.12	0.12	0.00	-0.03	0.17
Ni	1	0.18	0.15	-0.03	-0.01	0.20

NOTE—Random errors represent the standard error of the mean and the last column represent the root mean squares of these errors.

**Table 6.** Parallaxes, Proper Motions and Distances

Star	<i>Gaia</i> DR2 source ID	$\varpi$	error	pmra	error	pmdec	error	Distance	d1	d2
				(mas)	(mas yr $^{-1}$ )	(mas yr $^{-1}$ )	(mas yr $^{-1}$ )			
J0326+0202	3268028903151246720	0.5421	0.0392	22.759	0.074	-14.128	0.062	1.727	1.617	1.853
J1108+2530	3995801795674031616	0.4887	0.0423	0.553	0.089	-38.926	0.062	1.893	1.753	2.057
J1256+3440	1515900293283319168	0.1945	0.0469	4.068	0.058	-13.785	0.048	3.601	3.134	4.194
J1413+1727	1233499867083517952	0.1525	0.0488	-6.039	0.089	-10.405	0.095	4.240	3.590	5.100
J1630+0953	4458577516730343424	0.1170	0.0261	-8.735	0.033	-8.939	0.023	6.183	5.354	7.267
J2216+0246	2682719929806900096	0.2893	0.0530	8.700	0.090	-11.429	0.100	2.899	2.521	3.391

NOTE—The d1 and d2 columns indicate the 16th percentile and 84th percentile confidence intervals.

**Table 7.** Positions and Galactic Space-velocity Components.

Star	X	Y	Z	U	V	W	$V_R$	$V_\phi$	$V_\perp$
							(km s $^{-1}$ )	(km s $^{-1}$ )	(km s $^{-1}$ )
J0326+0202	$9.47^{+0.08}_{-0.08}$	$0.03^{+0.00}_{-0.00}$	$-1.15^{+0.08}_{-0.07}$	$-115.54^{+2.84}_{-2.79}$	$-201.44^{+13.81}_{-13.13}$	$-22.65^{+3.24}_{-3.39}$	$-115.55^{+2.84}_{-2.79}$	$201.44^{+13.13}_{-13.81}$	$117.74^{+4.31}_{-4.39}$
J1108+2530	$8.83^{+0.05}_{-0.05}$	$0.38^{+0.03}_{-0.03}$	$1.77^{+0.13}_{-0.13}$	$183.79^{+9.97}_{-10.14}$	$-287.20^{+24.04}_{-23.70}$	$-120.18^{+1.86}_{-1.89}$	$183.57^{+9.94}_{-10.10}$	$287.33^{+23.72}_{-24.05}$	$219.41^{+10.11}_{-10.27}$
J1256+3440	$8.40^{+0.03}_{-0.03}$	$-0.43^{+0.06}_{-0.06}$	$3.59^{+0.46}_{-0.47}$	$182.38^{+23.98}_{-24.38}$	$-110.44^{+20.46}_{-19.99}$	$317.44^{+3.91}_{-3.86}$	$182.48^{+24.02}_{-24.40}$	$110.27^{+19.95}_{-20.42}$	$366.15^{+24.34}_{-24.70}$
J1413+1727	$6.69^{+0.23}_{-0.23}$	$-0.27^{+0.04}_{-0.04}$	$3.99^{+0.60}_{-0.60}$	$92.72^{+7.03}_{-6.93}$	$-220.29^{+36.13}_{-35.81}$	$104.85^{+0.87}_{-0.90}$	$92.875^{+7.08}_{-6.98}$	$220.23^{+35.80}_{-36.11}$	$140.07^{+7.13}_{-7.04}$
J1630+0953	$3.67^{+0.60}_{-0.62}$	$-2.15^{+0.28}_{-0.29}$	$3.63^{+0.49}_{-0.47}$	$142.91^{+12.36}_{-11.93}$	$-311.69^{+44.89}_{-46.83}$	$131.88^{+12.42}_{-12.03}$	$145.78^{+13.76}_{-12.88}$	$310.35^{+46.32}_{-44.49}$	$196.58^{+18.54}_{-17.62}$
J2216+0246	$7.31^{+0.12}_{-0.12}$	$-1.96^{+0.26}_{-0.26}$	$-1.93^{+0.25}_{-0.25}$	$-37.84^{+2.70}_{-2.79}$	$-187.73^{+17.67}_{-17.68}$	$-72.86^{+18.67}_{-18.72}$	$-36.98^{+2.54}_{-2.60}$	$187.90^{+17.70}_{-17.70}$	$81.71^{+18.84}_{-18.90}$

NOTE—The – and + indicate the 16th percentile and 84th percentiles

**Table 8.** Calculated Orbital Parameters, Energies and Angular Momenta.

Star	$r_{apo}$	$r_{peri}$	$Z_{max}$	e	E	$L_Z$
	(kpc)				$(10^3 \text{ km}^2 \text{ s}^{-2})$	$(\text{kpc km s}^{-1})$
J0326+0202	$10.88^{+0.18}_{-0.16}$	$0.42^{+0.30}_{-0.26}$	$1.35^{+0.05}_{-0.03}$	$0.93^{+0.05}_{-0.05}$	$-0.98^{+0.03}_{-0.03}$	$-214.66^{+29.32}_{-30.21}$
J1108+2530	$15.65^{+1.73}_{-1.31}$	$1.91^{+0.57}_{-0.60}$	$7.43^{+0.23}_{-0.26}$	$0.78^{+0.05}_{-0.03}$	$-0.60^{+0.09}_{-0.09}$	$-1061.80^{+21.31}_{-22.01}$
J1256+3440	$65.94^{+14.83}_{-9.67}$	$8.90^{+0.21}_{-0.19}$	$29.69^{+4.02}_{-2.62}$	$0.76^{+0.04}_{-0.03}$	$-0.52^{+0.08}_{-0.07}$	$2666.88^{+41.09}_{-40.83}$
J1413+1727	$8.03^{+0.10}_{-0.08}$	$2.88^{+0.74}_{-0.25}$	$7.90^{+0.12}_{-0.50}$	$0.47^{+0.03}_{-0.09}$	$-0.91^{+0.09}_{-0.08}$	$700.25^{+25.89}_{-25.67}$
J1630+0953	$7.11^{+2.54}_{-0.69}$	$4.16^{+0.82}_{-1.23}$	$7.11^{+2.50}_{-0.72}$	$0.30^{+0.11}_{-0.04}$	$-1.18^{+0.02}_{-0.02}$	$559.86^{+5.63}_{-5.21}$
J2216+0246	$8.07^{+0.11}_{-0.12}$	$0.47^{+0.60}_{-0.25}$	$3.57^{+2.46}_{-0.92}$	$0.89^{+0.06}_{-0.13}$	$-1.14^{+0.05}_{-0.04}$	$-551.44^{+138.48}_{-137.99}$

NOTE—The – and + indicate the 16th percentile and 84th percentiles



## 参考文献

- Adams F C, Grohs E. Stellar helium burning in other universes: A solution to the triple alpha fine-tuning problem[J/OL]. Astroparticle Physics, 2017, 87:40-54. DOI: [10.1016/j.astropartphys.2016.12.002](https://doi.org/10.1016/j.astropartphys.2016.12.002).
- Alexeeva S, Ryabchikova T, Mashonkina L, et al. NLTE line formation for Mg\ion{+} and Mg\ion{++} in atmospheres of B-A-F-G-K stars[J]. ArXiv e-prints, 2018.
- Alexeeva S A, Pakhomov Y V, Mashonkina L I. Non-LTE sodium abundance in galactic thick- and thin-disk red giants[J/OL]. Astronomy Letters, 2014, 40:406-424. DOI: [10.1134/S1063773714070019](https://doi.org/10.1134/S1063773714070019).
- Alonso A, Arribas S, Martínez-Roger C. The effective temperature scale of giant stars (F0-K5). II. Empirical calibration of  $T_{eff}$  versus colours and [Fe/H][J/OL]. , 1999, 140:261-277. DOI: [10.1051/aas:1999521](https://doi.org/10.1051/aas:1999521).
- Alvarez E, Hakim R. Quark ERA in the primeval universe[J]. , 1979, 80(1):71-76.
- Andrievsky S M, Spite F, Korotin S A, et al. NLTE strontium abundance in a sample of extremely metal poor stars and the Sr/Ba ratio in the early Galaxy[J/OL]. , 2011, 530:A105. DOI: [10.1051/0004-6361/201116591](https://doi.org/10.1051/0004-6361/201116591).
- Aoki W, Honda S, Beers T C, et al. Spectroscopic Studies of Very Metal-poor Stars with the Subaru High Dispersion Spectrograph. III. Light Neutron-Capture Elements[J/OL]. , 2005, 632:611-637. DOI: [10.1086/432862](https://doi.org/10.1086/432862).
- Aoki W, Beers T C, Christlieb N, et al. Carbon-enhanced Metal-poor Stars. I. Chemical Compositions of 26 Stars[J/OL]. , 2007, 655:492-521. DOI: [10.1086/509817](https://doi.org/10.1086/509817).
- Aoki W, Suda T, Boyd R N, et al. Explaining the Sr and Ba Scatter in Extremely Metal-poor Stars [J/OL]. , 2013, 766:L13. DOI: [10.1088/2041-8205/766/1/L13](https://doi.org/10.1088/2041-8205/766/1/L13).
- Archontis V, Vlahos L. Introduction to the physics of solar eruptions and their space weather impact [J/OL]. Philosophical Transactions of the Royal Society of London Series A, 2019, 377(2148): 20190152. DOI: [10.1098/rsta.2019.0152](https://doi.org/10.1098/rsta.2019.0152).
- Argast D, Samland M, Gerhard O E, et al. Metal-poor halo stars as tracers of ISM mixing processes during halo formation[J]. , 2000, 356:873-887.
- Arimoto N. Population III stars and Initial Phase of Galactic Chemical Evolution[C]//Theoretical Aspects on Structure, Activity, and Evolution of Galaxies. 1983: 108.
- Arnould M, Goriely S, Takahashi K. The r-process of stellar nucleosynthesis: Astrophysics and nuclear physics achievements and mysteries[J/OL]. , 2007, 450:97-213. DOI: [10.1016/j.physrep.2007.06.002](https://doi.org/10.1016/j.physrep.2007.06.002).

- Asplund M, Grevesse N, Sauval A J, et al. The Chemical Composition of the Sun[J/OL]. , 2009, 47:481-522. DOI: [10.1146/annurev.astro.46.060407.145222](https://doi.org/10.1146/annurev.astro.46.060407.145222).
- Astropy Collaboration, Robitaille T P, Tollerud E J, et al. Astropy: A community Python package for astronomy[J/OL]. , 2013, 558:A33. DOI: [10.1051/0004-6361/201322068](https://doi.org/10.1051/0004-6361/201322068).
- Astropy Collaboration, Price-Whelan A M, Sipőcz B M, et al. The Astropy Project: Building an Open-science Project and Status of the v2.0 Core Package[J/OL]. , 2018, 156:123. DOI: [10.3847/1538-3881/aabc4f](https://doi.org/10.3847/1538-3881/aabc4f).
- Bailer-Jones C A L, Rybizki J, Fouesneau M, et al. Estimating Distance from Parallaxes. IV. Distances to 1.33 Billion Stars in Gaia Data Release 2[J/OL]. , 2018, 156:58. DOI: [10.3847/1538-3881/aacb21](https://doi.org/10.3847/1538-3881/aacb21).
- Bailey S I. Note on the Structure of the Milky Way.[J]. Harvard College Observatory Circular, 1922, 242:6-8.
- Baker R H. Investigations of Galactic Structure. IV. The Milky Way in Cassiopeia.[J]. Harvard College Observatory Circular, 1939, 424:1-16.
- Barklem P S, Aspelund-Johansson J. The broadening of Fe II lines by neutral hydrogen collisions [J/OL]. , 2005, 435(1):373-377. DOI: [10.1051/0004-6361:20042469](https://doi.org/10.1051/0004-6361:20042469).
- Becker S A, Iben J, I. The asymptotic giant branch evolution of intermediate-mass stars as a function of mass and composition. I. Through the second dredge-up phase.[J/OL]. , 1979, 232:831-853. DOI: [10.1086/157345](https://doi.org/10.1086/157345).
- Beers T C, Christlieb N. The Discovery and Analysis of Very Metal-Poor Stars in the Galaxy[J/OL]. , 2005, 43:531-580. DOI: [10.1146/annurev.astro.42.053102.134057](https://doi.org/10.1146/annurev.astro.42.053102.134057).
- Beers T C, Carollo D, Lee Y, et al. Carbon-Enhanced Metal-Poor (CEMP) Stars in the Halo System of the Galaxy and Their Link with High Redshift Damped Lyman Alpha Systems[C]//American Astronomical Society Meeting Abstracts: volume 219 American Astronomical Society Meeting Abstracts #219. 2012: 222.06.
- Bergemann M, Gehren T. NLTE abundances of Mn in a sample of metal-poor stars[J/OL]. , 2008, 492:823-831. DOI: [10.1051/0004-6361:200810098](https://doi.org/10.1051/0004-6361:200810098).
- Bisterzo S, Gallino R, Straniero O, et al. The s-process in low-metallicity stars - II. Interpretation of high-resolution spectroscopic observations with asymptotic giant branch models[J/OL]. , 2011, 418:284-319. DOI: [10.1111/j.1365-2966.2011.19484.x](https://doi.org/10.1111/j.1365-2966.2011.19484.x).
- Bland-Hawthorn J, Gerhard O. The Galaxy in Context: Structural, Kinematic, and Integrated Properties[J/OL]. , 2016, 54:529-596. DOI: [10.1146/annurev-astro-081915-023441](https://doi.org/10.1146/annurev-astro-081915-023441).
- Bolt M. Book Review: The Long Route to the Invention of the Telescope[J/OL]. Journal for the History of Astronomy, 2010, 41(1):120-122. DOI: [10.1177/002182861004100107](https://doi.org/10.1177/002182861004100107).

- Bolton J G, Westfold K C. Structure of the Galaxy and the Sense of Rotation of Spiral Nebulae [J/OL]. , 1950, 165(4195):487-488. DOI: [10.1038/165487b0](https://doi.org/10.1038/165487b0).
- Bond H E. Where is population III ?[J/OL]. , 1981, 248:606-611. DOI: [10.1086/159186](https://doi.org/10.1086/159186).
- Bond J R, Carr B J, Arnett W D. Can Population III stars generate primordial helium?[J/OL]. , 1983, 304(5926):514-515. DOI: [10.1038/304514a0](https://doi.org/10.1038/304514a0).
- Borexino Collaboration, Agostini M, Altenmüller K, et al. Comprehensive measurement of pp-chain solar neutrinos[J/OL]. , 2018, 562(7728):505-510. DOI: [10.1038/s41586-018-0624-y](https://doi.org/10.1038/s41586-018-0624-y).
- Bovy J. galpy: A python Library for Galactic Dynamics[J/OL]. , 2015, 216:29. DOI: [10.1088/0067-0049/216/2/29](https://doi.org/10.1088/0067-0049/216/2/29).
- Bromm V, Loeb A. The formation of the first low-mass stars from gas with low carbon and oxygen abundances[J/OL]. , 2003, 425:812-814. DOI: [10.1038/nature02071](https://doi.org/10.1038/nature02071).
- Bromm V, Coppi P S, Larson R B. The Formation of the First Stars. I. The Primordial Star-forming Cloud[J/OL]. , 2002, 564(1):23-51. DOI: [10.1086/323947](https://doi.org/10.1086/323947).
- Brook C B, Kawata D, Gibson B K, et al. The Emergence of the Thick Disk in a Cold Dark Matter Universe[J/OL]. , 2004, 612:894-899. DOI: [10.1086/422709](https://doi.org/10.1086/422709).
- Burris D L, Pilachowski C A, Armandroff T E, et al. Neutron-Capture Elements in the Early Galaxy: Insights from a Large Sample of Metal-poor Giants[J/OL]. , 2000, 544:302-319. DOI: [10.1086/317172](https://doi.org/10.1086/317172).
- Butler K, Giddings J. A grid of marcs model atmospheres for late-type stars i. methods and general properties[J]. Newsletter on the analysis of astronomical spectra, 1985, No. 9:University of London.
- Caciolli A, Mazzocchi C, Capogrosso V, et al. Revision of the  $^{15}\text{N}(\text{p}, \gamma)^{16}\text{O}$  reaction rate and oxygen abundance in H-burning zones[J/OL]. , 2011, 533:A66. DOI: [10.1051/0004-6361/201117475](https://doi.org/10.1051/0004-6361/201117475).
- Caerols H, Asenjo F A. Weighing the Sun with five photographs[J]. arXiv e-prints, 2019: arXiv:1906.12272.
- Caffau E, Bonifacio P, François P, et al. An extremely primitive star in the Galactic halo[J/OL]. , 2011, 477:67-69. DOI: [10.1038/nature10377](https://doi.org/10.1038/nature10377).
- Caffau E, Gallagher A J, Bonifacio P, et al. Investigation of a sample of carbon-enhanced metal-poor stars observed with FORS and GMOS[J/OL]. , 2018, 614:A68. DOI: [10.1051/0004-6361/201732475](https://doi.org/10.1051/0004-6361/201732475).
- Carollo D, Beers T C, Lee Y S, et al. Two stellar components in the halo of the Milky Way[J/OL]. , 2007, 450:1020-1025. DOI: [10.1038/nature06460](https://doi.org/10.1038/nature06460).
- Carollo D, Beers T C, Chiba M, et al. Structure and Kinematics of the Stellar Halos and Thick Disks of the Milky Way Based on Calibration Stars from Sloan Digital Sky Survey DR7[J/OL]. , 2010, 712:692-727. DOI: [10.1088/0004-637X/712/1/692](https://doi.org/10.1088/0004-637X/712/1/692).

- Carollo D, Beers T C, Bovy J, et al. Carbon-enhanced Metal-poor Stars in the Inner and Outer Halo Components of the Milky Way[J/OL]. , 2012, 744:195. DOI: [10.1088/0004-637X/744/2/195](https://doi.org/10.1088/0004-637X/744/2/195).
- Carollo D, Freeman K, Beers T C, et al. Carbon-enhanced Metal-poor Stars: CEMP-s and CEMP-no Subclasses in the Halo System of the Milky Way[J/OL]. , 2014, 788:180. DOI: [10.1088/0004-637X/788/2/180](https://doi.org/10.1088/0004-637X/788/2/180).
- Carollo D, Beers T C, Placco V M, et al. The age structure of the Milky Way's halo[J/OL]. Nature Physics, 2016, 12:1170-1176. DOI: [10.1038/nphys3874](https://doi.org/10.1038/nphys3874).
- Carollo D, Tissera P B, Beers T C, et al. The Origin of the Milky Way's Halo Age Distribution [J/OL]. , 2018, 859:L7. DOI: [10.3847/2041-8213/aac2dc](https://doi.org/10.3847/2041-8213/aac2dc).
- Carr B. Where is Population III?[J/OL]. , 1987, 326(6116):829-830. DOI: [10.1038/326829b0](https://doi.org/10.1038/326829b0).
- Carretta E, Gratton R G, Sneden C. Abundances of light elements in metal-poor stars. III. Data analysis and results[J]. , 2000, 356:238-252.
- Castellani V, Chieffi A, Pulone L. The Evolution of He-burning Stars: Horizontal and Asymptotic Branches in Galactic Globulars[J/OL]. , 1991, 76:911. DOI: [10.1086/191584](https://doi.org/10.1086/191584).
- Castellani V, Chieffi A, Straniero O. The Evolution of Intermediate-Mass Stars through the H- and He-burning Phases[J/OL]. , 1990, 74:463. DOI: [10.1086/191506](https://doi.org/10.1086/191506).
- Castelli F, Kurucz R L. New Grids of ATLAS9 Model Atmospheres[C]//Piskunov N, Weiss W W, Gray D F. IAU Symposium: volume 210 Modelling of Stellar Atmospheres. 2003: A20.
- Cayrel R, Depagne E, Spite M, et al. First stars V - Abundance patterns from C to Zn and supernova yields in the early Galaxy[J/OL]. , 2004, 416:1117-1138. DOI: [10.1051/0004-6361:20034074](https://doi.org/10.1051/0004-6361:20034074).
- Chamberlain J W, Aller L H. The Atmospheres of A-Type Subdwarfs and 95 Leonis.[J/OL]. , 1951, 114:52. DOI: [10.1086/145451](https://doi.org/10.1086/145451).
- Chen B Q, Huang Y, Hou L G, et al. The Galactic spiral structure as revealed by O- and early B-type stars[J/OL]. , 2019, 487(1):1400-1409. DOI: [10.1093/mnras/stz1357](https://doi.org/10.1093/mnras/stz1357).
- Chiba M, Beers T C. Kinematics of Metal-poor Stars in the Galaxy. III. Formation of the Stellar Halo and Thick Disk as Revealed from a Large Sample of Nonkinematically Selected Stars[J/OL]. , 2000, 119:2843-2865. DOI: [10.1086/301409](https://doi.org/10.1086/301409).
- Chieffi A. The evolution of massive stars with mass loss: the H and He burning phases[J/OL]. Journal of Korean Physical Society, 2010, 56(51):1673. DOI: [10.3938/jkps.56.1673](https://doi.org/10.3938/jkps.56.1673).
- Christlieb N, Bessell M S, Beers T C, et al. A stellar relic from the early Milky Way[J/OL]. , 2002, 419:904-906. DOI: [10.1038/nature01142](https://doi.org/10.1038/nature01142).
- Cohen J G, Christlieb N, McWilliam A, et al. New Extremely Metal-Poor Stars in the Galactic Halo [J/OL]. , 2008, 672(1):320-341. DOI: [10.1086/523638](https://doi.org/10.1086/523638).
- Collins C B, Hawking S W. Why is the Universe Isotropic?[J/OL]. , 1973, 180:317-334. DOI: [10.1086/151965](https://doi.org/10.1086/151965).

- Cooper A P, Parry O H, Lowing B, et al. Formation of in situ stellar haloes in Milky Way-mass galaxies[J/OL]. , 2015, 454:3185-3199. DOI: [10.1093/mnras/stv2057](https://doi.org/10.1093/mnras/stv2057).
- Cristallo S, Straniero O, Gallino R, et al. Evolution, Nucleosynthesis, and Yields of Low-Mass Asymptotic Giant Branch Stars at Different Metallicities[J/OL]. , 2009, 696:797-820. DOI: [10.1088/0004-637X/696/1/797](https://doi.org/10.1088/0004-637X/696/1/797).
- Cristallo S, Piersanti L, Straniero O, et al. Evolution, Nucleosynthesis, and Yields of Low-mass Asymptotic Giant Branch Stars at Different Metallicities. II. The FRUITY Database[J/OL]. , 2011, 197:17. DOI: [10.1088/0067-0049/197/2/17](https://doi.org/10.1088/0067-0049/197/2/17).
- Cruz M A, Cogo-Moreira H, Rossi S. Searching for chemical classes among metal-poor stars using medium-resolution spectroscopy[J/OL]. , 2018, 475:4781-4793. DOI: [10.1093/mnras/stx3330](https://doi.org/10.1093/mnras/stx3330).
- Cui X Q, Zhao Y H, Chu Y Q, et al. The Large Sky Area Multi-Object Fiber Spectroscopic Telescope (LAMOST)[J/OL]. Research in Astronomy and Astrophysics, 2012, 12:1197-1242. DOI: [10.1088/1674-4527/12/9/003](https://doi.org/10.1088/1674-4527/12/9/003).
- Cunningham C J. Book Review: The Scientific Legacy of William Herschel[J]. Journal of Astronomical History and Heritage, 2018, 21:251-253.
- de Araujo J C N, Opher R. The Evolution of Population III Objects[J]. , 1990, 21:322.
- de Diego R, Garrido E, Fedorov D V, et al. The triple alpha reaction rate and the  $2^+$  resonances in  $^{12}\text{C}$ [J/OL]. Physics Letters B, 2011, 695(1-4):324-328. DOI: [10.1016/j.physletb.2010.11.001](https://doi.org/10.1016/j.physletb.2010.11.001).
- deg'l Innocenti S, Cassisi S, Castellani V, et al. Theoretical uncertainties on the evolution of HB and AGB-clump stars[J]. , 2001, 72:703-706.
- Deliyannis C P, Demarque P, Pinsonneault M H. Primordial Lithium, Stellar Evolution, Big Bang Cosmology, and Dark Matter[C]//: volume 22. 1990: 1214.
- Demarque P, Woo J H, Kim Y C, et al.  $\text{Y}^2$  Isochrones with an Improved Core Overshoot Treatment [J/OL]. , 2004, 155:667-674. DOI: [10.1086/424966](https://doi.org/10.1086/424966).
- Dodelson S, Jubas J M. Re-ionization and decaying dark matter[R]//NASA STI/Recon Technical Report N. 1991: 11944.
- Dolgov A D, Sazhin M V, Zeldovich Y B. Basics of modern cosmology[M]. 1990.
- E Smith D, Zuber M T. The Change in the Mass of the Sun and the Expansion of the Solar System [C]//EGU General Assembly Conference Abstracts: volume 19. 2017: 11131.
- Efstathiou G, Sutherland W J, Maddox S J. The cosmological constant and cold dark matter[J/OL]. , 1990, 348(6303):705-707. DOI: [10.1038/348705a0](https://doi.org/10.1038/348705a0).
- Ellis G F R, Maartens R, Nel S D. The expansion of the Universe.[J/OL]. , 1978, 184:439-465. DOI: [10.1093/mnras/184.3.439](https://doi.org/10.1093/mnras/184.3.439).
- Espin T E. The Dark Structures in the Milky Way[J]. , 1912, 6:225.

- Ezzeddine R, Frebel A, Roederer I U, et al. Evidence for an aspherical Population III supernova explosion inferred from the hyper metal-poor star HE1327-2326[J]. arXiv e-prints, 2019.
- Font A S, McCarthy I G, Crain R A, et al. Cosmological simulations of the formation of the stellar haloes around disc galaxies[J/OL]. , 2011, 416:2802-2820. DOI: [10.1111/j.1365-2966.2011.19227.x](https://doi.org/10.1111/j.1365-2966.2011.19227.x).
- Ford L H. Gravitational particle creation and inflation[J/OL]. , 1987, 35(10):2955-2960. DOI: [10.1103/PhysRevD.35.2955](https://doi.org/10.1103/PhysRevD.35.2955).
- François P, Depagne E, Hill V, et al. First stars. VIII. Enrichment of the neutron-capture elements in the early Galaxy[J/OL]. , 2007, 476:935-950. DOI: [10.1051/0004-6361:20077706](https://doi.org/10.1051/0004-6361:20077706).
- Frebel A. From Nuclei to the Cosmos: Tracing Heavy-Element Production with the Oldest Stars[J/OL]. Annual Review of Nuclear and Particle Science, 2018, 68:237-269. DOI: [10.1146/annurev-nucl-101917-021141](https://doi.org/10.1146/annurev-nucl-101917-021141).
- Frebel A, Aoki W, Christlieb N, et al. Nucleosynthetic signatures of the first stars[J/OL]. , 2005, 434:871-873. DOI: [10.1038/nature03455](https://doi.org/10.1038/nature03455).
- Frebel A, Johnson J L, Bromm V. Probing the formation of the first low-mass stars with stellar archaeology[J/OL]. , 2007, 380:L40-L44. DOI: [10.1111/j.1745-3933.2007.00344.x](https://doi.org/10.1111/j.1745-3933.2007.00344.x).
- Frebel A, Casey A R, Jacobson H R, et al. Deriving Stellar Effective Temperatures of Metal-poor Stars with the Excitation Potential Method[J/OL]. , 2013, 769:57. DOI: [10.1088/0004-637X/769/1/57](https://doi.org/10.1088/0004-637X/769/1/57).
- Frischknecht U, Hirschi R, Thielemann F K. Non-standard s-process in low metallicity massive rotating stars[J/OL]. , 2012, 538:L2. DOI: [10.1051/0004-6361/201117794](https://doi.org/10.1051/0004-6361/201117794).
- Gaia Collaboration, Brown A G A, Vallenari A, et al. Gaia Data Release 2. Summary of the contents and survey properties[J/OL]. , 2018, 616:A1. DOI: [10.1051/0004-6361/201833051](https://doi.org/10.1051/0004-6361/201833051).
- Galli D, Palla F. Chemistry and Cooling of the Primordial Gas[C/OL]//Weiss A, Abel T G, Hill V. The First Stars. 2000: 229. DOI: [10.1007/10719504\\_4](https://doi.org/10.1007/10719504_4).
- Gallino R, Arlandini C, Busso M, et al. Evolution and Nucleosynthesis in Low-Mass Asymptotic Giant Branch Stars. II. Neutron Capture and the S-Process[J/OL]. , 1998, 497:388-403. DOI: [10.1086/305437](https://doi.org/10.1086/305437).
- Gibson E G. Description of solar structure and processes.[J/OL]. Reviews of Geophysics and Space Physics, 1972, 10:395-461. DOI: [10.1029/RG010i002p00395](https://doi.org/10.1029/RG010i002p00395).
- Ginzburg V L. The universe and its evolution.[J]. Fiz.-mat. spisanie, 1969, 12(2):111-124.
- Glover S. The First Stars[C/OL]//Wiklind T, Mobasher B, Bromm V. Astrophysics and Space Science Library: volume 396 The First Galaxies. 2013: 103. DOI: [10.1007/978-3-642-32362-1\\_3](https://doi.org/10.1007/978-3-642-32362-1_3).
- Goriely S, Mowlavi N. Neutron-capture nucleosynthesis in AGB stars[J]. , 2000, 362:599-614.
- Gratton R G, Sneden C, Carretta E, et al. Mixing along the red giant branch in metal-poor field stars [J]. , 2000, 354:169-187.

- Gray R O, Corbally C J. The Calibration of MK Spectral Classes Using Spectral Synthesis. I. The Effective Temperature Calibration of Dwarf Stars[J/OL]. , 1994, 107:742. DOI: [10.1086/116893](https://doi.org/10.1086/116893).
- Greenstein G S. The helium problem in cosmology.[D]. -, 1969.
- Greif T H. The numerical frontier of the high-redshift Universe[J/OL]. Computational Astrophysics and Cosmology, 2015, 2:3. DOI: [10.1186/s40668-014-0006-2](https://doi.org/10.1186/s40668-014-0006-2).
- Grillmair C J. Four New Stellar Debris Streams in the Galactic Halo[J/OL]. , 2009, 693:1118-1127. DOI: [10.1088/0004-637X/693/2/1118](https://doi.org/10.1088/0004-637X/693/2/1118).
- Hansen C J, Montes F, Arcones A. How Many Nucleosynthesis Processes Exist at Low Metallicity? [J/OL]. , 2014, 797:123. DOI: [10.1088/0004-637X/797/2/123](https://doi.org/10.1088/0004-637X/797/2/123).
- Hansen C J, Nordström B, Hansen T T, et al. Abundances of carbon-enhanced metal-poor stars as constraints on their formation[J/OL]. , 2016, 588:A37. DOI: [10.1051/0004-6361/201526895](https://doi.org/10.1051/0004-6361/201526895).
- Hansen T T, Andersen J, Nordström B, et al. The role of binaries in the enrichment of the early Galactic halo. II. Carbon-enhanced metal-poor stars: CEMP-no stars[J/OL]. , 2016, 586:A160. DOI: [10.1051/0004-6361/201527235](https://doi.org/10.1051/0004-6361/201527235).
- Hansen T T, Andersen J, Nordström B, et al. The role of binaries in the enrichment of the early Galactic halo. III. Carbon-enhanced metal-poor stars - CEMP-s stars[J/OL]. , 2016, 588:A3. DOI: [10.1051/0004-6361/201527409](https://doi.org/10.1051/0004-6361/201527409).
- Hara T, Miyoshi S. Formation of Population-III Objects due to Cosmic Strings[C]//Grindlay J E, Philip A G D. IAU Symposium: volume 126 The Harlow-Shapley Symposium on Globular Cluster Systems in Galaxies. 1988: 701.
- Harrison E R. Matter, Antimatter, and the Origin of Galaxies[J/OL]. , 1967, 18(23):1011-1013. DOI: [10.1103/PhysRevLett.18.1011](https://doi.org/10.1103/PhysRevLett.18.1011).
- Hawkins G S. Expansion of the Universe[J/OL]. , 1962, 194(4828):563-564. DOI: [10.1038/194563a0](https://doi.org/10.1038/194563a0).
- Hayashi C, Cameron R C. The Evolution of Massive Stars After Hydrogen Exhaustion in the Core. [J/OL]. , 1960, 65:490. DOI: [10.1086/108170](https://doi.org/10.1086/108170).
- Hayashi C, Cameron R C. Evolution of Massive Stars after Helium Burning.[J/OL]. , 1962, 67:577. DOI: [10.1086/108840](https://doi.org/10.1086/108840).
- Hayashi C, Cameron R C. The Evolution of Massive Stars. III. Hydrogen Exhaustion Through the Onset of Carbon-Burning[J/OL]. , 1962, 136:166. DOI: [10.1086/147362](https://doi.org/10.1086/147362).
- Hayes C R, Majewski S R, Hasselquist S, et al. Disk-like Chemistry of the Triangulum-Andromeda Overdensity as Seen by APOGEE[J/OL]. , 2018, 859(1):L8. DOI: [10.3847/2041-8213/aac38c](https://doi.org/10.3847/2041-8213/aac38c).
- Haywood M, Snaith O, Lehner M D, et al. Revisiting long-standing puzzles of the Milky Way: the Sun and its vicinity as typical outer disk chemical evolution[J/OL]. , 2019, 625:A105. DOI: [10.1051/0004-6361/201834155](https://doi.org/10.1051/0004-6361/201834155).

- Heger A, Woosley S E. The Nucleosynthetic Signature of Population III[J/OL]. , 2002, 567(1): 532-543. DOI: [10.1086/338487](https://doi.org/10.1086/338487).
- Heger A, Woosley S E. Nucleosynthesis and Evolution of Massive Metal-free Stars[J/OL]. , 2010, 724:341-373. DOI: [10.1088/0004-637X/724/1/341](https://doi.org/10.1088/0004-637X/724/1/341).
- Helmi A, Babusiaux C, Koppelman H H, et al. The merger that led to the formation of the Milky Way's inner stellar halo and thick disk[J/OL]. , 2018, 563:85-88. DOI: [10.1038/s41586-018-0625-x](https://doi.org/10.1038/s41586-018-0625-x).
- Hirano S, Hosokawa T, Yoshida N, et al. One Hundred First Stars: Protostellar Evolution and the Final Masses[J/OL]. , 2014, 781:60. DOI: [10.1088/0004-637X/781/2/60](https://doi.org/10.1088/0004-637X/781/2/60).
- Hirschi R. Very low-metallicity massive stars: Pre-SN evolution models and primary nitrogen production[J/OL]. , 2007, 461:571-583. DOI: [10.1051/0004-6361:20065356](https://doi.org/10.1051/0004-6361:20065356).
- Honda S, Aoki W, Kajino T, et al. Spectroscopic Studies of Extremely Metal-Poor Stars with the Subaru High Dispersion Spectrograph. II. The r-Process Elements, Including Thorium[J/OL]. , 2004, 607:474-498. DOI: [10.1086/383406](https://doi.org/10.1086/383406).
- Honda S, Aoki W, Ishimaru Y, et al. Neutron-Capture Elements in the Very Metal Poor Star HD 122563[J/OL]. , 2006, 643:1180-1189. DOI: [10.1086/503195](https://doi.org/10.1086/503195).
- Hotta H, Iijima H, Kusano K. First comprehensive calculation of the whole solar convection zone [C]//Catalyzing Solar Connections. 2018: 46.
- House E L, Brook C B, Gibson B K, et al. Disc heating: comparing the Milky Way with cosmological simulations[J/OL]. , 2011, 415:2652-2664. DOI: [10.1111/j.1365-2966.2011.18891.x](https://doi.org/10.1111/j.1365-2966.2011.18891.x).
- Hoyle F, Schwarzschild M. On the Evolution of Type II Stars.[J/OL]. , 1955, 2:1. DOI: [10.1086/190015](https://doi.org/10.1086/190015).
- Huang L, Adams F C, Grohs E. Sensitivity of carbon and oxygen yields to the triple-alpha resonance in massive stars[J/OL]. Astroparticle Physics, 2019, 105:13-24. DOI: [10.1016/j.astropartphys.2018.09.005](https://doi.org/10.1016/j.astropartphys.2018.09.005).
- Iben J, Icko, Rood R T. Metal-Poor Stars. III. on the Evolution of Horizontal-Branch Stars[J/OL]. , 1970, 161:587. DOI: [10.1086/150563](https://doi.org/10.1086/150563).
- Iben J, Icko, Ritossa C, García-Berro E. On the Evolution of Stars that Form Electron-degenerate Cores Processed by Carbon Burning. IV. Outward Mixing During the Second Dredge-up Phase and Other Properties of a 10.5 M Model Star[J/OL]. , 1997, 489(2):772-790. DOI: [10.1086/304822](https://doi.org/10.1086/304822).
- Ignat'ev A Y, Kuz'min V A, Shaposhnikov M E. On the origin of baryon asymmetry of the universe. [J]. Pisma v Zhurnal Eksperimentalnoi i Teoreticheskoi Fiziki, 1979, 30:726-730.
- Ishigaki M N, Tominaga N, Kobayashi C, et al. The Initial Mass Function of the First Stars Inferred from Extremely Metal-poor Stars[J/OL]. , 2018, 857:46. DOI: [10.3847/1538-4357/aab3de](https://doi.org/10.3847/1538-4357/aab3de).

- Ito H, Aoki W, Beers T C, et al. Chemical Analysis of the Ninth Magnitude Carbon-enhanced Metal-poor Star BD+44deg 493[J/OL]., 2013, 773 : 33. DOI: [10.1088/0004-637X/773/1/33](https://doi.org/10.1088/0004-637X/773/1/33).
- Jones A. Greek Cosmology and Cosmogony[M/OL]. 2015: 1549. DOI: [10.1007/978-1-4614-6141-8\\_54](https://doi.org/10.1007/978-1-4614-6141-8_54).
- Jurić M, Ivezić Ž, Brooks A, et al. The Milky Way Tomography with SDSS. I. Stellar Number Density Distribution[J/OL]., 2008, 673:864-914. DOI: [10.1086/523619](https://doi.org/10.1086/523619).
- Jurčák J, Kašparová J, Švanda M, et al. Heating of the solar photosphere during a white-light flare [J/OL]., 2018, 620:A183. DOI: [10.1051/0004-6361/201833946](https://doi.org/10.1051/0004-6361/201833946).
- Keller S C, Bessell M S, Frebel A, et al. A single low-energy, iron-poor supernova as the source of metals in the star SMSS J031300.36-670839.3[J/OL]., 2014, 506:463-466. DOI: [10.1038/nature12990](https://doi.org/10.1038/nature12990).
- Kerr F J, Lynden-Bell D. Review of galactic constants[J/OL]., 1986, 221:1023-1038. DOI: [10.1093/mnras/221.4.1023](https://doi.org/10.1093/mnras/221.4.1023).
- Kervella P, Decin L, Richards A M S, et al. The close circumstellar environment of Betelgeuse. V. Rotation velocity and molecular envelope properties from ALMA[J/OL]., 2018, 609:A67. DOI: [10.1051/0004-6361/201731761](https://doi.org/10.1051/0004-6361/201731761).
- Kessar M, Hughes D W, Kersalé E, et al. Scale Selection in the Stratified Convection of the Solar Photosphere[J/OL]., 2019, 874(1):103. DOI: [10.3847/1538-4357/ab07bf](https://doi.org/10.3847/1538-4357/ab07bf).
- Kielty C L, Venn K A, Loewen N B, et al. Carbon-enhanced metal-poor stars in the SDSS-APOGEE data base[J/OL]., 2017, 471:404-421. DOI: [10.1093/mnras/stx1594](https://doi.org/10.1093/mnras/stx1594).
- Kochukhov O. [Z]. 2010.
- Koebke K. Hadronic matter.[D]. -, 1973.
- Lamb S A, Iben J, I., Howard W M. On the evolution of massive stars through the core carbon-burning phase.[J/OL]., 1976, 207:209-232. DOI: [10.1086/154486](https://doi.org/10.1086/154486).
- Leavitt H S. 1777 variables in the Magellanic Clouds[J]. Annals of Harvard College Observatory, 1908, 60:87-108.3.
- Leavitt H S, Pickering E C. Periods of 25 Variable Stars in the Small Magellanic Cloud.[J]. Harvard College Observatory Circular, 1912, 173:1-3.
- LEBLANC F. An introduction to stellar astrophysics[M/OL]. Canada: Wiley, 2010. <http://books.google.jo/books?id=V684xcaD9cwC>.
- Lind K, Asplund M, Barklem P S. Departures from LTE for neutral Li in late-type stars[J/OL]., 2009, 503:541-544. DOI: [10.1051/0004-6361/200912221](https://doi.org/10.1051/0004-6361/200912221).
- Linde A D. Quantum creation of the inflationary Universe.[J]. Nuovo Cimento Lettere, 1984, 39: 401-405.

- Lucatello S, Tsangarides S, Beers T C, et al. The Binary Frequency Among Carbon-enhanced, s-Process-rich, Metal-poor Stars[J/OL]. , 2005, 625:825-832. DOI: [10.1086/428104](https://doi.org/10.1086/428104).
- Lugaro M, Karakas A I, Stancliffe R J, et al. The s-process in Asymptotic Giant Branch Stars of Low Metallicity and the Composition of Carbon-enhanced Metal-poor Stars[J/OL]. , 2012, 747: 2. DOI: [10.1088/0004-637X/747/1/2](https://doi.org/10.1088/0004-637X/747/1/2).
- Luri X, Brown A G A, Sarro L M, et al. Gaia Data Release 2. Using Gaia parallaxes[J/OL]. , 2018, 616:A9. DOI: [10.1051/0004-6361/201832964](https://doi.org/10.1051/0004-6361/201832964).
- Macrae D A. The Structure of the Galaxy from a Study of Regions not in the Galactic Plane.[D]. HARVARD UNIVERSITY., 1943.
- Maeder A, Meynet G, Chiappini C. The first stars: CEMP-no stars and signatures of spinstars[J/OL]. , 2015, 576:A56. DOI: [10.1051/0004-6361/201424153](https://doi.org/10.1051/0004-6361/201424153).
- Mardini M K, Ershiadat N, Al-Wardat M A, et al. The Nucleosynthesis and Reaction Rates of Fluorine 19 ( $^{19}F$ ) in the Sun[J]. arXiv e-prints, 2019:arXiv:1904.09608.
- Mardini M K, Li H, Placco V M, et al. Metal-poor Stars Observed with the Automated Planet Finder Telescope. I. Discovery of Five Carbon-enhanced Metal-poor Stars from LAMOST[J/OL]. , 2019, 875(2):89. DOI: [10.3847/1538-4357/ab0fa2](https://doi.org/10.3847/1538-4357/ab0fa2).
- Mardini M K, Placco V M, Taani A, et al. Metal-poor Stars Observed with the Automated Planet Finder Telescope. II. Chemodynamical Analysis of Six Low-Metallicity Stars in the Halo System of the Milky Way[J]. arXiv e-prints, 2019:arXiv:1906.08439.
- Mashonkina L, Jablonka P, Pakhomov Y, et al. The formation of the Milky Way halo and its dwarf satellites; a NLTE-1D abundance analysis. I. Homogeneous set of atmospheric parameters[J/OL]. , 2017, 604:A129. DOI: [10.1051/0004-6361/201730779](https://doi.org/10.1051/0004-6361/201730779).
- Masseron T, Johnson J A, Plez B, et al. A holistic approach to carbon-enhanced metal-poor stars [J/OL]. , 2010, 509:A93. DOI: [10.1051/0004-6361/200911744](https://doi.org/10.1051/0004-6361/200911744).
- Matteucci F, Recchi S. On the Typical Timescale for the Chemical Enrichment from Type Ia Supernovae in Galaxies[J/OL]. , 2001, 558(1):351-358. DOI: [10.1086/322472](https://doi.org/10.1086/322472).
- McCarthy I G, Font A S, Crain R A, et al. Global structure and kinematics of stellar haloes in cosmological hydrodynamic simulations[J/OL]. , 2012, 420:2245-2262. DOI: [10.1111/j.1365-2966.2011.20189.x](https://doi.org/10.1111/j.1365-2966.2011.20189.x).
- McCrea W H. A Philosophy for Big-Bang Cosmology[J/OL]. , 1970, 228(5266):21-24. DOI: [10.1038/228021a0](https://doi.org/10.1038/228021a0).
- McMillan P J. The mass distribution and gravitational potential of the Milky Way[J/OL]. , 2017, 465:76-94. DOI: [10.1093/mnras/stw2759](https://doi.org/10.1093/mnras/stw2759).
- McWilliam A. Barium Abundances in Extremely Metal-poor Stars[J/OL]. , 1998, 115(4):1640-1647. DOI: [10.1086/300289](https://doi.org/10.1086/300289).

- McWilliam A, Preston G W, Sneden C, et al. Spectroscopic Analysis of 33 of the Most Metal Poor Stars. II.[J/OL]. , 1995, 109:2757. DOI: [10.1086/117486](https://doi.org/10.1086/117486).
- Menou K, Le Mer J. Magnetorotational Transport in the Early Sun[J/OL]. , 2006, 650(2):1208-1216. DOI: [10.1086/507022](https://doi.org/10.1086/507022).
- Meyer B S. The r-, s-, and p-Processes in Nucleosynthesis[J/OL]. , 1994, 32:153-190. DOI: [10.1146/annurev.aa.32.090194.001101](https://doi.org/10.1146/annurev.aa.32.090194.001101).
- Meynet G, Ekström S, Maeder A. The early star generations: the dominant effect of rotation on the CNO yields[J/OL]. , 2006, 447:623-639. DOI: [10.1051/0004-6361:20053070](https://doi.org/10.1051/0004-6361:20053070).
- Mihalas D, Binney J. Book-Review - Galactic Astronomy - Structure and Kinematics[J]. Science, 1981, 214:829.
- Mitton S. The Cambridge encyclopaedia of astronomy[M]. 1977.
- Monachesi A, Gómez F A, Grand R J J, et al. On the stellar halo metallicity profile of Milky Way-like galaxies in the Auriga simulations[J/OL]. , 2016, 459:L46-L50. DOI: [10.1093/mnrasl/slw052](https://doi.org/10.1093/mnrasl/slw052).
- Mozel P. Book Review - Our Cosmic Origins: From the Big Bang to the Emergence of Life and Intelligence Book Authors Delsemme, Armand[J]. , 2000, 94:198-198.
- Murdin P. Big Bang Theory[M/OL]. 2000: 4801. DOI: [10.1888/0333750888/4801](https://doi.org/10.1888/0333750888/4801).
- Nissen P E, Gustafsson B, Edvardsson B, et al. Chemical composition and atmospheric parameters of metal-poor halo stars[J]. , 1994, 285:440-450.
- Nomoto K, Kobayashi C, Tominaga N. Nucleosynthesis in Stars and the Chemical Enrichment of Galaxies[J/OL]. , 2013, 51:457-509. DOI: [10.1146/annurev-astro-082812-140956](https://doi.org/10.1146/annurev-astro-082812-140956).
- Norris J E, Ryan S G, Beers T C. Extremely Metal-Poor Stars. VIII. High-Resolution, High Signal-to-Noise Ratio Analysis of Five Stars with [Fe/H]<~−3.5[J/OL]. , 2001, 561(2):1034-1059. DOI: [10.1086/323429](https://doi.org/10.1086/323429).
- Norris J E, Christlieb N, Korn A J, et al. HE 0557-4840: Ultra-Metal-Poor and Carbon-Rich[J/OL]. , 2007, 670(1):774-788. DOI: [10.1086/521919](https://doi.org/10.1086/521919).
- Ober W W, El Eid M F, Fricke K J. Evolution and nucleosynthesis in Population III stars[C]// Rees M J, Stoneham R J. NATO Advanced Science Institutes (ASI) Series C: volume 90. 1982: 293-301.
- Oort J H. Investigations concerning the rotational motion of the galactic system together with new determinations of secular parallaxes, precession and motion of the equinox (Errata: 4 94)[J]. , 1927, 4:79.
- Orcajo S, Cieza L A, Gamen R, et al. Evidence for disc regulation in the lowest mass stars of the young stellar cluster NGC 2264[J/OL]. , 2019, 487(2):2937-2946. DOI: [10.1093/mnras/stz1452](https://doi.org/10.1093/mnras/stz1452).
- Osorio Y, Barklem P S, Lind K, et al. The influence of electron collisions on non-LTE Li line formation in stellar atmospheres[J/OL]. , 2011, 529:A31. DOI: [10.1051/0004-6361/201016418](https://doi.org/10.1051/0004-6361/201016418).

- Paczyński B. Evolution of Single Stars. II. Core Helium Burning in Population I Stars[J]. , 1970, 20:195.
- Page D N. Inflation does not explain time asymmetry[J/OL]. , 1983, 304(5921):39-41. DOI: [10.1038/304039a0](https://doi.org/10.1038/304039a0).
- Pagel B E J. Helium and Big Bang nucleosynthesis[J/OL]. , 2000, 333:433-447. DOI: [10.1016/S0370-1573\(00\)00033-8](https://doi.org/10.1016/S0370-1573(00)00033-8).
- Pannekoek A. Researches into the structure of the galaxy[J]. Koninklijke Nederlandse Akademie van Wetenschappen Proceedings Series B Physical Sciences, 1910, 13:239-258.
- Park C. Electron impact excitation rate coefficients for hydrogen, helium and alkali atoms.[J/OL]. , 1971, 11:7-36. DOI: [10.1016/0022-4073\(71\)90158-0](https://doi.org/10.1016/0022-4073(71)90158-0).
- Parker L. Quantized Fields and Particle Creation in Expanding Universes. I[J/OL]. Physical Review, 1969, 183(5):1057-1068. DOI: [10.1103/PhysRev.183.1057](https://doi.org/10.1103/PhysRev.183.1057).
- Pillepich A, Madau P, Mayer L. Building Late-type Spiral Galaxies by In-situ and Ex-situ Star Formation[J/OL]. , 2015, 799:184. DOI: [10.1088/0004-637X/799/2/184](https://doi.org/10.1088/0004-637X/799/2/184).
- Placco V M, Beers T C, Roederer I U, et al. Hubble Space Telescope Near-ultraviolet Spectroscopy of the Bright CEMP-no Star BD+44deg 493[J/OL]. , 2014, 790 : 34. DOI : [10.1088/0004-637X/790/1/34](https://doi.org/10.1088/0004-637X/790/1/34).
- Placco V M, Frebel A, Beers T C, et al. Carbon-enhanced Metal-poor Star Frequencies in the Galaxy: Corrections for the Effect of Evolutionary Status on Carbon Abundances[J/OL]. , 2014, 797:21. DOI: [10.1088/0004-637X/797/1/21](https://doi.org/10.1088/0004-637X/797/1/21).
- Placco V M, Beers T C, Reggiani H, et al. G64-12 and G64-37 Are Carbon-enhanced Metal-poor Stars[J/OL]. , 2016, 829:L24. DOI: [10.3847/2041-8205/829/2/L24](https://doi.org/10.3847/2041-8205/829/2/L24).
- Plaskett J S. Book Reviews: The Dimensions and Structure of the Galaxy[J]. Popular Astronomy, 1936, 44:466.
- Pols O R, Izzard R G, Stancliffe R J, et al. The occurrence of nitrogen-enhanced metal-poor stars: implications for the initial mass function in the early Galactic halo[J/OL]. , 2012, 547:A76. DOI: [10.1051/0004-6361/201219597](https://doi.org/10.1051/0004-6361/201219597).
- Puget J L, Heyvaerts J. Population III stars and the shape of the cosmological black body radiation [J]. , 1980, 83(3):L10-L12.
- Puy D, Signore M. Primordial molecules in the early cloud formation.[J]. , 1996, 305:371.
- Qian Y Z, Wasserburg G J. Stellar Sources for Heavy r-Process Nuclei[J/OL]. , 2003, 588:1099-1109. DOI: [10.1086/374271](https://doi.org/10.1086/374271).
- Qian Y Z, Wasserburg G J. Abundances of Sr, Y, and Zr in Metal-Poor Stars and Implications for Chemical Evolution in the Early Galaxy[J/OL]. , 2008, 687:272-286. DOI: [10.1086/591545](https://doi.org/10.1086/591545).
- Radovan M V, Lanclos K, Holden B P, et al. The automated planet finder at Lick Observatory

- [C/OL]//: volume 9145 Ground-based and Airborne Telescopes V. 2014: 91452B. DOI: [10.11117/12.2057310](https://doi.org/10.11117/12.2057310).
- Ramírez I, Meléndez J. The Effective Temperature Scale of FGK Stars. II.  $T_{eff}$ :Color:[Fe/H] Calibrations[J/OL]. , 2005, 626:465-485. DOI: [10.1086/430102](https://doi.org/10.1086/430102).
- Ribas I, Jordi C, Vilardell F, et al. First Determination of the Distance and Fundamental Properties of an Eclipsing Binary in the Andromeda Galaxy[J/OL]. , 2005, 635(1):L37-L40. DOI: [10.1086/499161](https://doi.org/10.1086/499161).
- Roederer I U, Kratz K L, Frebel A, et al. The End of Nucleosynthesis: Production of Lead and Thorium in the Early Galaxy[J/OL]. , 2009, 698:1963-1980. DOI: [10.1088/0004-637X/698/2/1963](https://doi.org/10.1088/0004-637X/698/2/1963).
- Roederer I U, Lawler J E, Sobeck J S, et al. New Hubble Space Telescope Observations of Heavy Elements in Four Metal-Poor Stars[J/OL]. , 2012, 203:27. DOI: [10.1088/0067-0049/203/2/27](https://doi.org/10.1088/0067-0049/203/2/27).
- Roederer I U, Preston G W, Thompson I B, et al. A Search for Stars of Very Low Metal Abundance. VI. Detailed Abundances of 313 Metal-poor Stars[J/OL]. , 2014, 147:136. DOI: [10.1088/0004-6256/147/6/136](https://doi.org/10.1088/0004-6256/147/6/136).
- Roederer I U, Preston G W, Thompson I B, et al. Neutron-capture Nucleosynthesis in the First Stars [J/OL]. , 2014, 784(2):158. DOI: [10.1088/0004-637X/784/2/158](https://doi.org/10.1088/0004-637X/784/2/158).
- Roriz M, Pereira C B, Drake N A, et al. High-resolution spectroscopic observations of the new CEMP-s star CD -50deg 776[J/OL]., 2017, 472 : 350 – 360. DOI : [10.1093/mnras/stx1930](https://doi.org/10.1093/mnras/stx1930).
- Roth J. What is the best guess for the number of stars in the Milky Way?[J]. , 2006, 111(5):98.
- Ryabchikova T, Piskunov N, Pakhomov Y, et al. Accuracy of atmospheric parameters of FGK dwarfs determined by spectrum fitting[J/OL]. , 2016, 456:1221-1234. DOI: [10.1093/mnras/stv2725](https://doi.org/10.1093/mnras/stv2725).
- Ryan S G. Lithium Trail Leads Back to the Big Bang[J]. The Newsletter of the Isaac Newton Group of Telescopes, 2000, 3:14-16.
- Ryan S G, Aoki W, Norris J E, et al. The Origins of Two Classes of Carbon-enhanced, Metal-poor Stars[J/OL]. , 2005, 635:349-354. DOI: [10.1086/497282](https://doi.org/10.1086/497282).
- Rybicki G B, Hummer D G. An accelerated lambda iteration method for multilevel radiative transfer. I - Non-overlapping lines with background continuum[J]. , 1991, 245:171-181.
- Salvadori S, Schneider R, Ferrara A. Cosmic stellar relics in the Galactic halo[J/OL]. , 2007, 381 (2):647-662. DOI: [10.1111/j.1365-2966.2007.12133.x](https://doi.org/10.1111/j.1365-2966.2007.12133.x).
- Santoro F, Shull J M. Critical Metallicity and Fine-Structure Emission of Primordial Gas Enriched by the First Stars[J/OL]. , 2006, 643:26-37. DOI: [10.1086/501518](https://doi.org/10.1086/501518).
- Sasaki Y, Oguchi H, Kobayashi T, et al. Nitrogen oxide cycle regulates nitric oxide levels and bacterial cell signaling[J/OL]. Scientific Reports, 2016, 6:22038. DOI: [10.1038/srep22038](https://doi.org/10.1038/srep22038).
- Schneider R, Ferrara A, Natarajan P, et al. First Stars, Very Massive Black Holes, and Metals[J/OL]. , 2002, 571(1):30-39. DOI: [10.1086/339917](https://doi.org/10.1086/339917).

- Senchyna P, Stark D P, Chevallard J, et al. Extremely metal-poor galaxies with HST/COS: laboratories for models of low-metallicity massive stars and high-redshift galaxies[J]. arXiv e-prints, 2019: arXiv:1904.01615.
- Shapley H. Investigations of Cepheid Variables. II. The Period-Luminosity Relation for Galactic Cepheids.[J]. Harvard College Observatory Circular, 1927, 314:1-6.
- Siess L. Evolution of massive AGB stars. I. Carbon burning phase[J/OL]. , 2006, 448(2):717-729. DOI: [10.1051/0004-6361:20053043](https://doi.org/10.1051/0004-6361:20053043).
- Silk J. Book-Review - the Big Bang - the Creation and Evolution of the Universe[J]. Science, 1980, 210:59.
- Silk J. On the Nature of the First Stars[C]//Audouze J, Tran Thanh Van J. NATO Advanced Science Institutes (ASI) Series C: volume 117. 1984: 253.
- Skrutskie M F, Cutri R M, Stiening R, et al. The Two Micron All Sky Survey (2MASS)[J/OL]. , 2006, 131:1163-1183. DOI: [10.1086/498708](https://doi.org/10.1086/498708).
- Sneden C, Cowan J J, Lawler J E, et al. The Extremely Metal-poor, Neutron Capture-rich Star CS 22892-052: A Comprehensive Abundance Analysis[J/OL]. , 2003, 591:936-953. DOI: [10.1086/375491](https://doi.org/10.1086/375491).
- Sneden C, Cowan J J, Gallino R. Neutron-Capture Elements in the Early Galaxy[J/OL]. , 2008, 46: 241-288. DOI: [10.1146/annurev.astro.46.060407.145207](https://doi.org/10.1146/annurev.astro.46.060407.145207).
- Sneden C, Lawler J E, Cowan J J, et al. New Rare Earth Element Abundance Distributions for the Sun and Five r-Process-Rich Very Metal-Poor Stars[J/OL]. , 2009, 182:80-96. DOI: [10.1088/0067-0049/182/1/80](https://doi.org/10.1088/0067-0049/182/1/80).
- Sneden C A. Carbon and Nitrogen Abundances in Metal-Poor Stars.[D]. THE UNIVERSITY OF TEXAS AT AUSTIN., 1973.
- Sobeck J S, Kraft R P, Sneden C, et al. The Abundances of Neutron-capture Species in the Very Metal-poor Globular Cluster M15: A Uniform Analysis of Red Giant Branch and Red Horizontal Branch Stars[J/OL]. , 2011, 141:175. DOI: [10.1088/0004-6256/141/6/175](https://doi.org/10.1088/0004-6256/141/6/175).
- Spergel D N, Bean R, Doré O, et al. Three-Year Wilkinson Microwave Anisotropy Probe (WMAP) Observations: Implications for Cosmology[J/OL]. , 2007, 170:377-408. DOI: [10.1086/513700](https://doi.org/10.1086/513700).
- Spite M, Cayrel R, Plez B, et al. First stars VI - Abundances of C, N, O, Li, and mixing in extremely metal-poor giants. Galactic evolution of the light elements[J/OL]. , 2005, 430:655-668. DOI: [10.1051/0004-6361:20041274](https://doi.org/10.1051/0004-6361:20041274).
- Starkenburg E, Shetrone M D, McConnachie A W, et al. Binarity in carbon-enhanced metal-poor stars[J/OL]. , 2014, 441:1217-1229. DOI: [10.1093/mnras/stu623](https://doi.org/10.1093/mnras/stu623).
- Starkenburg E, Aguado D S, Bonifacio P, et al. The Pristine survey IV: approaching the Galactic

- metallicity floor with the discovery of an ultra-metal-poor star[J/OL]. , 2018, 481:3838-3852. DOI: [10.1093/mnras/sty2276](https://doi.org/10.1093/mnras/sty2276).
- Suda T, Katsuta Y, Yamada S, et al. Stellar Abundances for the Galactic Archeology (SAGA) Database — Compilation of the Characteristics of Known Extremely Metal-Poor Stars[J/OL]. , 2008, 60:1159-1171. DOI: [10.1093/pasj/60.5.1159](https://doi.org/10.1093/pasj/60.5.1159).
- Sugimoto D. Mixing between Stellar Envelope and Core in Advanced Phases of Evolution. II — Evolution of Stellar Cores of Initial Masses 10 and 3M —[J/OL]. Progress of Theoretical Physics, 1970, 44(3):599-616. DOI: [10.1143/PTP.44.599](https://doi.org/10.1143/PTP.44.599).
- Sugimoto D, Yamamoto Y, Hōshi R, et al. Evolution of Carbon Stars. II —Carbon Burning Phase— [J/OL]. Progress of Theoretical Physics, 1968, 39(6):1432-1447. DOI: [10.1143/PTP.39.1432](https://doi.org/10.1143/PTP.39.1432).
- Tegmark M. Probes of the Early Universe[D]. -, 1994.
- Thielemann F K, Eichler M, Panov I V, et al. Neutron Star Mergers and Nucleosynthesis of Heavy Elements[J/OL]. Annual Review of Nuclear and Particle Science, 2017, 67:253-274. DOI: [10.1146/annurev-nucl-101916-123246](https://doi.org/10.1146/annurev-nucl-101916-123246).
- Tidwell H, Rooney C, Stacey G. Calibrating ZEUS-2 to Study Star Formation in the Early Universe [C]//American Astronomical Society Meeting Abstracts: volume 233 American Astronomical Society Meeting Abstracts #233. 2019: 146.20.
- Tissera P B, Scannapieco C, Beers T C, et al. Stellar haloes of simulated Milky-Way-like galaxies: chemical and kinematic properties[J/OL]. , 2013, 432:3391-3400. DOI: [10.1093/mnras/stt691](https://doi.org/10.1093/mnras/stt691).
- Tissera P B, Beers T C, Carollo D, et al. Stellar haloes in Milky Way mass galaxies: from the inner to the outer haloes[J/OL]. , 2014, 439:3128-3138. DOI: [10.1093/mnras/stu181](https://doi.org/10.1093/mnras/stu181).
- Tissera P B, Machado R E G, Carollo D, et al. The central spheroids of Milky Way mass-sized galaxies[J/OL]. , 2018, 473:1656-1666. DOI: [10.1093/mnras/stx2431](https://doi.org/10.1093/mnras/stx2431).
- Tody D. The IRAF Data Reduction and Analysis System[C/OL]//Crawford D L. : volume 627 Instrumentation in astronomy VI. 1986: 733. DOI: [10.1117/12.968154](https://doi.org/10.1117/12.968154).
- Tody D. IRAF in the Nineties[C]//Hanisch R J, Brissenden R J V, Barnes J. Astronomical Society of the Pacific Conference Series: volume 52 Astronomical Data Analysis Software and Systems II. 1993: 173.
- Tominaga N, Umeda H, Nomoto K. Supernova Nucleosynthesis in Population III 13-50 M<sub>solar</sub> Stars and Abundance Patterns of Extremely Metal-poor Stars[J/OL]. , 2007, 660:516-540. DOI: [10.1086/513063](https://doi.org/10.1086/513063).
- Tominaga N, Iwamoto N, Nomoto K. Abundance Profiling of Extremely Metal-poor Stars and Supernova Properties in the Early Universe[J/OL]. , 2014, 785:98. DOI: [10.1088/0004-637X/785/2/98](https://doi.org/10.1088/0004-637X/785/2/98).
- Tur C, Heger A, Austin S M. Production of <sup>26</sup>Al, <sup>44</sup>Ti, and <sup>60</sup>Fe in Core-collapse Supernovae:

- Sensitivity to the Rates of the Triple Alpha and  $^{12}\text{C}(\alpha, \gamma)^{16}\text{O}$  Reactions[J/OL]. , 2010, 718(1): 357-367. DOI: [10.1088/0004-637X/718/1/357](https://doi.org/10.1088/0004-637X/718/1/357).
- Turner M S, Schramm D N. The origin of baryons in the Universe[J/OL]. , 1979, 279(5711): 303-305. DOI: [10.1038/279303a0](https://doi.org/10.1038/279303a0).
- Umeda H, Nomoto K. First-generation black-hole-forming supernovae and the metal abundance pattern of a very iron-poor star[J/OL]. , 2003, 422(6934):871-873. DOI: [10.1038/nature01571](https://doi.org/10.1038/nature01571).
- Voronchev V T. Suprathermal nuclear effects in the solar core: overall view[J/OL]. Journal of Physics G Nuclear Physics, 2019, 46(6):065201. DOI: [10.1088/1361-6471/ab1435](https://doi.org/10.1088/1361-6471/ab1435).
- Welsh L, Cooke R, Fumagalli M. Modelling the chemical enrichment of Population III supernovae: the origin of the metals in near-pristine gas clouds[J/OL]. , 2019, 487(3):3363-3376. DOI: [10.1093/mnras/stz1526](https://doi.org/10.1093/mnras/stz1526).
- Wheeler J C, Sneden C, Truran J, James W. Abundance ratios as a function of metallicity.[J/OL]. , 1989, 27:279-349. DOI: [10.1146/annrev.aa.27.090189.001431](https://doi.org/10.1146/annrev.aa.27.090189.001431).
- Wiescher M. The History and Impact of the CNO Cycles in Nuclear Astrophysics[J/OL]. Physics in Perspective, 2018, 20(1):124-158. DOI: [10.1007/s00016-018-0216-0](https://doi.org/10.1007/s00016-018-0216-0).
- Woosley S E. The Evolution of Massive Helium Stars, Including Mass Loss[J/OL]. , 2019, 878(1): 49. DOI: [10.3847/1538-4357/ab1b41](https://doi.org/10.3847/1538-4357/ab1b41).
- Xu Y, Hou L G, Wu Y W. The spiral structure of the Milky Way[J/OL]. Research in Astronomy and Astrophysics, 2018, 18(12):146. DOI: [10.1088/1674-4527/18/12/146](https://doi.org/10.1088/1674-4527/18/12/146).
- Yang Y, Feng X S, Jiang C W, et al. A study of the emergence of flux rope from the solar convection zone into the atmosphere by using a novel numerical method[J/OL]. Physics of Plasmas, 2018, 25(9):090702. DOI: [10.1063/1.5044646](https://doi.org/10.1063/1.5044646).
- Yew M. A Multi-Frequency Study of the Milky Way-like Spiral Galaxy NGC6744[D]. Western Sydney University (Australia), 2017.
- Yong D, Norris J E, Bessell M S, et al. The Most Metal-poor Stars. II. Chemical Abundances of 190 Metal-poor Stars Including 10 New Stars with  $[\text{Fe}/\text{H}] = -3.5$ [J/OL]. , 2013, 762:26. DOI: [10.1088/0004-637X/762/1/26](https://doi.org/10.1088/0004-637X/762/1/26).
- Yoon J, Beers T C, Placco V M, et al. Observational Constraints on First-star Nucleosynthesis. I. Evidence for Multiple Progenitors of CEMP-No Stars[J/OL]. , 2016, 833:20. DOI: [10.3847/0004-637X/833/1/20](https://doi.org/10.3847/0004-637X/833/1/20).
- Yoshida N, Omukai K, Hernquist L, et al. Formation of Primordial Stars in a  $\Lambda$ CDM Universe [J/OL]. , 2006, 652:6-25. DOI: [10.1086/507978](https://doi.org/10.1086/507978).
- Zacharias N, Finch C T, Girard T M, et al. The Fourth US Naval Observatory CCD Astrograph Catalog (UCAC4)[J/OL]. , 2013, 145:44. DOI: [10.1088/0004-6256/145/2/44](https://doi.org/10.1088/0004-6256/145/2/44).

- Zhao G, Magain P. The chemical composition of the extreme halo stars. III. Equivalent widths of 20. [J]. , 1990, 86:85.
- Zhao G, Magain P. Abundances of neutron capture elements in metal-poor dwarfs. I Yttrium and zirconium.[J]. , 1991, 244:425.
- Zhao G, Chen Y Q, Shi J R, et al. Stellar Abundance and Galactic Chemical Evolution through LAMOST Spectroscopic Survey[J/OL]. , 2006, 6:265-280. DOI: [10.1088/1009-9271/6/3/01](https://doi.org/10.1088/1009-9271/6/3/01).
- Zhao G, Zhao Y H, Chu Y Q, et al. LAMOST spectral survey An overview[J/OL]. Research in Astronomy and Astrophysics, 2012, 12:723-734. DOI: [10.1088/1674-4527/12/7/002](https://doi.org/10.1088/1674-4527/12/7/002).
- Zolotov A, Willman B, Brooks A M, et al. The Dual Origin of Stellar Halos[J/OL]. , 2009, 702: 1058-1067. DOI: [10.1088/0004-637X/702/2/1058](https://doi.org/10.1088/0004-637X/702/2/1058).